DOCTORAL DISSERTATION

# Computer simulation of growth and photo-induced phenomena

## József Hegedüs

from Budapest, Hungary

Thesis advisors:

Prof. Sándor Kugler
*Department of Theoretical Physics,*
*Budapest University of Technology and Economics*

and

Prof. Peter Thomas
Fachbereich Physik und
Wissenschaftl. Zentrum für Materialwissenschaften
der Philipps-Universität Marburg

2006

Vom Fachbereich Physik der Philipps-Universität
als Dissertation angenommen am 31.07.2006
Erstgutachter: Prof. Dr. Stephen R. Elliott (Cambridge, UK)
Zweitgutachter: Prof. Dr. Sergei Baranovski (Marburg, Germany)
Tag der mündlichen Prüfung: 22.08.2006

# Table of Contents

# 1 Introduction

Computers become more and more important in every aspect of our life. Their exponentially growing power draws the attention of scientists to solve otherwise unsolvable problems using computer simulations. Computer experiments are just like real experiments. In real experiments we need samples, equipments, measurements and data analysis. Analogously, computer experiments need models, program codes, simulations and data analysis. Using increasing amount of computer resources we approach more and more the reality during our simulations. They explain scientific phenomena and reduce risk of future experiments. They are important both to science and to industry. Experts are needed to make use of the exploding growth of computational power. Interest in computer simulations is now greater than ever.

The physical properties of solids are fundamentally determined by their atomic structure. Atomic structure on the other hand is influenced by the preparation conditions. Computer simulation of the preparation provides insight into how the atomic structure of the prepared material is influenced during preparation. Simulation of preparation of materials is therefore of high importance because it helps to optimize their physical properties for applications. In Chapter 2 and Chapter 3 I explore ways to investigate the preparation of crystalline and amorphous materials using computer simulations. Based on the results obtained in Chapter 3 it is possible to study the photo-induced volume changes in amorphous Selenium and this work is described in Chapter 4. Each chapter has it's own introduction and in the following I only summarize briefly the structure of the thesis.

In Chapter 2 I describe – to my knowledge – for the first time how two dimensional kinetic Monte Carlo simulations can be used to study instabilities during epitaxial growth when the instabilities are induced by immobile impurities. Impurities are unavoidable in experiments, therefore considering their effects is important to all scientist who are involved in epitaxial growth. I do not consider specific physical systems, rather I keep the model as simple as possible to preserve the generality of the results. I am using a simple two dimensional lattice model with nearest neighbor interactions to model the crystal. It is possible to simulate the deposition of a few of million atoms using kinetic Monte Carlo simulations because I take advantage of the periodicity of the crystal. That is not possible in the case of amorphous materials.

In Chapter 3 I present results about the computer simulation of preparation of amorphous materials. Amorphous materials can be prepared basically in two ways: growth from vapor phase and melt quenching from liquid phase. Molecular dynamics simulation allows the investigation of both methods. I study the preparation of two model materials: amorphous Selenium and amorphous Silicon. The topology of their atomic structure is very different: amorphous Selenium has an average coordination number of two, while in the case of amorphous Silicon it is near to four. The first material is under-constrained while the second is over-constrained. Chapter 3 consists of three parts. In the first part I consider the preparation of amorphous Selenium. Classical empirical potentials enable the simulation of large systems, for the comparison of different preparation conditions and methods I take advantage of their effectiveness. The quality of the potential determines drastically the quality of the results, therefore I compare three different potentials for the description of amorphous Selenium in the second part and two potentials for the description of amorphous Silicon in the third part of Chapter 3.

In Chapter 4 I describe how computer simulation can be used to understand photo-induced phenomena in amorphous chalcogenides. I investigate for the first time the photo-induced volume changes in amorphous Selenium thin-films using tight-binding molecular dynamics simulation. The microscopic results predict a new and unified description of photo-induced volume changes, so that both photo-induced contraction and expansion can be explained within the same model.

The thesis ends with a summary of my results.

# 2 Kinetic Monte Carlo simulation of impurity induced growth instabilities

## 2.1 Introduction

Epitaxial growth of crystals is a technologically and scientifically important method to prepare materials for experiments and applications. Without this method many of our everyday used devices (communication, data storage, lasers) could have not been fabricated. Impurities are always present during epitaxial growth, therefore investigation of their effects is important both to science and to industry. Impurities can be deposited intentionally if they are used to dope the crystal. After deposition they can behave basically in two different ways: they can diffuse or they can be immobile depending on their binding energy to the crystal. In my work I will investigate only the case in which impurities cannot diffuse after they have reached the surface of the crystal. First I give a short overview on crystal growth and then I discuss the impurity induced phenomena in a simple one-dimensional model to introduce the physical concepts. Based on this I will then overview the literature and then continue with the discussion of kinetic Monte Carlo simulation and the obtained results. I close the chapter with concluding remarks.

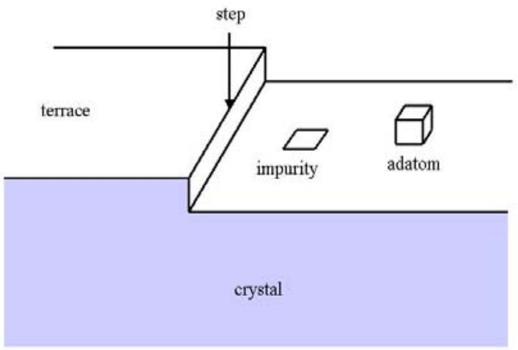

**Figure 2.1. Schematic illustration of a crystal surface with impurities.**

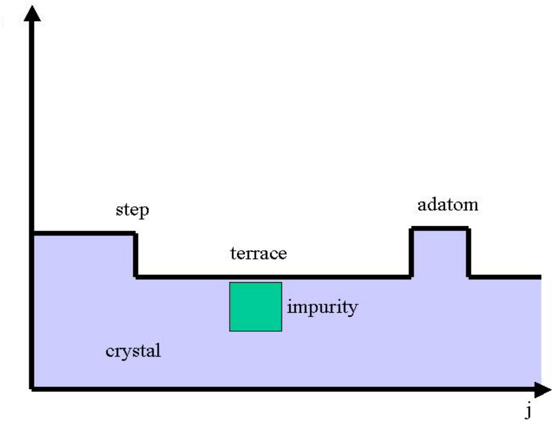

**Figure 2.2. Side view.**

**Impurities inside the terrace affect the diffusion barriers for adatoms on the surface.**

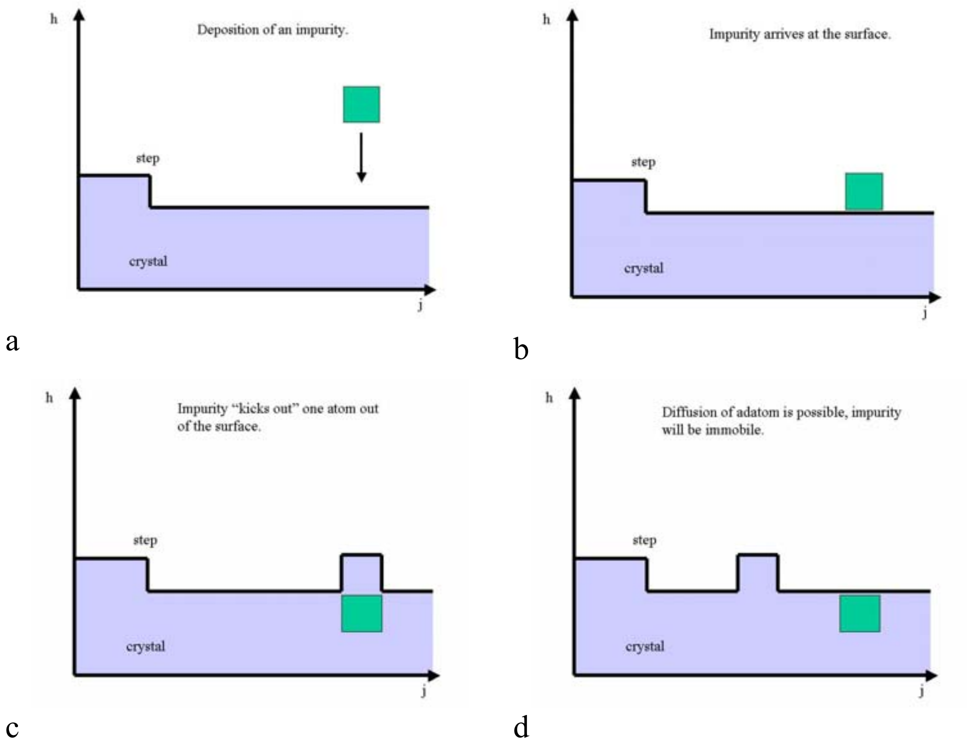

**Figure 2.3 Deposition of an impurity. The event of impurity deposition in my model describes the physical process, where an impurity kicks out an atom out of the surface and will be in the terrace embedded and fixed there (a-b-c). The kicked out adatom can diffuse after this event freely and the impurity stays at the impinging position (d).**

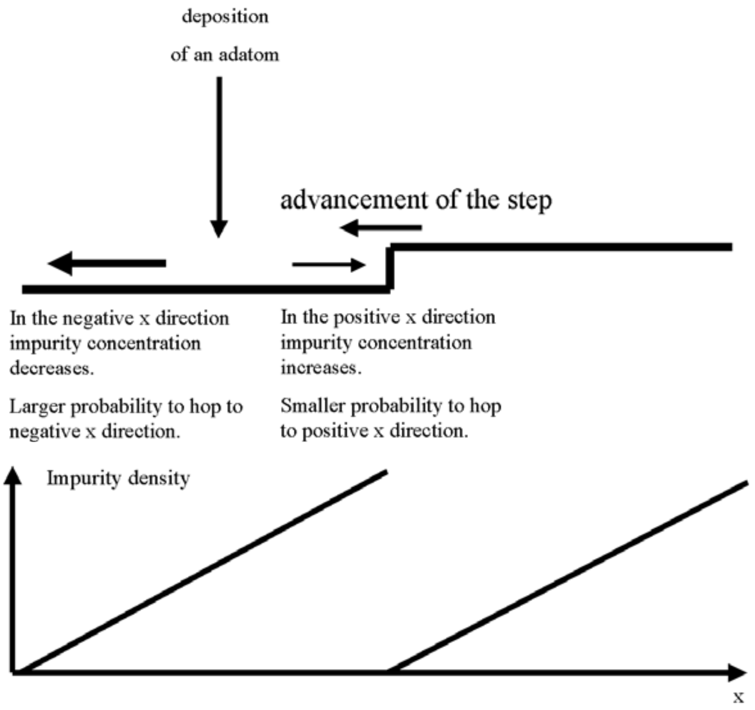

**Figure 2.4. Schematic representation of inhomogeneity of the impurity density in the terrace. This density gradient can lead to drift of adatoms on the terrace. If impurities act as random barriers, an adatom deposited in the middle of the terrace will have a greater probability to diffuse in that direction where less impurities are present. This can lead to step-pairing and step-bunching.**

In Figure 2.1 and in Figure 2.2 I depicted a schematic representation of the crystal surface and the impurities during growth. There are basically two ways for crystal growth to proceed:

1.) Adatoms on the terraces do not nucleate to form islands, they preferentially attach to steps instead of nucleating, this growth mode is called the step-flow growth.
2.) On the contrary, if the tendency of nucleation on the terrace is high, adatoms will form islands on the terraces and new adatoms will feed preferentially the islands and not the steps, therefore, steps do not advance but islands grow and coalesce. Once an island is complete, new islands will form. This growth mode is called nucleation growth.

Which one of the two cases dominates, will depend on the relation of the characteristic diffusion time of an adatom to reach a step after arriving on the terrace, compared to the average time between the deposition of two atoms.

Let us consider an important property of crystal surfaces: surface roughening, also known as the Kosterlitz-Thouless transition. This transition separates two phases: rough (disordered) and flat (ordered). Above the transition temperature, in the disordered phase the height-height correlation function of the surface diverges with distance and step formation is thermodynamically favorable. The step-pairing and step-bunching requires to be in the ordered phase of the Kosterlitz-Thouless transition and at the same time the condition for step-flow growth is essential to be fulfilled.

The process for the depozition of an impurity is schematically shown in Figure 2.3. Impurities will be built in into the terrace immediately. An inhomogeneity of impurity density can arises due to the fact that “newly” deposited parts of the terrace mainly consist of adatoms which are mobile (i.e. not impurities) because such mobile adatoms can reach the steps where they contribute to the growth of the terrace. Parts of the terrace far away from the steps, in opposite direction as steps advance, are rich in impurities due to the fact that these parts of the terrace are “older” and were exposed longer to the deposition flux which contains also impurities. Schematic representation of the impurity density gradient can be seen in Figure 2.4. This gradient can lead to an asymmetry of adatom currents because adatoms deposited to the middle of the terrace can easier diffuse to that direction where fewer impurities are present if the impurities act as random barriers. As later will be shown, this can lead to pairing of steps and eventually bunching of steps because adatoms preferentially feed descending steps. However, if impurities lower the barriers between potential valleys, then adatoms will preferentially feed ascending steps and this can lead to the stabilization of an equidistant step train. These mechanisms were discussed in detail by J. Krug using a one-dimensional analytical description in Ref. 1.

### 2.1.1 Illustration of effects of immobile impurities in a one dimensional model system

Understanding how adatom current asymmetries can lead to step-pairing, step-bunching or equidistant step trains is important because such asymmetries can be induced not only by the presence of impurities but also by electrical field [2], by chemical reactions [3], by potential barriers at the step edges (like Ehrlich - Schwöbel barrier) [4] or by strain.

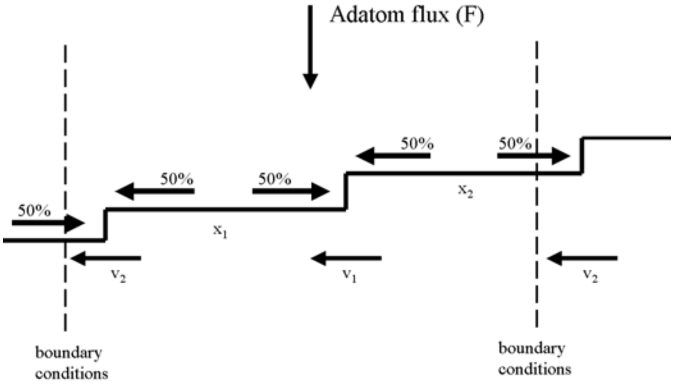

a

Marginal stable case with symmetrical adatom currents. There is no preferential direction for the adatoms on the terraces to hop. Time development of terrace sizes can be described as random walks. Their size distribution is binomial. The average advancement velocity of steps is equal:

$$v_1 = F(0.5x_1 + 0.5x_2)$$
$$v_2 = F(0.5x_1 + 0.5x_2)$$
$$v_2 - v_1 = 0$$

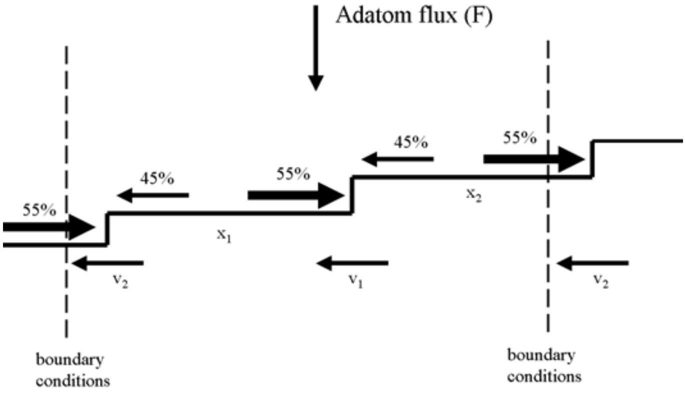

b

Example for a stabilizing case. Adatoms diffuse preferentially to the ascending steps. An effective repulsion between the steps is a consequence of the asymmetrical adatom currents and corresponding average step velocities:

$$v_1 = F(0.55x_1 + 0.45x_2)$$
$$v_2 = F(0.45x_1 + 0.55x_2)$$
$$v_2 - v_1 = -0.1F(x_1 - x_2)$$

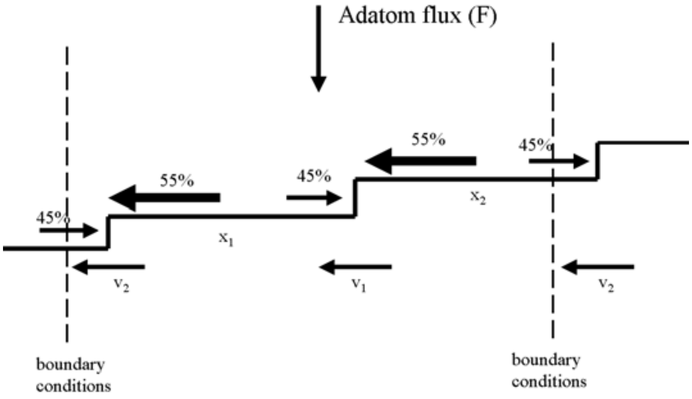

c

Illustration of unstable situation. In this example, 5% more adatoms attach to descending steps than to ascending steps. The system is unstable towards pairing of steps. Which can be understood as an effective attraction between steps due to mass conservation:

$$v_1 = F(0.45x_1 + 0.55x_2)$$
$$v_2 = F(0.55x_1 + 0.45x_2)$$
$$v_2 - v_1 = 0.1F(x_1 - x_2)$$

**Figure 2.5. Illustration of possible adatom current asymmetries and their consequences. There are three different kinds of scenarios corresponding to different asymmetries of adatom diffusion on a terrace (a: no asymmetry, b: preferential diffusion to ascending steps, c: preferential diffusion to descending steps). For simplicity, I consider a system with two terraces, two steps and with periodic boundary conditions. In the figures, $v_1$ and $v_2$ denote the velocities of steps, $x_1$ and $x_2$ the terrace widths. I assume that steps are parallel to each other and their meandering can be neglected. I assumed that steps absorb all adatoms that reach the step.**

An illustration of different scenarios of adatom current asymmetries can be seen in Figure 2.5. Let us consider a system with two terraces and with periodic boundary conditions. In case of no adatom current asymmetries, i.e. no impurities, as depicted in Figure 2.5a, the velocity of advancement of steps is proportional on average to the size of the terraces on which adatoms diffuse to the step,

$$v_1 = F(0.5x_1 + 0.5x_2) \tag{1}$$

$$v_2 = F(0.5x_1 + 0.5x_2) \tag{2}$$

$v_1$ and $v_2$ denote velocities of steps, $x_1$ and $x_2$ the terrace widths, $F$ is the deposition flux. By subtracting these two equations, we find that the difference of the velocities does not depend on the terrace sizes:

$$v_2 - v_1 = 0\,. \tag{3}$$

Therefore, if an initially equidistant step distribution is perturbed so that one terrace becomes larger and the other terrace becomes smaller, the perturbation will remain marginally stable until another perturbation happens to the system. Since deposition of adatoms to terraces is a stochastic process, such random perturbations always occur and the time development of the terrace sizes can be described using a random-walk model. However, if some percentage of the adatoms on the terrace preferentially diffuse to the ascending steps (as shown in Figure 2.5b) then a random perturbation to the equidistant step distribution will be unstable and decay.

Let us consider an example in which 5% of the adatoms preferentially diffuse to the ascending steps, which means that the step velocities will be:

$$v_1 = F(0.55x_1 + 0.45x_2) \tag{4}$$

$$v_2 = F(0.45x_1 + 0.55x_2) \tag{5}$$

and the relative velocity of the steps will depend on the difference of terrace sizes:

$$v_2 - v_1 = -0.1F(x_1 - x_2)\,. \tag{6}$$

If we take $L = x_1 + x_2$ as the total length of the system, then the change of $x_1$ can be described by the differential equation:

$$v_2 - v_1 = \dot{x}_1 = -0.1F(2x_1 - L) \tag{7}$$

where we see that the “restoring force” is proportional to the adatom flux, in other words, the decay of a terrace size fluctuation with a given magnitude always needs the same amount of material to be deposited, independently of the deposition rate. By solving this differential equation we can see that, the typical timescale for decay of a fluctuation equals the time needed to deposit five monolayers:

$$x_1 = L\frac{1}{2}(1 - e^{-0.2Ft}) \tag{8}$$

Using a similar argument in the case when 5% more adatoms attach to descending steps rather than to ascending steps we find that

$$v_2 - v_1 = \dot{x}_1 = 0.1F(2x_1 - L) \tag{9}$$

and we find two solutions depending on the sign of the initial perturbation to ½ L,

$$x_1 = L\frac{1}{2}(1 \pm e^{+0.2Ft})\,. \tag{10}$$

As a consequence we see that impurities which enhance local diffusion stabilize the step distances and impurities which hinder local diffusion lead to step-pairing and eventually can lead to step-bunching.

### 2.1.2 Overview of literature

The literature of epitaxial growth of crystals is enormous but only little interest has been devoted to the computer investigation of impurity induced instabilities during growth. Two of the pioneers, D. Kandel and J. D. Weeks have investigated the impurity problem using a simple Monte Carlo simulation already in 1993 [5], however, their model is much more simple than my model. Recently, J. Krug showed that impurities which hinder local diffusion can lead to step bunching while impurities which enhance local diffusion tend to stabilize an equidistant step distribution during growth [1]. They used a one-dimensional analytical model of crystal growth with immobile impurities. In this chapter I will clarify these mechanisms using a two-dimensional lattice model instead of a one-dimensional continuum theory. Kinetic Monte Carlo approach enables me to follow the microscopic motion of atoms on the surface, therefore in the investigated parameter regime kinetic Monte Carlo modeling is more realistic than continuum theory, where serious approximations are used. The price I have to pay is the limited system size, simulation length and parameter regime I can investigate. Similar simulations already has been discussed in the literature. Encouraging results have been recently achieved by E. T. Croke *et al.*, where the step bunching in SiC systems has been successfully understood using kinetic Monte Carlo simulations [6]. In their model, however, the step bunching has been explained by impurities which were mobile, contrary to the case discussed in this chapter. Furthermore, step-bunching can be induced by electromigration, so that there is a drift of adatoms on the crystal surface in the direction of the descending step. This effect has been numerically verified by M. Sato and M. Uwaha in 1999 [7]. M. Vladimirova *et al.* simulated, using kinetic Monte Carlo method, a model where two species can diffuse on the terraces and react with each other (precursors and crystal units), they have observed pairing of steps, step bunching and mound formation [3]. This is important, because in Ref. 1, only instability of pairs has been considered, which can mean that immobile impurities could cause pairing of steps but not necessarily bunching. A similar question has been addressed in Ref. 3. It is not clear yet, whether the mechanism proposed in Ref. 1 can induce step-bunching and if so, under what conditions. The step-bunching instability should be induced in the case of immobile impurities by the drift of adatoms on the surface, which arises due to diffusion in disordered lattice. An excellent theoretical treatment of this problem has been written by J. W. Haus and K. W. Kehr [8]. Considering pairing of steps, in a recent paper O. Pierre-Louis and J.-J. Metois reports on stable train of pairs of steps on a Si (111) surface during growth around 1230°C under electromigration [2]. Similar step pairs have been investigated by M. Sato and M. Uwaha theoretically in 1996 [9]. Recently, an excellent review on step dynamics and step instabilities also discussing the above mentioned results was published by J. Krug [4], the author and his colleagues have also conducted one-dimensional analytical calculations and simulations to investigate the shape and scaling of moving step bunches and the effect of electromigration [10,11]. This work has been partly motivated by the results of J. Krug and his coauthors.

## 2.2 Simulation Method

### 2.2.1 Kinetic Monte Carlo algorithm

There are different ways to simulate crystal growth. One can follow the motions of atoms in a three dimensional, continuous space, calculating all the forces acting on the atoms and solving the Newtonian equations of motions. This is possible using molecular dynamics simulation, however, the computational demand limits the size of the system to a couple of hundreds atoms, and simulation times to the order of nanoseconds. In the case of crystalline materials, however, we can take advantage of the ordered structure of the crystal, and instead of following the displacement of atoms due to ballistic motion and due to atomic forces, we can simulate the time evolution of the system by limiting our description to certain events as for example hopping, chemical reactions, adsorption or desorption of atoms. Furthermore, instead of characterizing the system by continuous three dimensional variables, which would describe the positions of atoms, we can index the crystal lattice using discrete variables and use discrete variables for the description of the configuration of the system, for example if a given lattice site is occupied by an atom or not. In order to describe time evolution of the system in terms of events, I have to know on average how often certain events happen (hopping of an atom, adsorption).

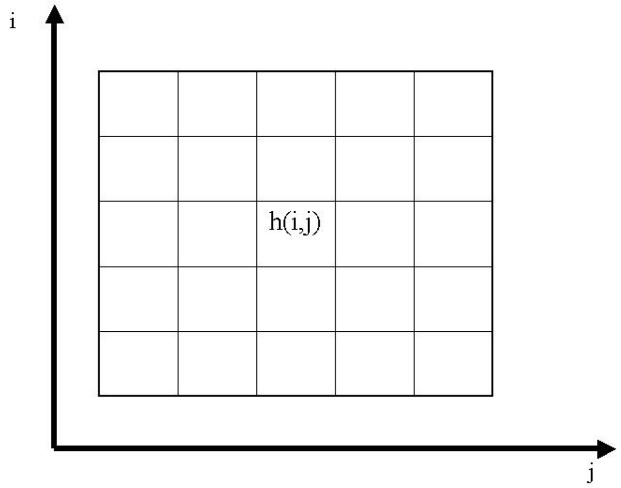

**Figure 2.6 Cubic lattice for the simulation of a 2+1 dimensional solid on solid model. Lattice sites are indexed by i and j. The height of the uppermost atom at is denoted by h(i,j).**

Let $\widetilde{p}$ denote the relative frequency of events. For real physical systems this can be determined either experimentally or theoretically using for example density functional calculations. Let there be $m$ events altogether which describe the time development of the system. For example, if I consider the hopping of single adatoms on a flat surface, and I have algother 100 adatoms on the surface and they can hop to their four neighboring sites, then the total number of events, $m$, is 4*100=400. The total number of events depends on the definition of the model, and the actual configuration of the system.

The probability of an event is given by

$$p = \frac{\widetilde{p}}{R}, \text{ where } R = \sum_{m} \widetilde{p}\,. \tag{11}$$

Knowing these probabilities the time development of the system can be described by the Bortz-Kalos-Lebowitz algorithm [12], which is a stochastic method. I summarize briefly the algorithm:

0. Initialize the system, set values for $imp(i, j, h_{i,j}) = 0$, $h_{i,j}, R$ and $p = \frac{\tilde{p}}{R}$ for all possible events.
1. Choose an event with corresponding probability ( $p = \frac{\tilde{p}}{R}$ ).
2. Carry out the chosen event: change $imp(i, j, h_{i,j}) = 0$ and $h_{i,j}$ accordingly to the chosen event.
3. Recalculate all $\tilde{p}$ that have been changed and recalculate $R$.
4. Return to step 1.

Note that the number of events can in change every cycle.

A 2+1 dimensional cubic solid on solid (SOS) lattice with nearest neighbor interactions modeled the crystal. The size of the system is described by two integer numbers:

$$L_i \text{ and } L_j,$$

They tell the number of lattice sites in both dimensions, perpendicular to the growth direction. Lattice sites are indexed by $i$ and $j$. Every lattice site has a height,

$$h_{i,j},$$

an integer number, which denotes the height of the uppermost atom, below which every site is occupied by an atom, i.e. there are no vacancies in the lattice. The “solid on solid (SOS)” terminology stands for this. A schematic illustration of the lattice can be seen in Figure 2.6. Atoms can have two subtypes: mobile atoms or immobile impurities. I describe the position of impurities using a three dimensional array $imp(i, j, k)$, which stores the type of the atom at lattice site $i$ and $j$, at height $k$. The array, $imp(i, j, k)$, can have two values: $imp(i, j, k) = 0$, if the atom at the position $i, j, k$ is a mobile atom and $imp(i, j, k) = 1$ if it is an impurity. Since there are no atoms above $h_{i,j}$, $imp(i, j, k)$ is only defined for $k \le h_{i,j}$.

### 2.2.2 Relative probabilities of events

For the kinetic Monte Carlo modeling of crystal growth it is needed to match the probabilities of the events with physical relevance. First, let’s consider the hopping of a single adatom on a terrace. Adatoms usually sit in a potential valley at a given lattice point and vibrate. They are trying to escape from the potential valley to a neighboring valley. The probability of escaping is proportional to

$$e^{-\frac{E}{k_B T}},$$

where $E$ is the height of the energy barrier to overcome, $T$ is the temperature, $k_B$ is the Boltzmann constant. If the adatom tries to escape $\nu$ times per second, then

$$D = \nu e^{-\frac{E}{k_B T}}$$

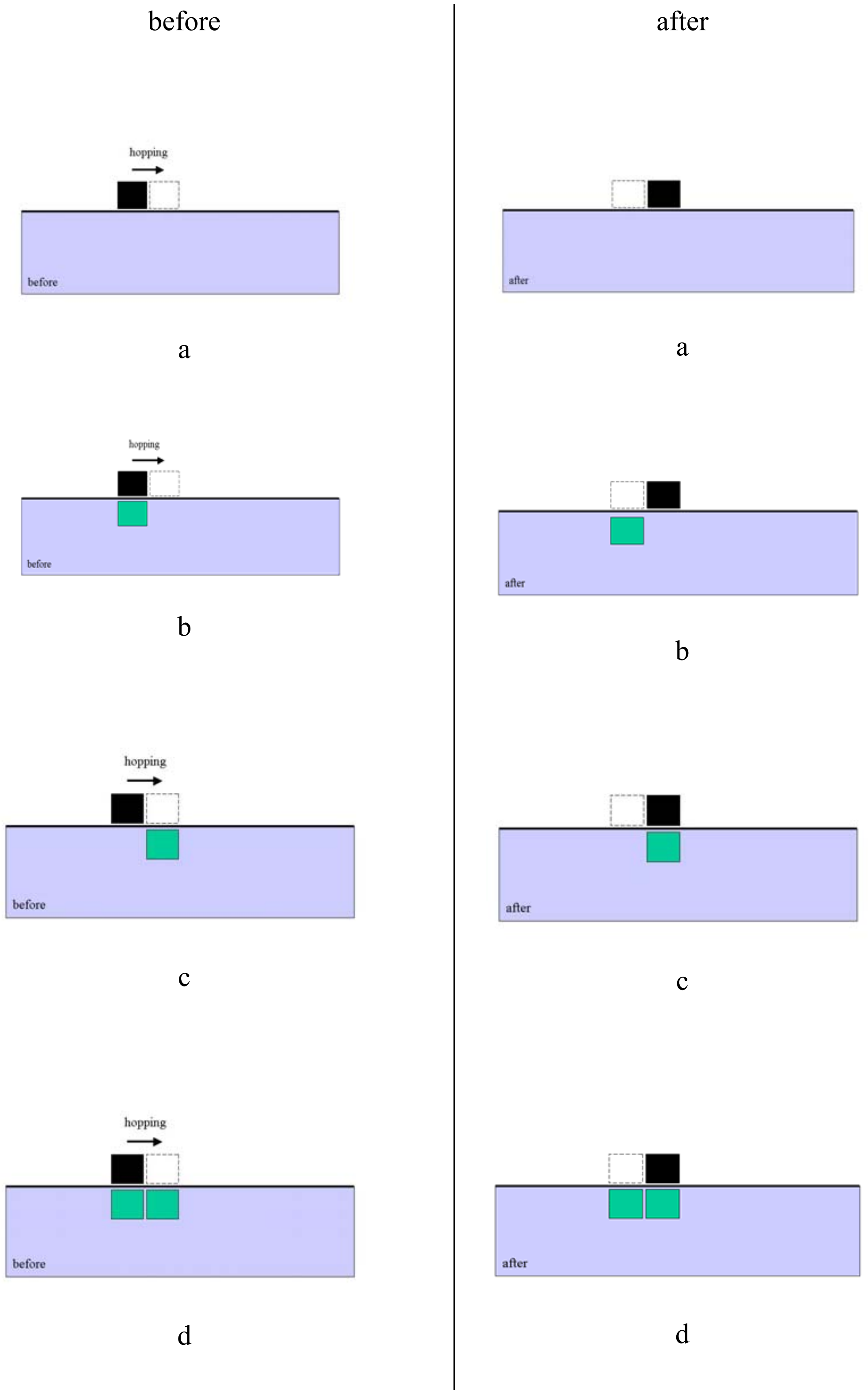

**Figure 2.7. Illustration of single adatom hopping processes, whose hopping probabilities are different due to different local impurity configurations in the terrace.**

gives the number of hops of an adatom per second on the terrace. The potential valleys on the terrace are illustrated in Figure 2.8. Immobile impurities can act as extra random barriers for diffusion since they are randomly distributed due to the randomness of the deposition. Diffusion on such a random surface has been theoretically treated by Haus and Kehr [**8**]. Such a theoretical treatment is necessary for the continuum description. In kinetic Monte Carlo simulations, however, the effect of impurities are taken into account directly by changing the hopping probability of the adatom according to the barrier caused by the impurity. Depending on the impurity configurations, there are four possible scenarios I have to consider to describe hopping of a single adatom (no neighbors) on the terrace, the simplest case is without impurities as shown in Figure 2.7a. Since only the relative frequency is important in the Bortz-Kalos-Lebowitz algorithm, I take

$$\widetilde{p} = 1,$$

for this event. It is important to note that this $\widetilde{p}$ is only valid for hopping of a single adatom on a clean terrace, without any nearest neighbors and it changes depending on the number of nearest neighbors, $n$, which is defined for an adatom at site, $i, j, h_{i,j}$ , as

$$n = f(h_{i,j} - h_{i,j+1}) + f(h_{i,j} - h_{i,j-1}) + f(h_{i,j} - h_{i+1,j}) + f(h_{i,j} - h_{i-1,j}), \qquad (12)$$

where $f(x) = 1$, if $x \le 0$, otherwise it is 0.

If the single adatom (adatom without neighbors ) sits on an impurity and hops to a site, below which there is no impurity, as illustrated in Figure 2.7b, the relative probability of the hopping of the single adatom is given by (definition of $J_{imp}$, simulation parameter)

$$\widetilde{p} = \frac{1}{J_{imp}}. \qquad (13)$$

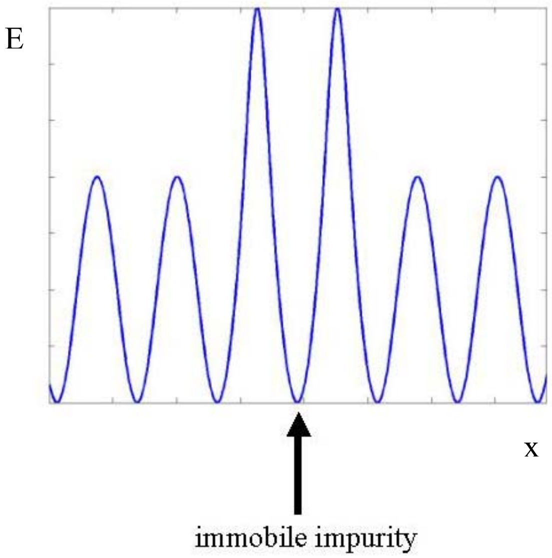

**Figure 2.8 Illustration of potential energy landscape on the terrace. I consider only impurities that change only the potential barriers but not the depth of the potential valley, i.e. they do not change the chemical potential of adatoms. In this example I depicted only the case when an impurity acts as an extra barrier for the hopping of adatoms.**

The frequency of such a hopping will be reduced or increased in comparison to the hopping on the clean surface, depending on the type of impurity, if the impurity lowers the hopping barrier,

$$J_{imp} < 1, \tag{14}$$

which enhances local diffusion of adatoms. If the impurity increases hopping barrier,

$$J_{imp} > 1, \tag{15}$$

and the local diffusion will be slowed down.

Not only if the source site (black square, Figure 2.7, before) but also if the site below the target site (empty square, Figure 2.7, before) is an impurity, will the relative probability change to

$$\tilde{p} = \frac{1}{J_{imp}} \tag{16}$$

as shown in Figure 2.7c. This condition is important because it ensures that impurities in the model act as random barriers rather than random traps, which would be the case if this event would be absent in the calculation.

However, if both the target, and the source sites are contaminated by impurities (see Figure 2.7d) the adatom feels the effect of both impurities, therefore the relative probability of hopping will be:

$$\tilde{p} = \frac{1}{J_{imp}^{2}} \tag{17}$$

for a single adatom.

In the case of hopping of adatoms with neighbors on a clean surface the relative probability reads as (this is the definition of $J$, simulation parameter)

$$\tilde{p} = \left(\frac{1}{J}\right)^{n} \tag{18}$$

where, $n$, is the number of nearest neighbors (see Eq. 7.). Physically, in the most simple case, $J$ depends on the bonding energy between atoms. It follows

$$J = e^{\frac{E_b}{k_B T}}, \tag{19}$$

where $E_b$ corresponds to the (in-plane) bonding energy to neighboring atoms on the terrace. Note that this energy might be different compared to the bonding energy to the terrace and it might even depend on the number of neighbors and other factors.

For the description of the relative hopping probability of a not-single adatom on the surface, I have to take into account both the effects of neighboring atoms, and effects of impurities. I assume, that the energy barriers felt by the adatom are the sum of barrier caused by the impurity and the bonding to other adatoms. Mathematically this assumption can be written as

$$\tilde{p} = \left(\frac{1}{J}\right)^{n} * \left(\frac{1}{J_{imp}}\right)^{\mu}. \tag{20}$$

### 2.2.3 Deposition of crystal atoms and impurities to the surface

There are two kinds of atom which are deposited to the surface: crystal atoms and impurities. Crystal atoms are the atoms which make up most of the crystal and impurities are only a few percent. Crystal atoms can diffuse on the terraces after deposition. Impurities, in the contrary, will be immediately built into the uppermost surface layer after impinging to the surface (as shown in Figure 2.3).

$R_{growth}$ describes, how many times on average a single adatom hops on a clean surface until the next adatom arrives. In Table 2.1 I compares the relative probabilities of events in the kinetic Monte Carlo simulation. I will introduce an important concept relating to growth rate, terrace size, island formation and step-bunching.

| **Description of events** | **Relative probability of event** ($\tilde{p}$) | **Changes due to event.** |
|---|---|---|
| Hopping of a mobile atom (not impurity) from $i, j, h_{i,j}$ (source site) to one of the nearest neighbor sites (target site). | $\tilde{p} = \left(\frac{1}{J}\right)^n * \left(\frac{1}{J_{imp}}\right)^\mu$<br>$0 \le n \le 4$ is the number of neighbors at $i, j, h_{i,j}$.<br>$0 \le \mu \le 2$ is the number of impurities involved in the hopping. [See Figure 2.7] | The height of target site is increased by one and $h_{i,j}$ is decreased by one. |
| Deposition of atoms at $h_{i,j}$. | $\tilde{p} = \frac{1}{R_{growth}}$<br>Physical meaning: between two depositions, an adatom without neighbors hops approximately $R_{growth}$ times on average, because the relative probability of the hopping of an adatom without neigbours on a surface without impurities is 1. | With probability $\rho_{imp}$, $imp(i, j, h_{i,j}) = 1$ is set. (This corresponds to the incorporation of an impurity into the terrace). After this, the height of target site is increased by one and at the increased height $imp(i, j, h_{i,j}) = 0$ is set. (This corresponds to the deposition of an adatom on the terrace) |

**Table 2.1 Summary of relative probabilities of events in the kinetic Monte Carlo algorithm.**

If the number of steps in the system is $N_{steps}$ and $L_j$ is the system length perpendicular to the directions of the steps, then the average step distance is

$$\frac{L_j}{N_{steps}}.$$

This is the characteristic distance an adatom has to reach by diffusion until the next adatom arrives in order to avoid the accumulation of adatoms on the terraces and to avoid nucleation and island-formations. Therefore, for the investigation of step bunching I have to make sure, that the adatoms are deposited slowly enough so that they can reach the steps before they meet the next adatom. Let us assume that I have a set of parameters at which the system is in step-flow growth mode and I would like to increase the size of the system. The above concept implies that I have to pay special attention when I change

$$\frac{L_j}{N_{steps}}.$$

Since the characteristic distance an adatom can reach via diffusion is proportional to the square root of the number of total diffusion steps. Therefore, the corresponding distance, $l$, between deposition of two adatoms is

$$l \propto R_{growth}{}^{1/2}$$

because the number of hops between the deposition of two atoms is on average $R_{growth}$ per adatom. Therefore, for example by doubling the system size, I have to reduce the growth rate by a factor of four in order to achieve the same growth conditions, i.e. for example not to go from step-flow growth to island growth.

### 2.2.4 Boundary conditions

Since I want to study the effect of impurities on step bunching, special care must be paid to boundary conditions. For the four sides of the rectangular cubic lattice, I have four boundary conditions. I do not have to take care about the corners of the lattice, because I do not have diagonal interactions, which would be the case in a more complicated model.

1. $h_{0,j} = h_{L_i,j}$
2. $h_{1,j} = h_{L_i+1,j}$
3. $N_{steps} + h_{i,L_j} = h_{i,0}$
4. $N_{steps} + h_{i,L_j+1} = h_{i,1}$

$N_{steps}$ corresponds to the number of steps in the system. These boundary conditions force the presence of $N_{steps}$ steps parallel to the direction i. More complicated boundary conditions are also possible to investigate using my program code, for example diagonal steps, however, to investigate the effect of impurities on step bunching and to compare the results with one-dimensional continuum theories these boundary conditions are the most appropriate.

| Parameters | Description |
|---|---|
| $\rho_{imp}$ | Relative number of impurities, for example in the case of 10% impurities, $\rho_{imp} = 0.1$. |
| $R_{growth}$ | Growth rate. Between the deposition of two atoms, an atom without neighbors on the flat surface hops $R_{growth}$ times on average. |
| $J = e^{\frac{E_b}{k_B T}}$ | $J$ depends on the bonding energy between atoms. $E_b$ corresponds to the bonding energy to a neighboring atom on the terrace. |
| $J_{imp} = e^{\frac{E_{imp}}{k_B T}}$ | This term describes how an impurity below an adatom affects the hopping probability of the adatom. $E_{imp}$ is the extra energy barrier for hopping due to an impurity [See Figure 2.8]. |
| $L_i$ | Cell size in direction i. |
| $L_j$ | Cell size in direction j. |
| $N_{steps}$ | Number of steps in the system (periodic boundary condition in the i direction is shifted by $N_{steps}$ at the ends of the cell). |

**Table 2.2. Summary of the parameters in the kinetic Monte Carlo algorithm to simulate crystal growth in the presence of immobile impurities.**

### 2.2.5 Implementation

The Bortz-Kalos-Lebowitz algorithm described in the previous section at the first glance seems to be very easy to implement in any programming language. However, there are two critical steps in the algorithm, where special care must be taken if there are large numbers of events: the first is to choose the events with the appropriate probability:

$$p = \frac{\tilde{p}}{R} \tag{21}$$

and the second is to recalculate:

$$R = \sum_m \tilde{p} \tag{22}$$

after carrying out the event, because some $\tilde{p}$-s change due to new atomic arrangements. The first step could be naively carried out as it is illustrated in Figure 2.9. for a total number of eight events. Let $0 \le r \le 1$ be an uniformly distributed random variable. Then by finding an integer, $k$, for which

$$\sum_{m<k} p_m < r < \sum_{m<k+1} p_m$$

holds, we have chosen the $k+1$-th event with probability $p_{k+1}$. With this algorithm we can always choose an event with the appropriate probability in every kinetic Monte Carlo step. However, in order to simulate the growth of realistic systems, for example in a system with 500x500 lattice size the deposition of ten monolayers (2,5 million atoms) would mean about one million possible events per kinetic Monte Carlo Step and at least 2,5 billion kinetic Monte Carlo steps with a typical deposition rate of

$$R_{growth} = 1000.$$

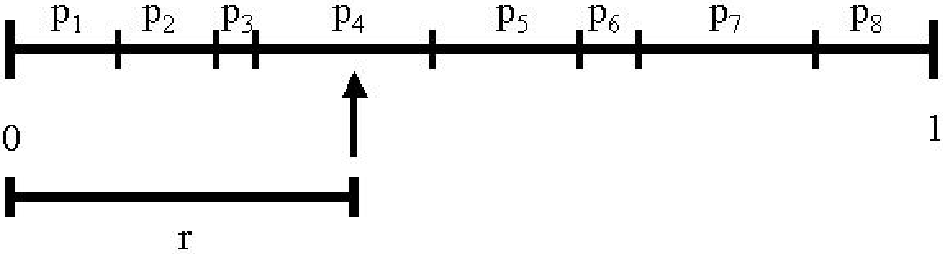

**Figure 2.9. Illustration of a simple algorithmic to choose an event with appropriate probability in the case of eight total events. By generating a randnom number $0 \le r \le 1$, with a uniform probability distribution it is possible to find chose an event with appropriate probability distribution, as represented in the figure. The time needed to chose an event is proportional to the total number of events.**

Therefore, the aforementioned way to choose an event would require five or six orders of magnitude more CPU time (it would take about 100 years) rather than using the currently implemented tree-search algorithm (it takes only couple of days). This algorithm exploits the fact that if interactions are not long-ranged, in one kinetic Monte Carlo step only a few, typically a couple of ten, events change. Therefore only a couple of $\tilde{p}$-s must be recalculated and therefore the search for events with appropriate probability can be carried out efficiently by using a recursive algorithm described below.

The tree-search algorithm finds an event as illustrated in Figure 2.10 in three steps:

1. $0 < r < p_1 + p_2 + p_3 + p_4$ (23)
2. $p_1 + p_2 < r < p_1 + p_2 + p_3 + p_4$ (24)
3. $p_1 + p_2 + p_3 < r < p_1 + p_2 + p_3 + p_4$. (25)

The CPU time required for the tree-search algorithm scales logarithmically with the number of events if the number of event-changes in one kinetic Monte Carlo step is independent of the system size, i.e. the interactions describing the physical system are short ranged (for example Ising-model).

The algorithm has been implemented using object oriented programming in Java. The structure of the language is very well suited to the nature of the problem. The tree-search algorithm implemented in Java has two advantages, flexibility and efficiency. The code is flexible due to the object oriented implementation, where the events are treated as isolated entities and large parts of the code is isolated from each other, this means that if I have to change the code at some part the other parts will continue to function properly. Furthermore, the tree-search is extremely efficient when it comes to large systems as shown above. In the future nearly any kind of kinetic Monte Carlo simulations of systems with short range interactions can be efficiently carried out using this code that I have developed during my PhD work.

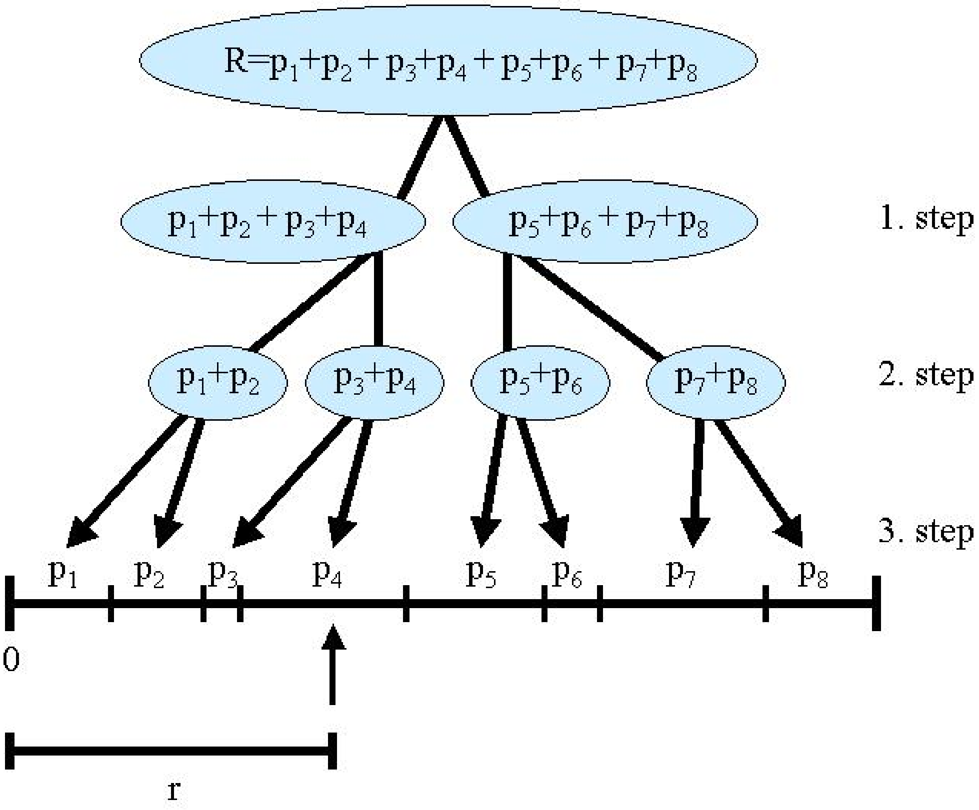

**Figure 2.10. Tree-search algorithm to find $p_4$, if we know the partial sums of probabilities. Note, that instead of 8 comparisons as in the linear case (Figure 2.9), here we are able to find $p_4$ using only 3 comparisons. In case of one million events we would need only 20 comparisons instead of one million. The tree must be stored in memory during simulation. Furthermore, updating of the tree takes only a few steps: if an event changes, only the nodes on the path from the top node (root) to the particular event must be updated.**

### 2.2.6 Data analysis and storage

Since the simulation of deposition of the order of tens of thousands of particles takes billions of kinetic Monte Carlo steps, special care must be paid when storing and analyzing such a mass of numerical data. There are basically two different ways to analyze simulation data and calculate relevant physical quantities:

1. during the simulation
2. after the simulation.

Both approaches have their advantages and disadvantages, especially when dealing with such a great number of simulation steps the difference between the two methodologies is striking. Analyzing data during the simulation has the advantage that disk access is minimal, therefore in the case of large amount of data transfer this approach can save huge amount of time. On the other hand, analyzing data after the simulation has the advantage that any kind of analysis can be done quickly without having to resimulate the whole process. The drawback of this method is that the time resolution is courser, as for example in the case of a system with the following parameters:

$$L_x = 25; L_y = 100; R_{growth} = 400; J = 40; \rho_{imp} = 0$$

the deposition of 500 atoms required on average 1.8 million kinetic Monte Carlo Steps. This high number can be understood approximately by assuming that there are five single adatoms on the terrace and for every new atom to arrive every adatom on the terrace must hop on average 400 times, since

$$R_{growth} = 400.$$

Therefore, for every new adatom to be deposited on average 5*400=2000 kinetic Monte Carlo steps should be carried out if we restrict ourselves to the hopping of single adatoms on terraces. Therefore, to deposit 500 atoms, at least 2 million kinetic Monte Carlo steps are needed on average if there are five atoms on the terrace.

Because writing to disk costs a lot of time, only after every 500th deposited atom has the configuration been written to disk. Analysis of data has been carried out using Matlab and Perl. Simulations have been run using parallel computers in Jülich (JUMP). The kinetic Monte Carlo algorithm is inherently serial; however, using parallel computer simulation of different realizations of the same system and over large parameter regimes is possible. This means practically, that a typical job consists of a few hundred different simulations with different parameters. The only drawback of parallel computers in Jülich (JUMP) is the limited job duration which is at most 24 hours. Therefore, after finding the most relevant parameter regime, longer than 24 hour simulations must be carried out using single desktop PCs.

## *2.3 Discussion of results*

### 2.3.1 Investigation of the parameter regime

The kinetic Monte Carlo model I investigate reproduces both the roughening transition and the different types of growth modes (nucleation vs. step-flow). In general a numerical model with seven parameters can show very complicated behaviors. Since my goal is to investigate step-pairing and step-bunching induced by impurities I have to find a convenient parameter regime first. For this purpose the supercomputer JUMP in Jülich is an excellent tool. Several hundreds of simulations have been carried out until step-bunching and step distance stabilizing effects have been observed. To illustrate the complicated behavior of the system I summarized results of 20 simulations in Table 2.3. Depending on the parameters I have observed basically four different scenarios during growth, labeled with four terms: “islands”, “step-flow”, “step-pairs”, “islands and step-pairs”. A typical island and it’s growth is depicted in Figure 2.11. Note that with increasing adatom flux islands always appear and we observe a transition from step-flow growth mode to nucleating growth. Also note that such a transition can be induced not only by increasing the adatom flux but also by introducing impurities. Impurities trap adatoms, and those adatoms can act as nucleation centers to which new adatoms can attach and so formation of islands begins.

| $J_{imp}$ | $R_{growth}$ | | | |
|---|---|---|---|---|
| | 100 | 200 | 400 | 800 |
| 0.5 | islands | step-flow | step-flow | step-flow |
| 1 | islands | step-flow | step-flow | step-flow |
| 2 | islands | step-pairs | step-pairs | step-pairs |
| 3 | islands | islands | islands and step-pairs | step-pairs |
| 4 | islands | islands | islands and step-pairs | step-pairs |

**Table 2.3. Search for convenient parameters to investigate step-pairing. Meaning of labels: "islands" stands for nucleating growth mode, "step-flow" means that adatoms mostly attached to step edges, "step-pairs" labels a situation where the two steps formed a pair, "islands and step-pairs" means that step pairing and island formation cyclically followed each other. Other system parameters were:**

$$\rho_{imp} = 0.1; L_x = 100; L_y = 25; J = 40; N_{steps} = 2$$

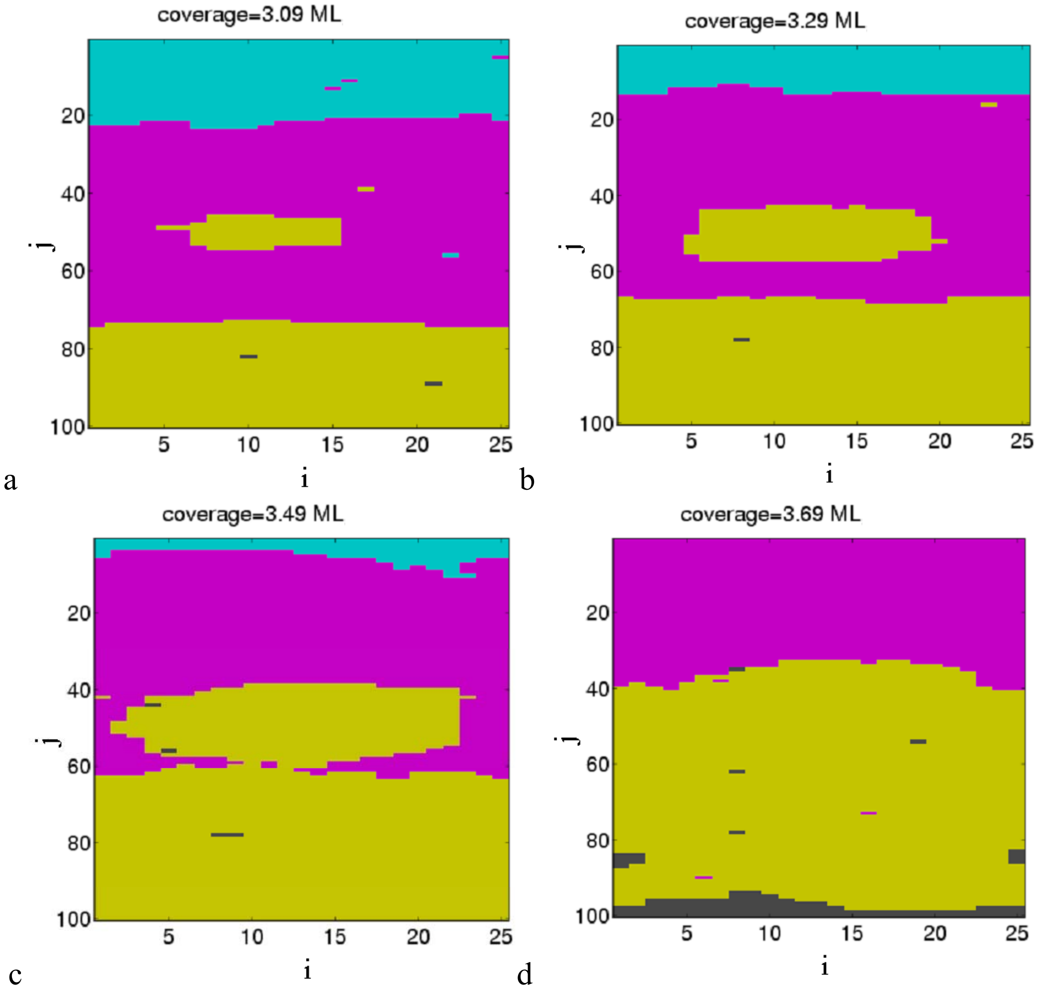

**Figure 2.11. Formation and growth of islands during growth. To be able to investigate step-bunching such phenomena is to be avoided. Different pictures belong to different number of atoms deposited to the surface (a: 3.09 MLs, b: 3.29 MLs, c: 3.49 MLs, d: 3.69 MLs). Different colors indicate different surface heights: cyan is 0, purple is 1, yellow is 2, gray is 3. Note that adatoms feed the island and steps at the same time, steps advance as the island grows. System parameters:**

$$L_i = 25; L_j = 100; \rho_{imp} = 0.1; J = 40; N_{steps} = 2; R_{growth} = 100; J_{imp} = 0.5$$

Such a transition can be observed at

$$R_{growth} = 200,$$

if we increase the height of the potential barrier caused by the impurities, we see how islands start to form due to the newly introduced nucleation centers, adatoms trapped by impurities.

Another interesting phenomena is that step-pairing and islands can be seen at the same time. After the steps formed a pair and the terrace got bigger, the probability for two adatoms on the terrace to find each other becomes high enough to spark island formation. This only happens beyond a critical terrace size and this terrace size can be reached when steps form pairs. Therefore, we can observe a cyclical behavior where steps first form pairs and then island formation occurs on the already large terraces and so terraces will be equalized again and there will be no longer step pairs on the terraces so the whole process repeats itself. Such a process is labeled by "islands and step-pairs" and will be discussed later in more detail once the concept of space-time plots is introduced.

My main task is to investigate step-pairing and step-bunching, therefore the formation of islands is not desirable this means that I must investigate the parameter regime where

$$R_{growth} \geq 800.$$

Note that if the flux is decreased I have to carry out more kinetic Monte Carlo steps per deposited adatom, therefore more computer time will be needed. I have to try to keep the adatom flux as high as possible and at the same time avoid the formation of islands.

### 2.3.2 Step-pairing and space-time plots

In Figure 2.12 I have depicted a typical process of step-pairing. Since the inhomogenities of impurity distribution leads to step-pairing as explained previously, I also depicted the locations of impurities. The initial configuration of the system can be seen in Figure 2.12, top panel. Initially there are no impurities and the two terraces have the same size, i.e. the two step distances are equal. In the middle panel, the situation after depositing 0.2 monolayer, i.e. 500 atoms can be seen. Note that the approx. 50 impurities are distributed uniformly. The two step distances are nearly the same. In the lower panel the configuration after the deposition of 5000 atoms is shown. The steps formed pairs due to the inhomogeneous impurity distribution. Which can be seen in the left figure at the bottom. There are only a few impurities on the top of the higher terrace (yellow) , while before the steps (before light blue) there are many impurities. The reason for this is that the "young" part of the terrace is composed of adatoms which were collected by the step from the terrace, while "old" parts of the terrace have been exposed for a long time to the adatom flux, therefore also to impurity incorporation. Since my main interest was to investigate the time-development and stability of step-pairing and step-bunching I had to find a way to efficiently present simulation data. In Figure 2.12 it can be seen that the system can be viewed as a quasi one-dimensional system because the fluctuations of the step edges are small.

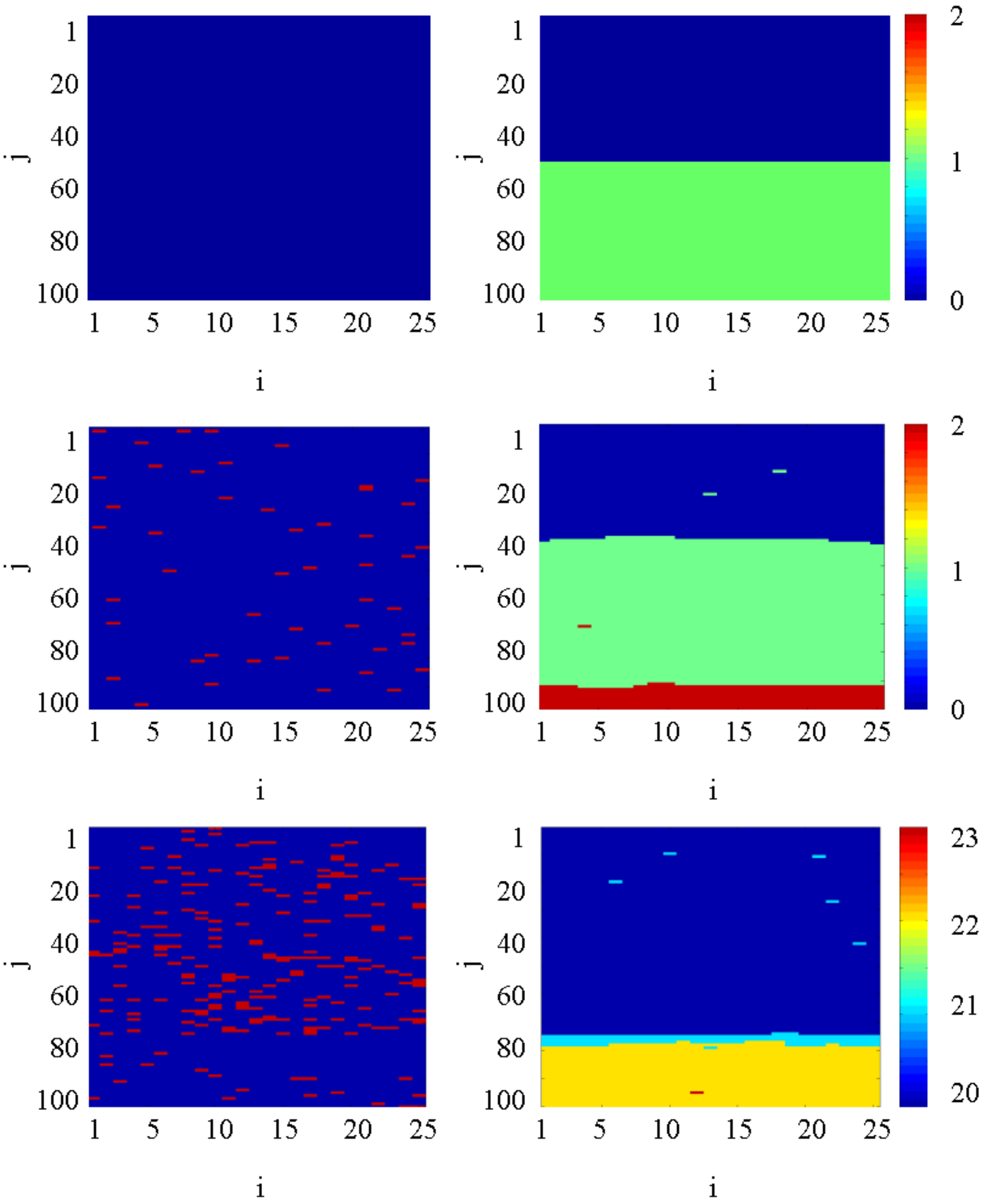

**Figure 2.12. Impurity distributions (left) and color coded surface height profiles (right) at three different growth stages for a system which shows step-pairing. If the highest atom in the right figures at a given i and j is an impurity then the pixel at i and j in the left figure is colored with red, otherwise it's blue. Practically, left figure shows the places where impurities sit in the terraces. Upper panel shows the initial configuration with an initial coverage of 1250 atoms, equal step distances. Middle panel shows the situation after the deposition of 500 atoms, note that the impurities are uniformly distributed and the step distances doesn't deviate too much from the initial configuration. Lower panel corresponds to a surface morphology after deposition of 50000 atoms, namely 20 monolayers, step-pairing can be observed. Note that impurities at the terrace are not uniformly distributed any more, there are more impurities ahead the steps than behind the steps. Simulation parameters are the following:**

$$L_i = 25; L_j = 100; J = 40; J_{imp} = 4; \rho_{imp} = 0.1; R_{growth} = 800; N_{steps} = 2$$

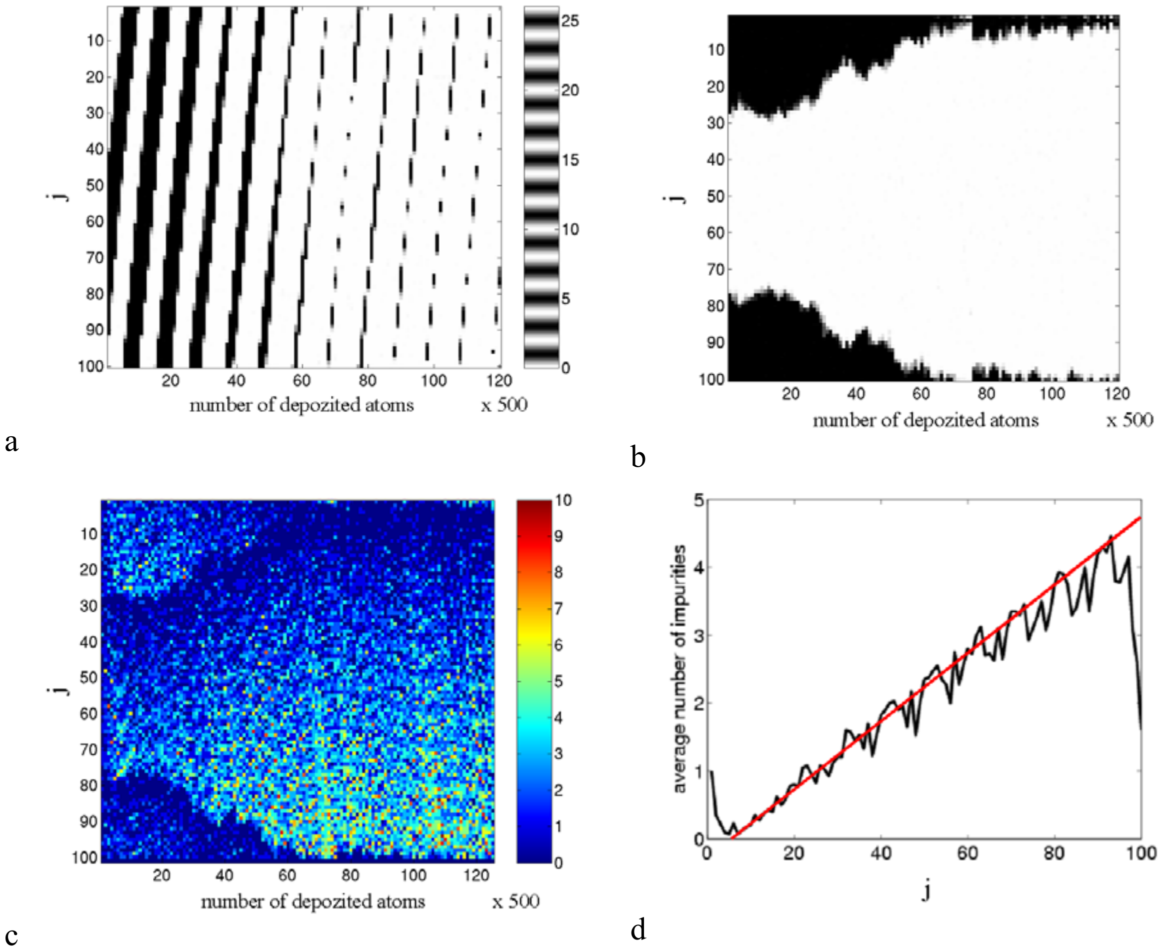

**Figure 2.13. Space time plots and distribution of impurities for a system which shows step pairing. a: space-time plot, b: space-time plot in a coordinate system moving with the average step advancement velocity, c: time-development of impurity distribution in moving coordinate frame (color coding denotes the average number of impurities); d: averaged impurity distribution after step pairing (averaged between 80x500 and 120x500 atoms deposited corresponding to Figure c). The red line in Subfigure d represents the theoretical curve corresponding to Figure 2.4. The deviation is a sign of impurity density saturation. System parameters are the same as in Figure 2.12.**

$$L_i = 25; L_j = 100; J = 40; J_{imp} = 4; \rho_{imp} = 0.1; R_{growth} = 800; N_{steps} = 2$$

I can average over the i coordinate and describe the system in every step by an average height function of j. By color-coding these average heights and putting the columns next to each other I am able to visualize the time development of the system, as can be seen in Figure 2.13a. Cyclical grayscale codes the different heights. Every even height is coded by white and every odd height is coded by black as shown in the bar in Figure 2.13a.

Let us consider first the initial configuration in Figure 2.13a. There are no deposited atoms, this corresponds to the first column in Figure 2.13a (number of deposited atoms equals zero). Where the terrace with height 0 corresponds to a very narrow white strip in the range $1 \le j \le 50$, this corresponds to the blue terrace in the top right subfigure in Figure 2.12. Similarly, the green terrace with height 1 in the top right subfigure in Figure 2.12 corresponds to the narrow black strip in the range of $50 \le j \le 100$ in Figure 2.13a. Note that as atoms are deposited the narrow stripes shift to smaller x numbers, this corresponds to growth and to the advancement of steps.

My aim is to investigate the time development of terrace sizes during growth. Principally, all information is contained in Figure 2.13a, however, this Figure is not easily analyzable because the subsequent pixel columns corresponding to subsequent atomic configurations are shifted always due to the 0.2 monolayer coverage difference. I can present the time development of terrace sizes in a better way if I apply a back shift so that the average position of steps corresponds to $j = 50$ and I have two steps at $j = 25$ and at $j = 75$ in the beginning, as shown in Figure 2.13b. Physically, this means that I first look at the system from a coordinate system which moves with the average step advancement velocity and I make the space time plot from that coordinate system. Using this method I see the time development of size fluctuation of terraces. Let us examine the time development of step pairing in Figure 2.13a and Figure 2.13b. In the initial configuration (number of deposited atoms equals to zero) we can see in both pictures that the sizes of the two terraces are equal. After depositing 100x500=50000 atoms, i.e. 20 monolayers, we can see in both pictures that the white terrace (even height) became nearly as big as the whole system, while the black terrace (odd height) almost disappeared. Let us compare the average surface height in Figure 2.13a and b with 100x500=50000 atoms deposited and the corresponding bottom right subfigure in Figure 2.12, with also 100x500=50000 deposited. We can follow in all pictures (Figure 2.12, Figure 2.13) how step pairing occurs and see that the step-pair stays stable after pairing with only minor fluctuation.

Step-pairing occurs due to inhomogeneous distribution of impurities as it can be seen in Figure 2.13c and Figure 2.13d. In Figure 2.13c the time development of the number of impurities along the i-direction at a given j position is depicted. The coordinate system in Figure 2.13c corresponds to the same moving coordinate system as in Figure 2.13b. Note that after depositing 2000 atoms, in the initial stage, at $j = 30$ there are no impurities and at the end of the terrace, at $j = 75$ there are two impurities on average. As the terrace gets wider due to step pairing, i.e. after deposition of 50000 atoms, there are already 4 impurities on average at $x = 95$. This is also depicted in Figure 2.13d, where the impurity density along the j axis can be seen. In Figure 2.13d I have averaged over 40 different configurations between 80x500 and 120x500 atoms deposited. The impurity gradient is constant. It’s distribution can be understood by the following estimation that by 10% impurity concentration, i.e. by

$$\rho_{imp} = 0.1,$$

50 lattice sites away from the step edge, at $j = 60$, the average number of impurities in a row should be 10% percent, i.e. if

$$L_i = 25$$

then on average 2.5 impurities should be in each row at $j = 60$. This estimate is fulfilled by the simulation results.

Using space-time plots, not only step-pairing can be studied but also formation of islands. Analysis of large numbers of simulations with different parameters means that the time development of the run should be analyzed for each run. This can be very efficiently done by using space-time plots for every simulation, indeed, this tool greatly helped me to categorize the simulations into the aforementioned four categories. Another example, how island formation after step-pairing can be easily detected using space-time plots can be seen in Figure 2.14.

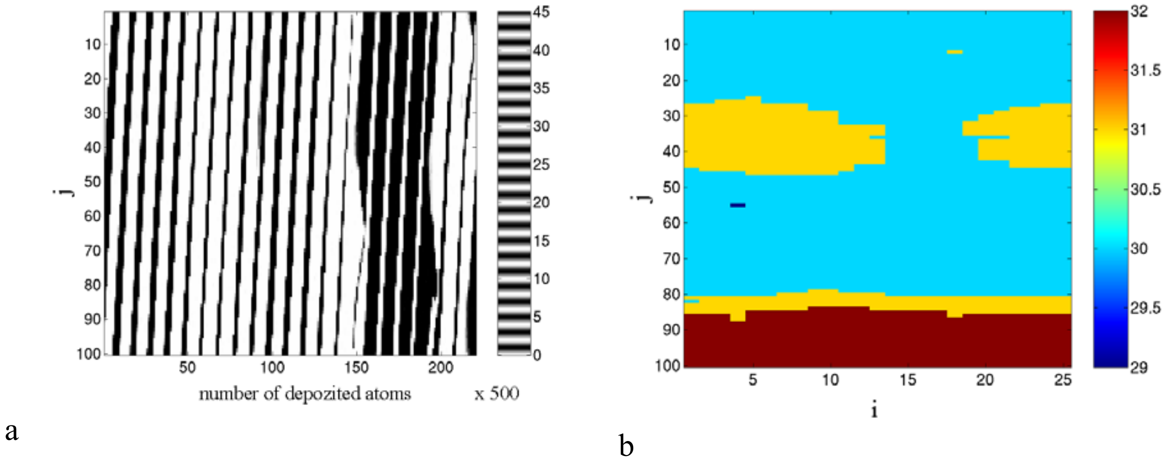

**Figure 2.14. Island formation after step-pairing. Space-time plot (a) is an excellent tool for the investigation of the time-development of island formation after step-pairing. The corresponding height profile after deposition of 150x500 atoms can be seen in Figure b. The system parameters are the following:**

$$L_i = 25; L_j = 100; \rho_{imp} = 0.05; J = 40; J_{imp} = 4; R_{growth} = 400 .$$

After examining the space-time plots for the simulations of interest and making sure that no island formation takes place, it is possible to measure the step distances by measuring the terrace sizes. By counting how many sites there are with a given height in the system. Using this method I have depicted the time development of terrace sizes in six different simulations in Figure 2.15. Development of step sizes during step-pairing, the same simulation as depicted in Figure 2.12 and Figure 2.13, can be seen in Figure 2.15d. Note that step-pairing takes place after the deposition of five-ten monolayers, this corresponds roughly to an average asymmetry of 5% in the adatom currents, as discussed previously in the case of the simple one-dimensional model system with constant adatom current asymmetry. In Figure 2.15a the time development of terrace sizes of a system with the same parameters as in Figure 2.15d is depicted, with the only difference that the initial condition corresponded to a situation where steps already formed pairs. The step pair is stable during the deposition of 20 monolayers, even the largest terrace size fluctuation is below 15%. Figure 2.15b the same simulation has been run as in Figure 2.15a, with the only difference that the impurities did not cause any change to the diffusion coefficient of adatoms. The terrace size fluctuations are larger, principally they could get as large as the system size allows since the change of terrace size can be described as a random walk. We can compare Figure 2.15a, Figure 2.15b and Figure 2.15c to observe how fast stabilizing impurities (impurities which speed up local diffusion) can push the system in a state with equidistant steps. It happens on a time scale needed to deposit five monolayers. If we compare Figure 2.15e and Figure 2.15f we can observe the suppression of fluctuations by impurities and the maintaining an equidistant step distribution.

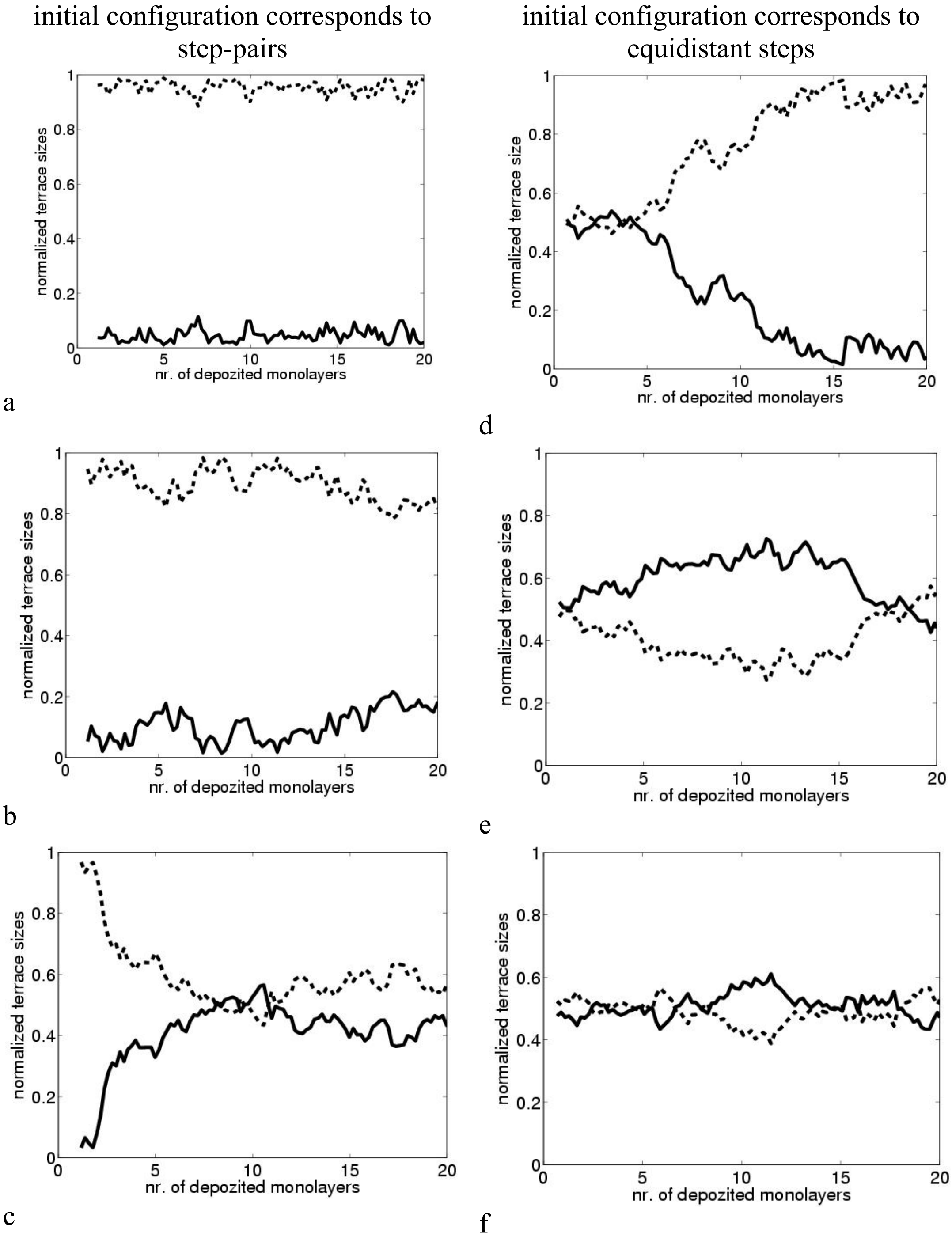

**Figure 2.15. Time development of normalized terrace sizes for (a,d) unstable, $J_{imp} = 4$, (b,e) marginal stable, $J_{imp} = 1$, (c,f) stable, $J_{imp} = 0.2$, cases. Only $J_{imp}$ was different in the three cases, other system parameters were the same:**

$$L_i = 25; L_j = 100; J = 40; \rho_{imp} = 0.1; R_{growth} = 800; N_{steps} = 2$$

### 2.3.3 Systems with three steps

In order to investigate the time-development of step-pairing and eventually formation of larger step bunches the size of the system has to be increased in the j direction, so that the average distance between steps stays the same as it was in the case of two-steps. Also the boundary condition and the analysis using space-time plots have to be changed. Instead of only using two colors already three colors are needed so that the space-time plots provide a good overview on the time-development of the system.

In Figure 2.16 space-time plots of different systems with three steps in the moving coordinate frame are depicted. The coordinate frame advances with the average step velocity. The marginal stable case, where impurities do not influence the local diffusion of adatoms is shown in Figure 2.16b. The terrace size development reflects an oscillatory behavior instead of following a random walk as it is the case if only two steps are present in the system. The periodic time of the oscillation corresponds to the time needed to deposit 50x500=25000 atoms, i.e. 6.6 monolayers. This periodic time is inherent to this system due to the coupling between the velocities of neighboring steps. Two neighboring steps share the same terrace from which the adatoms are collected by both steps. This introduces the coupling and leads to oscillatory behavior. The oscillations can be suppressed by stabilizing impurities as it can be seen in Figure 2.16a. In the case of destabilizing impurities we can observe step-pairing but no step-bunching. In order to observe step bunching the adatom flux to the descending terraces should be two times larger then arriving to ascending terraces, however the difference between the two currents is only about 10% as it has been estimated in the case of two steps. We can observe that the periodic time of the fluctuation as can be seen in Figure 2.16b did not change with respect to Figure 2.16c. The magnitude of the fluctuations became however larger, and also periodic step-pairing can be observed for a short amount of time. However these step-pairs dissolve due to the fact that the terrace size from which the step-pair collects the adatoms will change with time so that the step-pair dissolves. This means, that the terrace which feeds the lower step in the step-pair will get bigger than the terrace which feeds the upper step in the step-pair. This is exactly what happens Figure 2.16c for example after the deposition of 100x500=50000 atoms. The red terrace which feeds the lower step of the step-pair (red-blue transition line) becomes larger than the gray terrace which feeds the upper step in the step-pair (blue-gray transition line). Therefore the velocity of the lower-step will be larger than the velocity of the upper-step and the step-pair dissolves. In this simulation $J = 40$ which means that practically every adatom on the grey terrace feeds the upper step and every adatom on the red terrace feeds the lower step and this causes the steps to separate. In future work it would be interesting to investigate the case with lower $J$ so that the adatoms do not attach so strong to steps, therefore they can feed both steps, in that case it might be possible that only a small current difference as large as 10% makes a larger bunch of steps stable.

It could be also possible that in the case of more than three steps in a macroscopic system step-bunches can occur due to impurities because of more complex behavior similar to traffic jam on highways. Such step-bunches would be dynamically stable.

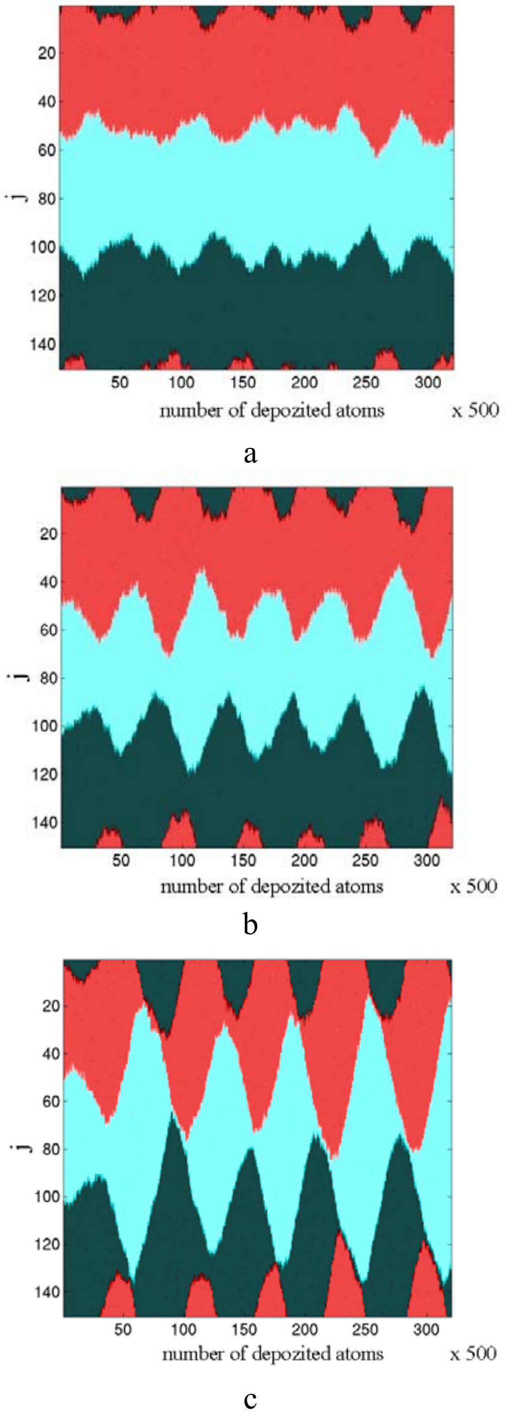

**Figure 2.16. Space-time plots in the moving coordinate frame for**

**(a) stabilizing,** $J_{imp} = 0.1$, **(b) marginal stable,** $J_{imp} = 1$, **(c) destabilizing,** $J_{imp} = 4$,

**impurities in a system with three steps. Note that oscillations arise in the marginal stable case due to coupling between step velocities because of shared neighboring terraces. Stabilizing impurities suppress oscillations while destabilizing impurities enhance oscillations but don't lead to step-bunching. Only step-pairing can be observed in Figure c and they are not stable. Different colors mean different heights: initially gray is zero, blue is one and red is three. Identical system parameters are:**

$$L_i = 25; L_j = 150; J = 40; \rho_{imp} = 0.1; R_{growth} = 800; N_{steps} = 3$$

To investigate such behavior there are two possibilities: either using a one-dimensional simulation where much larger systems can be treated (1000 steps) or using two dimensional kinetic Monte Carlo simulation where only a few the steps can be simulated in a reasonable amount of time. In the following section the case of eight steps will be examined to understand how step-pairs interact.

### 2.3.4 Systems with eight steps

In macroscopic systems there can be several thousands of steps, therefore to investigate their behavior and interactions it is important to simulate systems more than three steps. With more than three steps the effect of periodic boundary conditions do not play crucial role in determining the behavior of the system. In doing so a compromise should be made, so that the number of steps are as large as possible (this means increasing system size and computational effort) and the number of deposited atoms are enough to reach a stationary state. After trying different system sizes I have concluded that eight-steps are enough to compensate for the effect of the boundary conditions and it is small enough so that the system can reach a stationary state in one or two week of simulation time.

The motivation to simulate larger systems is to see whether the coupling between the terraces and the asymmetries in the adatom currents would lead to a dynamical step bunching, similar to the case of traffic jam on the streets.

Let us first examine the effect of stabilizing impurities. We expect that stabilizing impurities will cause stable equidistant step distribution during growth and suppress oscillations that would occur due to coupling of step velocities between neighboring steps via terraces. In Figure 2.17 we can see that such stabilization takes place indeed, the initial large fluctuations disappear. In case of destabilizing impurities just the opposite happens as it can be seen in Figure 2.18, however the patterns emerging are more complicated than in the three step case. The system is unstable against step-pairing but no larger step bunches can be observed. We can observe a wave in step-pairing. To recognize this, let us consider in Figure 2.18 the step-pair wave at four points, as summarized in Table 2.4.

| index | j position | number of atoms depozited |
|---|---|---|
| 1 | 340 | 250x500 |
| 2 | 240 | 310x500 |
| 3 | 150 | 370x500 |
| 4 | 40 | 410x500 |

**Table 2.4 A wave of step-pairs can be observed in Figure 2.18 when we follow the points from index 1 to index 4. The wave travels faster than the average step velocity this can be seen in the figure as with increasing number of atoms deposited the position of the step pair shifts towards the growth direction while the space-time plot in Figure 2.18 is compensated by the average step velocity (moving coordinate system).**

These four points lie along a line in Figure 2.18 and correspond to step-pairing wave. This wave characterizes the whole dynamics of the system and it’s presence can be seen during the whole deposition process.

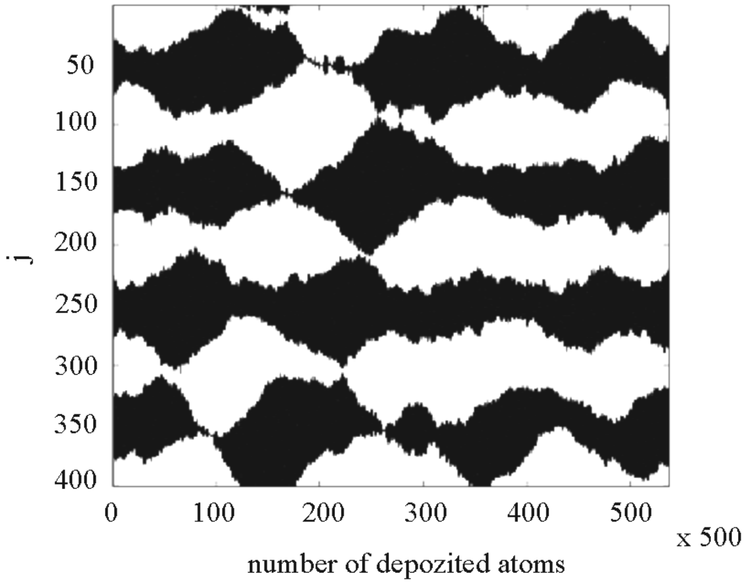

**Figure 2.17. Space-time plot for a system with eight steps and stabilizing impurities in the moving-coordinate frame is shown. After initial fluctuations, the step distanced are equalized by stabilizing impurities similarly to the case of three steps in the system. The parameters are the following:**

$$L_i = 25; L_j = 400; J = 40; \rho_{imp} = 0.1; J_{imp} = 0.2; R_{growth} = 1600; N_{steps} = 8$$

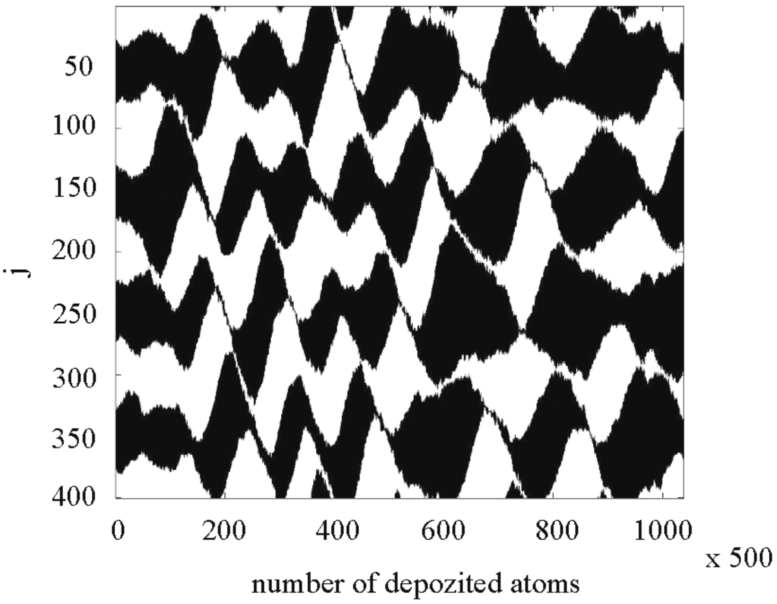

**Figure 2.18. Space-time plot made from the moving-coordinate system is shown to investigate the interaction of step-pairs. The time development of a system with eight steps and with destabilizing impurities can be seen. There is instability towards the formation of step-pairs. However, no sign of formation of step-bunches can be observed. Note the wave like propagation of formation and dissolution of step-pairs. The system parameters are:**

$$L_i = 20; L_j = 400; J = 40; \rho_{imp} = 0.1; J_{imp} = 4; R_{growth} = 1000; N_{steps} = 8$$

## 2.4 Conclusion

In this chapter I have presented the results of the first two-dimensional kinetic Monte Carlo simulation on a cubic solid on solid lattice to study the effect of immobile impurities on step-pairing and step-bunching. The model is specified by seven independent parameters, therefore, search for optimal parameter regime has been carried out first. In order to analyze and present the simulation results the time-development of the model systems were investigated using space-time plots and moving coordinate frames. These very effective tools were applied to characterize large number of simulation results.

For a better understanding of step-pairing first a one-dimensional analytic model system with constant adatom current asymmetry has been considered and the results have been compared with kinetic Monte Carlo simulations. It has been shown in the model system that step-pairing occurs if the impurities act as random barriers and terrace sizes equalize if the impurities enhance local diffusion. The terrace size development of a system with two steps without any impurities can be described by a random walk. Simulation results with two steps supported the predictions of the one-dimensional analytical model. Step-pairing occurred with destabilizing impurities and equidistant terrace sizes resulted from the presence of stabilizing impurities. Systems with three steps showed a more complicated behavior than the systems with only two steps because of the coupling between velocities of neighboring steps via shared neighboring terraces. As a consequence of this, the random walk description (in the case of no impurities and two steps) does not apply anymore to the system with three steps. Oscillations appear, which can be either enhanced by destabilizing or suppressed by stabilizing impurities. The system with impurities acting as random barriers is unstable against step-pairing but step-bunches of three steps are not stable because the magnitude of the current difference between adatom currents to ascending and descending steps is only about 10%. Systems with eight steps show similar behavior as systems with three steps, however the patterns in the space-time plots are more complicated because the systems are not constrained anymore so much by the periodic boundary conditions as they were in the three step case. No step-bunching can be observed in systems with eight steps, however the system is unstable against formation of step-pairs and also a wave like behavior of step-formation has been observed due to the coupling by terraces.

As a final conclusion, I have demonstrated that kinetic Monte Carlo simulation is an excellent tool to microscopically investigate the step-bunching and corresponding instabilities on surfaces. Results suggest that step-bunching cannot be caused by immobile impurities as believed before. Further study is needed to clarify this point.

## 2.5 Bibliography

[1] J. Krug, Europhysics Letters **60**, 788-794 (2002)
[2] O. Pierre-Louis and J.-J. Metois, Physical Review Letters **93**, 165901 (2004)
[3] M. Vladimirova A. Pimpinelli and A. Videcoq, J. of Crystal Growth **220**, 631-636 (2000)
[4] J. Krug, cond-mat/0405066
[5] D. Kandel and J. D. Weeks, Physical Review B **59**, 5554 (1993)
[6] E. T. Croke, F. Grosse, J. J. Vajo, M. F. Gyure, M. Floyd, and David J. Smith, Applied Physics Letters **79**, 1310 (2000)
[7] M. Sato and M. Uwaha, Surface Science **442**, 318-328 (1999)
[8] J.W. Haus and K. W. Kehr, Phys. Rep. **586**, 263 (1987)
[9] M. Sato and M. Uwaha, J. of the Physical Society of Japan **66**, 1054 (1997)
[10] V. Popkov, J. Krug, Europhysics Letters **72**, 1025 (2005)
[11] V. Popkov, J. Krug, cond-mat/0602216
[12] A. B. Bortz, M. H. Kalos, and J. L. Lebowitz, J. of Comp. Phys. **17**, 10 (1975)

# 3 Molecular dynamics simulation of preparation of amorphous semiconductors

## 3.1 Introduction

Technological importance of amorphous semiconductors draws researchers' attention more and more to investigate their structure because it determines all their unique and peculiar properties which are exploited in our everyday used devices. Hydrogenated amorphous Silicon is used in solar cells, in sensors and in TFT screens. A lot of songs and movies are stored using amorphous chalcogenides on rewriteable DVD discs. New generation of medical imaging detectors are currently being developed based on amorphous Selenium. To optimize such devices understanding the structure of amorphous semiconductors is essential.

Although a great deal of experimental effort is being invested in discovering the atomic structure of amorphous materials, no experimental technique can tell us the exact three-dimensional atomic arrangements. Computer modeling of amorphous structure gets more and more important because it helps to discover the structure and so to improve devices. Particularly, the computer simulation of the preparation procedure of amorphous materials is helpful because of two aspects. Firstly, it is more realistic to make the structural models using computers in the same way as it happens in experiments. Secondly, the influence of preparation methods and parameters on the structures can be studied and understood on an atomic level and based on this knowledge material preparation can be optimized. Motivated by these facts, I have developed the methodology to simulate the preparation of chalcogenide glasses and further proceeded with the existing work of K. Kohary on amorphous Silicon. I want to understand the behavior and structure of two of the most important amorphous model semiconductors: amorphous Selenium and amorphous Silicon. Based on these simulations the study of more complex amorphous structures will be later easier.

Computer aided structural modeling of amorphous semiconductors has been utilized for a long time. In the following I will summarize the most relevant works in this field and emphasize the importance of further research. My path has been pioneered by the molecular dynamics simulations of atomic deposition of carbon [1] and Silicon [2] which has been carried out by K. Kohary and S. Kugler starting in 1998. Concerning the case of Selenium, the model material of chalcogenides; there are although simulations which investigate its preparation and physical properties [3, 4, 5] using a recently developed empirical three-body inter-atomic potential [6], however the authors did not investigate the preparation of thin-films, whose understanding is important both to physics and technology. Since the accuracy of empirical potentials is poor, more accurate methods, such as tight-binding models have been also used in the recent years to study amorphous Selenium [7, 8, 9]. The tight-binding approach preserves the quantum mechanical description of bonding when compared to empirical methods but its drawback is the higher computational cost [10]. However, when compairing the tight-binding methods with the *ab-initio* techniques it can be concluded that tight-binding modeling is still much faster, but it has reduced transferability because of the approximations made. Recently, an excellent tight-binding model has been developed by Molina *et al.* which reproduces different crystal phases and gives good agreement with experiments [11, 12]. It is important to note, that beside molecular dynamics there is another important approach to make computer modeling of amorphous materials, that is the reverse Monte Carlo method. It has been efficiently applied to construct large computer models of amorphous materials based on diffraction data both for Selenium [13] and Silicon [14].

There are different reasons why I started to simulate the preparation of amorphous semiconductors. To my knowledge, there has been no molecular dynamics simulation of atomic deposition of amorphous Selenium before this work and the simulation of this process is important both from a technological and from a scientific point of view because molecular dynamics simulation offers deep insights into atomic processes and structure. Furthermore, a newly published tight-binding model provided the possibility to simulate amorphous Selenium accurately on a much longer timescale than previously was possible, increasing the power of molecular dynamics method and allowing simulation of processes which were very hard to simulate before. Similarly, in the case of Silicon, a recently developed tight-binding model promised a much more accurate description for amorphous phases than it was possible before because physical properties of crystalline phases and small atomic clusters were reproduced very accurately by the new method. My last motivation to study the preparation methods of amorphous materials was that based on the experience obtained in the structural simulations of amorphous materials other processes like the photo-induced phenomena can be investigated.

## 3.2 Molecular dynamics simulation

Molecular dynamics simulation might be the art of seeing atoms without looking at them. With molecular dynamics we want to simulate reality. Similarly, as the motion of a ball on the beach can be described by forces and by the corresponding Newtonian equations of motions, atoms in the materials can be thought of as balls on which forces act. This idea is known as the Born-Oppenheimer approximation. If the mass of the atoms are much larger than the mass of the electrons then the electronic and atomic degrees of freedom can be treated separately. Atoms can be described as point particles, on which forces act due to interactions between electrons and atoms. The forces can be deduced from approximate empirical formulas or from total energy calculations based on quantum chemical or density functional methods. The interaction between atoms is more complicated to describe than for example gravitation between planets because the potential energy of the system is not the sum of potential energy of atomic pairs. This is why even the simplest empirical formula to describe Selenium explicitly includes three-body interaction terms to reproduce correctly the directed covalent bonds. To integrate the Newtonian equations of motions several algorithms are available. The most widely used algorithm family are the Verlet algorithms [15]. I briefly outline why such algorithms are so popular. One of the simplest versions of these algorithm can be obtained by the following reasoning. Let

$$\vec{r}_i, \vec{v}_i, \vec{a}_i$$

denote the position, velocity and acceleration of a particle at the i-th time step. Based on Taylor expansion, the time development of the position of the particle can be described as the following

$$\vec{r}_{i+1} = \vec{r}_i + \vec{v}_i \Delta t + \frac{1}{2}\vec{a}_i \Delta t^2 + \mathrm{O}(3).$$

However, the accuracy of the expression can be greatly enhanced by adding the following equation

$$\vec{r}_{i-1} = \vec{r}_i - \vec{v}_i \Delta t + \frac{1}{2}\vec{a}_i \Delta t^2 - \mathrm{O}(3)$$

yielding the more accurate Verlet algorithm

$$\vec{r}_{i+1} = 2\vec{r}_i - \vec{r}_{i-1} + \vec{a}_i \Delta t^2 + \mathrm{O}(4).$$

$\Delta t$ is the time step used to integrate the Newtonian equations of motions. This should be at least one order of magnitude smaller than the typical time scale for atomic oscillations. One or two femtoseconds are generally used values in most conventional situations in molecular dynamical simulations of solids and liquids. The most important input to such simulations is the description of interatomic forces. In the following I am going to describe the potentials and tight-binding models used during my calculations.

### 3.2.1 Empirical interatomic potential to describe Selenium-Selenium interaction

Selenium is nonmetallic element, red in powder form, black in vitreous form, and metallic gray in crystalline form, resembling sulfur and obtained primarily as a byproduct of electrolytic copper refining. It is widely used in rectifiers, as a semiconductor, and in xerography. Its photovoltaic and photoconductive actions make it useful in photocells, photographic exposure meters, and solar cells. Its atomic number is 34; its atomic weight is 78.96; its melting point (of gray Selenium) is 217 °C; its boiling point (gray) is 684.9 °C; its density (gray) is 4.79 g/cm$^3$. Its most stable crystalline forms consist of chains or rings with a preferred bond angle about 100°.

The empirical three-body potential used in many of my simulations has been developed in 1996 by C. Oligschleger and her co-workers [6] with the intent to provide both realistic and simple description of Selenium-Selenium interaction, so that simulations with several thousands atoms become possible. The most common Selenium crystals are built up by either Selenium rings or infinite helical chains, in both structures every Selenium atom has two nearest neighbors and this unique property has to be reproduced by the interatomic potential. The authors have taken into account both small Selenium clusters and crystalline phases during the parameter fitting of the potential. Its analytical form is

$$U = \sum_{i<j} V_2(r_{ij}) + \sum_{i<j<k} h(r_{ij}, r_{kj,} \Theta_{ijk}),$$

where $V_2(r_{ij})$ is the two body term and $h(r,s,\Theta)$ is the three body term, $r_{ij}, r_{kj}$ represents interatomic distances and $\Theta_{ijk}$ stands for the angle between bonds i-j and j-k. The functions are given by

$$V_{2,3}(r) = a_{2,3}e^{\alpha r} + b_{2,3}e^{\beta r} + c_{2,3}e^{\gamma r} \qquad \text{if } r < 2.79\ \text{Å}$$

$$V_{2,3}(r) = d_{2,3}(r - r_{2,3})^5 + e_{2,3}(r - r_{2,3})^4 + f_{2,3}(r - r_{2,3}) \qquad \text{if } r < 2.79\ \text{Å} < r_{2,3}$$

$$V_{2,3}(r) = 0 \qquad \text{if } r_{2,3} < r$$

$$h(r,s,\Theta) = V_3(r)V_3(s)[b_1(\cos\Theta - \cos\beta_2)^2 + b_3 - 0.5b_1\cos^4\Theta].$$

The altogether 23 parameters are fitted to both experimental results and density functional calculations. The two-body potential has a minimum at 2.23 Å, which corresponds to the bond length of the Selenium dimer described in the framework of this potential, experimental value is 2.17 Å. It is interesting to note, that the vibration frequency of the Se dimer in MD simulation is 9.66 THz and experimentally it is 11.55 THz, this frequency is slightly underestimated by the potential. Therefore, by using a molecular dynamics time step of one femtosecond, it takes about one hundred molecular dynamics time steps to follow one period of the oscillation of the Selenium dimer. Let us consider now what happens if three atoms approach each other. If the distance between two atoms is smaller than 4.7 Å (4.7 Å $=2*r_3$) and a third atom is nearer to both atoms than 2.35 Å ($r_3$) then the purely repulsive three-body interaction begins to repel the three atoms so that this repulsion will be minimal at a bond angle of about 100°.

The potential has been carefully tested and compared to experimental results. The description of atomic geometries and bonding energies are excellent, weak point of the potential lies in the quantitative description of phonons and vibration properties, however the overall performance of the potential is outstanding when considering its effectiveness and simplicity.

### 3.2.2 Tight-binding models for Selenium

There has been several attempts to describe the interatomic interactions between Selenium atoms by semi-empirical quantum chemical models. In this paragraph I will describe the latest development in this area. Recently, a tight-binding model has been developed by D. Molina *et al.* [11,12] to overcome the problems of earlier tight-binding models: the problem of transferability. If a tight-binding model transferable it can describe different phases (with different atomic coordination) and molecules with the same parameterization. This has been achieved by D. Molina *et al.* by introducing a more complex description for the dependence of hopping integrals on the interatomic distances. In the following I will briefly describe the Molina model which are used in my simulations. In every molecular dynamics steps first I solve the eigenvalue equation to account for chemical bonding,

$$\hat{H}\overline{x}_i = \varepsilon_i \overline{x}_i\,. \tag{1}$$

$\hat{H}$ is the hopping matrix, $\overline{x}_i$ is the i-th eigenvector and $\varepsilon_i$ is the i-th eigenvalue. The total energy of the system is composed of two parts: attraction due to chemical bonding and repulsion between atomic cores, so the total energy reads as

$$E = \sum_{i<j} E_{rep}(r_{ij}) + 2\sum_{i<n_{occ}} \varepsilon_i \tag{2}$$

where $E_{rep}(r_{ij})$ is the repulsive part. Derivation of this expression from density functional formalism in the framework of a controlled approximation has been discussed by C. M. Goring and his coauthors in a review about tight-binding modeling of materials [10]. The repulsive part is pair-wise additive and has an exponential part

$$E_{rep}(r) = \varphi_0 (r_0 / r)^m \exp\{m[-(r / d_c)^{m_c} + (d_0 / d_c)^{m_c}]\} . \qquad (2)$$

The diagonal elements of the hopping matrix corresponds to the on-site energies of isolated atoms, so that the limiting case that atoms are far away from each other and are not interacting be described correctly, in that case all the off diagonal elements are zero. However, if the atoms are nearer than a given distance, the corresponding off-diagonal elements are approximated by angular terms [16, 17] multiplied by radial terms depending only the distance between atoms, its functional form is given by

$$t^{\alpha\beta}(r) = t_0^{\alpha\beta} (r_0 / r)^n \exp\{n[-(r / r_c^{\alpha\beta})^{n_c^{\alpha\beta}} + (r_0 / r_c^{\alpha\beta})^{n_c^{\alpha\beta}}]\} , \qquad (3)$$

$r$ is interatomic distance, $\alpha\beta$ denotes the relations between atomic orbitals, in case of Selenium only s and p orbitals are relevant, therefore, only four different functions are necessary to describe the radial factors of hopping integrals, these are $ss\sigma, sp\sigma, pp\sigma, pp\pi$. Detailed description of the origin of these terms can be found in the pioneering article on Linear Combination of Atomic Orbitals (LCAO) method written by Slater and Koster in 1954 [16]. To guarantee zero hopping between atoms at large distances these functions have a cutoff at 3.8 Å or at 4.0 Å depending on the particular function. The functions has to be smoothed at the cutoffs, so that forces can be calculated.

Molina and Lomba introduced a Hubbard like term to the tight-binging model to correct any large transfer, which they encountered after developing the model without the Hubbard-term: the charge-transfer was too large and too much coordination defects appeared in disordered phases as it is described in their first paper on this subject [11]. The Hamiltonian of the system was modified by adding the Hubbard term which quadratically depends on deviations from charge neutrality, i.e.

$$E = \sum_{i<j} E_{rep}(r_{ij}) + 2 \sum_{i<n_{occ}} \varepsilon_i + \frac{1}{2} U \sum_{i}^{N} (q_i - q_i^0)^2 \qquad (4)$$

$$q_i = 2 \sum_{n}^{n_{occ}} \sum_{\alpha}^{n_b} (c_{i\alpha}^{(n)})^2 . \qquad (5)$$

$c_{i\alpha}^{(n)}$ are the coefficients of the eigenfunction

$$\Psi^{(n)} = \sum_{i,\alpha} c_{i,\alpha}{}^{(n)} \varphi^{\alpha}(\bar{r} - \bar{R}_i) , \qquad (6)$$

$n$ indexes the one-particle eigenstates, $\varphi^{\alpha}(\bar{r} - \bar{R}_i)$ are the basis functions per atom and $\alpha$ stands for the components of the basis, in the case of Selenium these are

$$s, p_x, p_y, p_z . \qquad (7)$$

$U$ is the Hubbard parameter whose value is 0.875 eV. The main effect of this correction is that molecular dynamics simulations provide drastically longer chains in liquid and amorphous Selenium.

After finding $c_{i\alpha}^{(n)}$ which minimize Eq. (2), they can be used to obtain the forces. Namely, the part of the forces acting on atoms due to the valence electrons can be efficiently calculated using the Hellmann-Feynman theorem

$$\overline{F}_{ij} = \frac{\partial\left(-2\sum_{i<n_{occc}}\varepsilon_i\right)}{\partial\overline{R}_{ij}} = -4\sum_{\alpha\beta}\rho_{ij}^{\alpha\beta}\frac{\partial t^{\alpha\beta}(\overline{R}_{ij})}{\partial\overline{R}_{ij}} \tag{8}$$

where the partial density matrix is

$$\rho_{ij}^{\alpha\beta} = \sum_{n}^{n_{occ}} c_{i\alpha}^{(n)}c_{j\beta}^{(n)} \; . \tag{9}$$

### 3.2.3 Tight-binding models for Silicon

In 1994 Kwon *et al.* have published a transferable tight-binding model for Silicon [17]. However, as noticed by K. Kohary, the model provided six-fold coordinated defects in the amorphous phase [18]. Three years later, Lenosky *et al.* have developed a highly optimized tight-binding parametrization scheme for Silicon using cubic spline interpolation to model the radial part of the hopping integrals instead of exponential functions [19]. The potential has been tested in many different cases since than, however, no calculation has been carried out so far to - my knowledge - which investigates how well the promising new parametrization performs if disordered Silicon has to be described.

### 3.2.4 Development and testing the molecular dynamics program package ATOMDEP

ATOMDEP is the name of the program package which has been initially developed by K. Kohary and S. Kugler to simulate the preparation of amorphous carbon [1] and Silicon [2]. In order to simulate the preparation of Selenium and to improve the accuracy of the description of amorphous Silicon I have implemented the corresponding potentials for Selenium and Silicon. Before obtaining results from computer simulations the programs has to be tested carefully. I have checked that the binding energies of clusters and crystals given in the papers by the authors of the potentials agree with the values I have obtained using ATOMDEP. To check dynamical properties I have compared vibration frequencies, diffusion coefficients and melting points.

## *3.3 Comparison of different preparation techniques of amorphous Selenium using molecular dynamics simulation*

In experiments there are principally two different ways to prepare amorphous semiconductors: atomic deposition or rapid quenching from the liquid. An excellent overview on the preparation techniques can be found in the monograph by S. R. Elliott [20]. Different preparation techniques lead to different atomic structures, so to optimize materials for industrial applications it is important to understand and compare the atomic processes in both preparational methods and their dependence on physical parameters like bombarding energy. Among other structural properties, attention will be paid to defect formations such as coordination defects and voids. In this section, I have used an empirical interatomic Selenium-Selenium interaction potential for the molecular dynamics simulations because they allowed to create large structural models [6].

### 3.3.1 Selenium, the model material of chalcogenide glasses

Chalcogenide glasses are disordered solids, which contain a considerable amount of chalcogen atoms (S, Se and Te). In the stable condensed phases chalcogenide elements form covalent bonds with two nearest neighbours in accordance with the 8-N rule. These atoms have six electrons in the outermost shell with a configuration of $s^2p^4$. Electrons in *s* states do not participate in bonding since these states have energies well below the *p* states. Two covalent bonds are formed between chalcogen atoms by two *p* electrons, but the other electron pair - also called a lone pair (LP) – remains not bonded.

The structure of pure amorphous Selenium (a-Se) - a representative chalcogenide material - can be described as the random mixture of rings and helical chains accompanied by coordination defects. The trigonal phase consists of infinite helical chains and the building unit of the monoclinic phase is an eight-member Selenium ring. In these structures the bond length is close to 2.38 Å, the bond angle to 100° and the dihedral angle is close to 102°, these values remain preserved mainly also in the amorphous phase. One- and three-fold coordination defects (C1 and C3) play an important role in determining the physical properties of amorphous Selenium beside the disorder which is introduced by the random arrangement of chains and rings in the material. Neutron diffraction experiments have shown that the average coordination number remains close to two despite the presence of one and three fold coordinated atoms [13, 21]. According to Phillips-Thorpe model a-Se is considered to form an under-constrained network due to its average coordination number of two. In an amorphous structure, where coordination defects modify the continuous random network, the presence of dangling bonds is expected due to the existing unpaired electrons. However, no electron-spin-resonance (ESR) signal has been observed in a-Se. A possible explanation of this phenomenon is that the defects are not neutral: one-fold coordinated atoms are negatively charged (C1) and three-fold coordinated atoms are positively charged (C3) which are called valence alternation pairs (VAP's).

### 3.3.2 Simulation details

In Figure 3.1 the substrate used in the simulations is depicted. In order to mimic the crystalline phase and absorb the impulse of the incoming atoms the bottom 108 atoms was not enabled to move and they still could interact with other atoms via the empirical potential. The velocities of the remaining 216 substrate atoms were rescaled so that their temperature stays at a given value and not rises drastically when adatoms with kinetic energies corresponding to several thousand Kelvin degrees impinge to the surface.

Open boundary condition is used in the deposition direction and in the two other directions perpendicular to the bombarding direction periodic boundary conditions are applied. The structure of the substrate corresponds to the trigonal phase of crystalline Selenium, where infinite helical chains are aligned parallel to each other. The incoming atoms were placed randomly above the substrate with the smallest possible Z-coordinate. The direction of the velocities of the incoming atoms were uniformly distributed in a cone with an opening angle of 60°. Illustration of the geometries can be seen in Figure 3.2. The angles are determined using the following formula

$$\phi = 60° + 60° \times p \tag{10}$$

$$\varphi = 360° \times q \tag{11}$$

$p$ and $q$ are uniformly distributed random numbers between 0 and 1.

Before beginning to simulate the deposition of atoms it is important to make sure that the substrate is stable in the investigated temperature regime. For the following simple test I let all the 324 substrate atoms to move freely, so that the temperature distribution being as homogeneous as possible. In Figure 3.3 the time development of average mean square displacement of Selenium atoms can be seen,

$$R_{MSD}(t) = \frac{1}{324}\sum_{i}^{324}\left|\bar{r}_i(t) - \bar{r}_i(t=0)\right|^2 , \tag{12}$$

where i indexes the atoms.

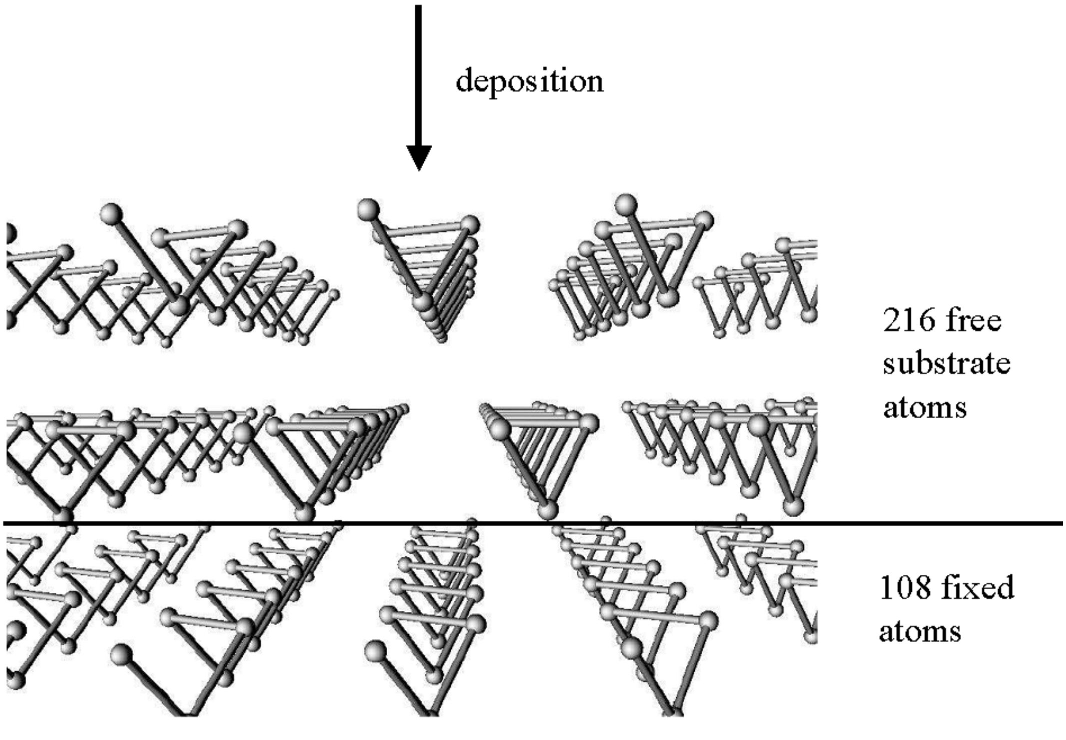

**Figure 3.1 Trigonal crystalline phase of Selenium used as substrate in the simulations of atomic deposition of amorphous Selenium. To compensate for the momentum of incoming atoms the 108 atoms at the bottom part of the substrate were fixed. 216 atoms at the top of the substrate were held at constant temperature by rescaling the velocities of the atoms.**

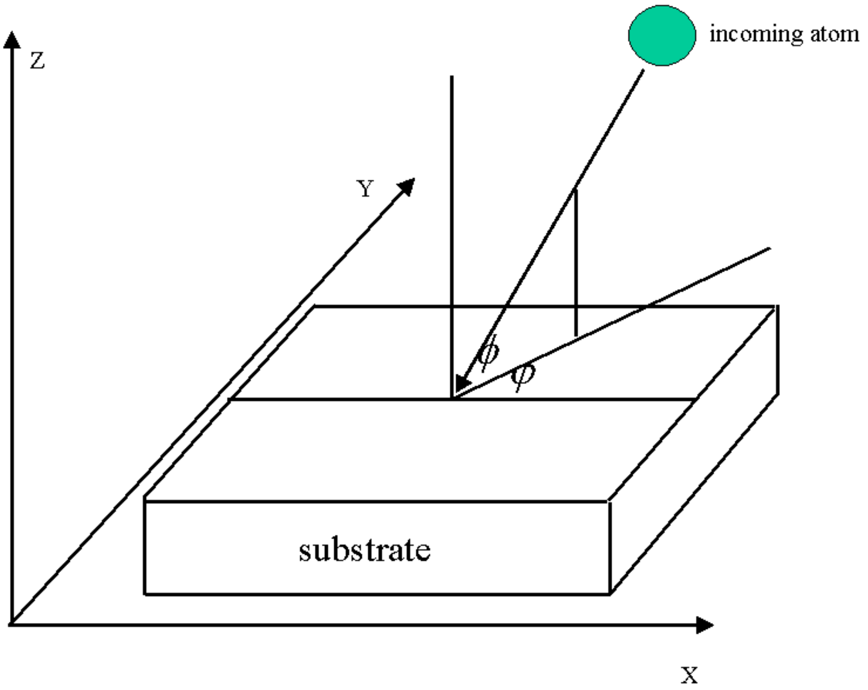

**Figure 3.2 Schematic representation of atomic deposition to the surface. Directions of incoming velocities are random except that incident angles smaller than 60° are not allowed.**

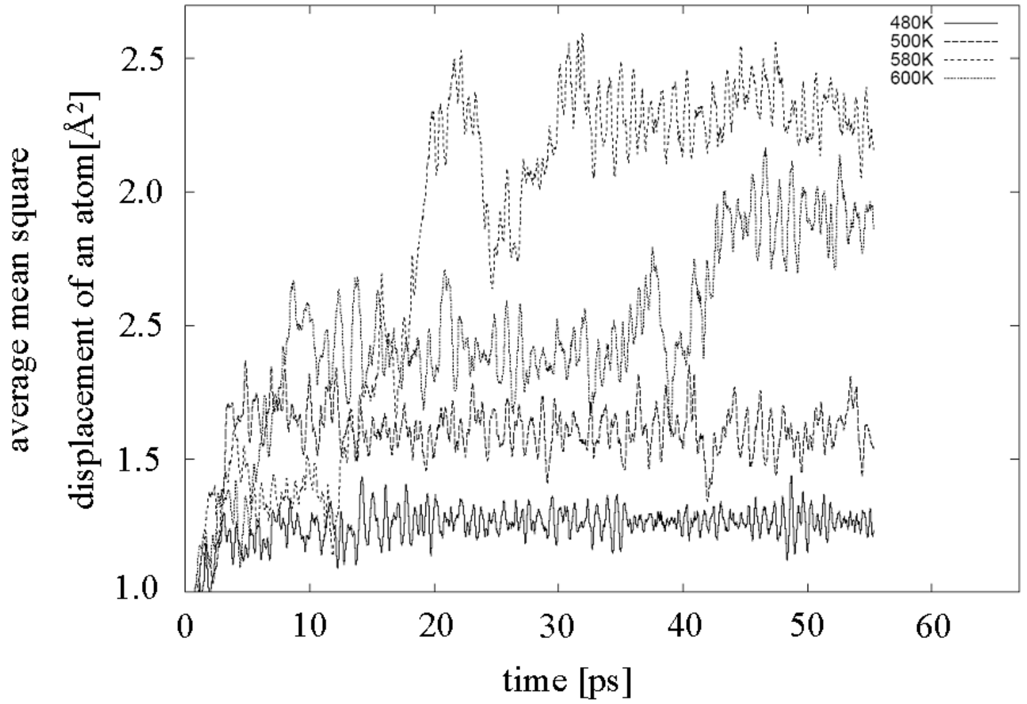

**Figure 3.3 Stability of the substrate at different temperatures. Average mean square displacement of an atom as a function of time is displayed. Note, how increasing temperature increases the average displacement per atom. Large fluctuations are due to chains which begin to rotate and covalent bonds do not break.**

Note that increasing temperature means increasing amplitude for atomic vibrations around the minimum of the potential valleys, however, the large jumps in the functions at higher temperatures are explained by rotation of a whole chain, i.e. the attractive inter-chain interaction is too weak to hold the orientation of the chains at higher temperatures. Melting point of Selenium is 494 K. This corresponds to the phenomenon that chains begin to diffuse and covalent bonds stay inert. By increasing the temperature to 800 K the increase in the average mean square displacement as time elapses changes drastically compared to the lower temperature cases discussed above. Substrate is unstable at 800 K as it can be seen in Figure 3.4.

After depositing about thousand atoms, it turns out in the first run, that the system explodes due to not sufficient heat conductance of amorphous Selenium which makes it necessary to introduce a more effective way to cool the system. To illustrate this situation a snapshot of the system is depicted in Figure 3.5. The figure shows the structure after having deposited 1500 atoms in about half nanoseconds. It can be seen that atoms evaporate due to the high temperature. The temperature of the substrate is 100 K, the kinetic energy of the incoming atoms is 2.5 eV (this value can be easily reached in experiments where additional electric field is present to increase the velocities of bombarding atoms). This high energy flux cannot be conducted through amorphous Selenium. The problem arises only after the deposition of several hundred atoms as it can be seen in the movie made about the simulation process. Although, only the heat conduction caused by phonons is included in molecular dynamics simulations, the heart of the problem is not the underestimation of the heat conduction but the too high energy flux.

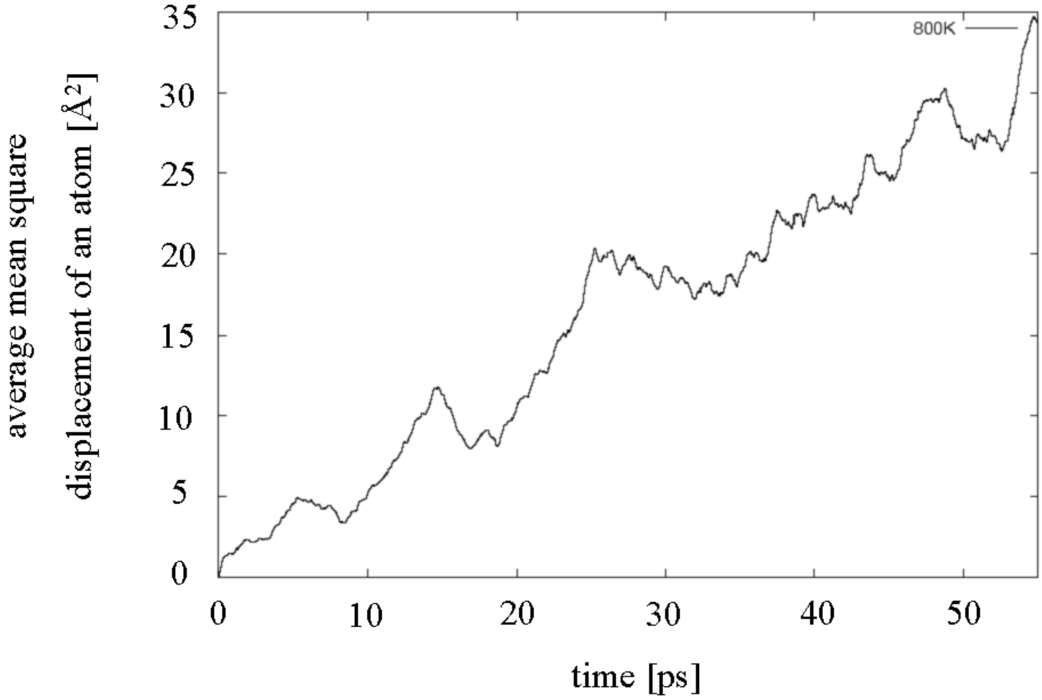

**Figure 3.4 Substrate is unstable at 800 K as can be seen from the time dependence of the average mean square displacement. This indicates that dissipation of heat will be an important issue during deposition to keep the system stable.**

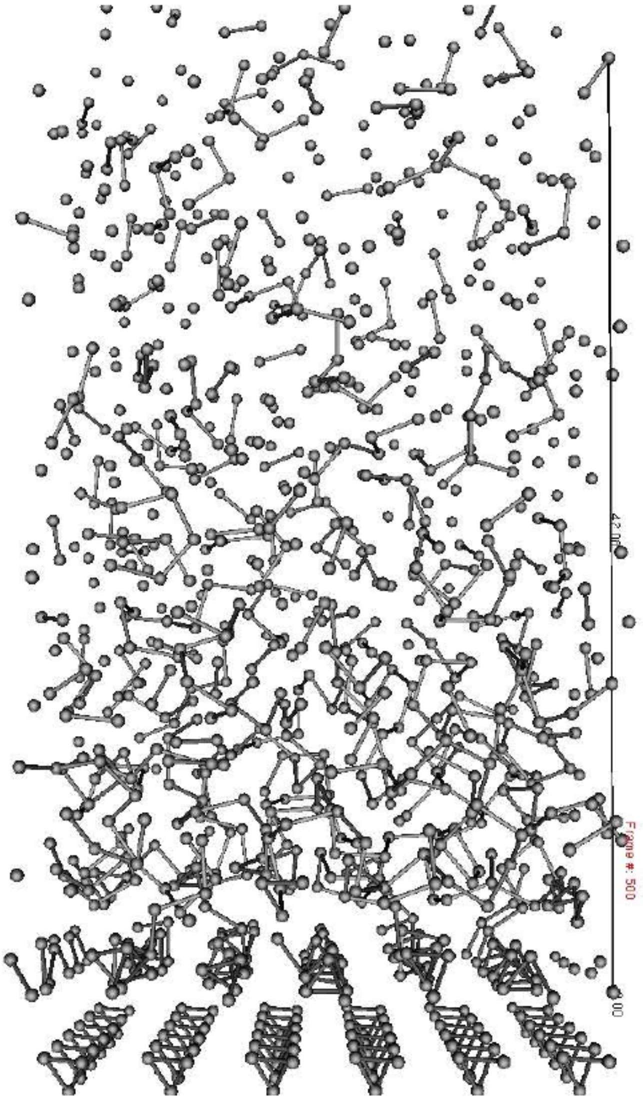

**Figure 3.5. Snapshot of the system after deposition of 1500 atoms to a crystalline substrate consisting of 108 fixed atoms (chains at the bottom) and 216 free-atoms whose velocity was rescaled to provide an average temperature of 100 K. Every 300 fs a new bombarding atom was introduced with 2.5 eV bombarding energy. In the snapshot atoms are considered to be bonded if their distance is smaller than 2.8 Å. The heat conductance of the amorhous layer above the substrate is not high enough and the surface of the film can not cool down even though the temperature of the substrate was held at 100 K. The surface of the substrate melts and evaporates. This shows that additional cooling has to be implemented in the algorithm.**

In experiments, couple of hundred monolayers can be grown per second, which is orders of magnitude smaller than the smallest possible deposition rate that can be modeled using molecular dynamics simulation. The reason for that is the simulation time of one-thousand atoms to follow one nanosecond in the computer takes a few of weeks on a single processor.

To compensate for the small heat conduction and large energy flux it is necessary to introduce the concept that the atoms which made a chemical bonding to the substrate became part of the substrate. This is useful because the substrate can be hold at constant temperature and the velocity of the substrate atoms are always rescaled so the temperature of the substrate corresponds to the prescribed value. This means that the number of substrate atoms in the system rises from 216 gradually, as more and more atoms attach to the substrate. An atom is considered to be bonded to the substrate if its distance is nearer to any substrate atoms than the cutoff of the interatomic potential. This means that an atom becomes a substrate atom even if it comes closer to the newly grown part of the substrate but it does not come close to any of the 216 atoms in the original substrate. This way of enhancing the cooling of the substrate has been already used to grow amorphous Silicon by K. Kohary [18].

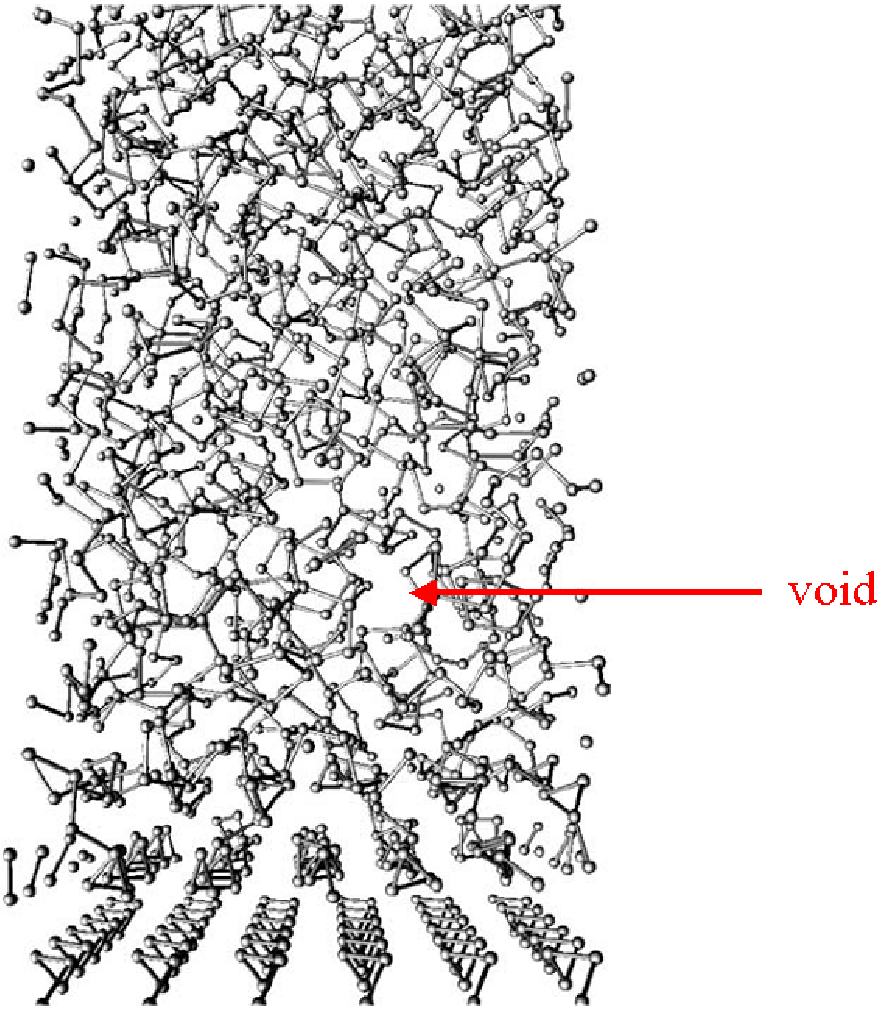

**Figure 3.6. Three dimensional view part of the amorphous Selenium structure grown using the growing substrate algorithm. The bombarding energy is 1 eV and the substrate temperature is 100 K. In every 300 fs a new bombarding atom was introduced. The lowest 108 atoms in the substrate are fixed to mimic the bulk crystalline phase. The substrate growing algorithm has fixed the problem with the too high energy flux. Note that there are voids in the structure.**

This method is extremely effective and introduces the extra cooling in a very natural way, since it is the substrate atoms whose temperature is reduced so that the kinetic energy of the newly arriving atoms decreases gradually. In the movie made on the deposition process it can be seen that bonds on the surface can be broken by the newly arriving atoms and they even penetrate below the surface, however the structure is solid even after the deposition of 1500 atoms, as it can be seen in Figure 3.6, in a snapshot that was taken during growth. To monitor the temperature and the stability of the structure during growth I have cut the system into 5 Å thick slices, perpendicular to growth direction. I measured the temperature and the number of atoms in these layers as a function of time during growth and plotted them in Figure 3.7. The substrate temperature is set to 100 K. However, the temperature of the surface is about 400 K as it can be seen in Figure 3.7 by looking at the red curve corresponding to the slice between 35-40 Å. After this layer has been filled up at 0.35 nanosecond, its temperature is about 300 K. Note the strong temperature gradient in the substrate, at the surface it can reach even 50 K / Å. As a conclusion, it can be said that the growing substrate technique can compensate efficiently for the too high energy flux due to extremely high deposition rate, however the temperature of the surface will be higher than the average temperature of the whole substrate due to the strong temperature gradient.

Insight into the dynamics of the growth can be obtained by displaying the maximal force acting in the system as a function of time as it can be seen in Figure 3.8. New bombarding atoms with 1 eV kinetic energy are introduced to the system every 300 fs, as they arrive on the surface peaks in Figure 3.8 can be observed. Small amplitude side peaks after the main peaks can be seen, they correspond to subsequent collisions.

It can be seen that the largest atomic force in this time interval is ten times larger than the maximal atomic force in the system if there are no collisions into the surface. These intervals can be seen as plateaus in the graph, for example at 30900 fs. The reason why the distance between the peaks is not exactly 300 fs is the following. Although every new atom is introduced after 300 fs, but their placement is random and also the amorphous surface is random therefore their time of impact will be different, so the peaks will not follow each other with exact 300 fs intervals.

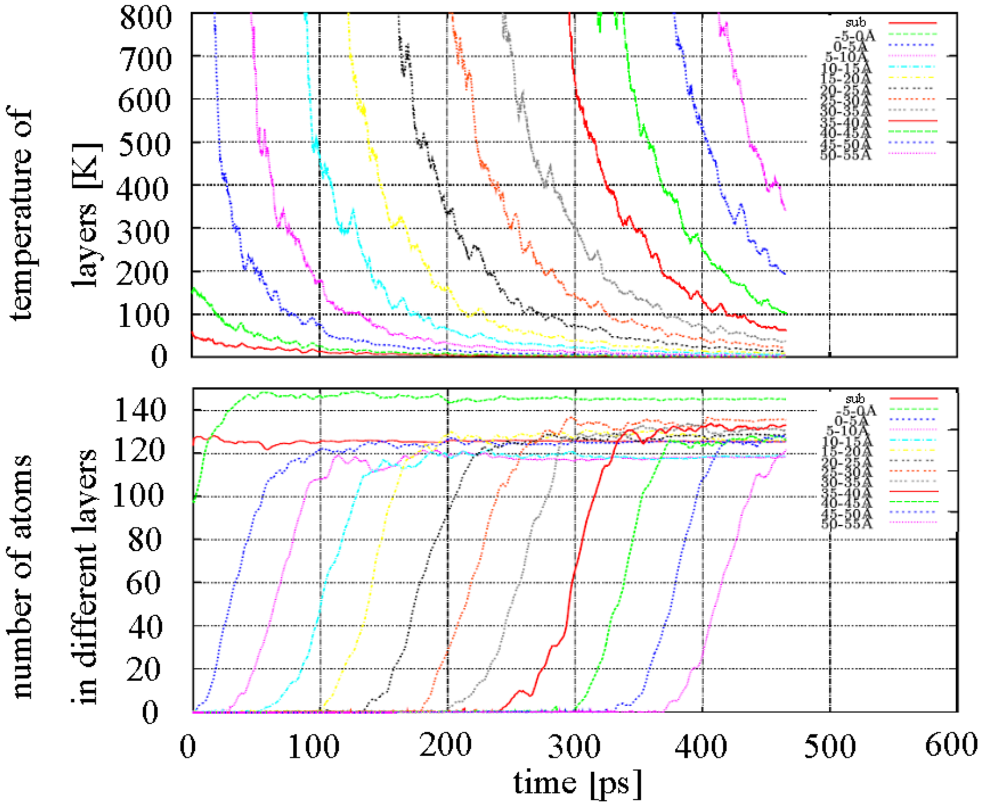

**Figure 3.7. Time development of temperature (upper panel) and number of atoms (lower panel) in subsequent 5 Å thick layers during growth with 1 eV bombarding energy and 100 K substrate temperature. A new bombarding atom was launched to the surface in every 300 femtosecond.**

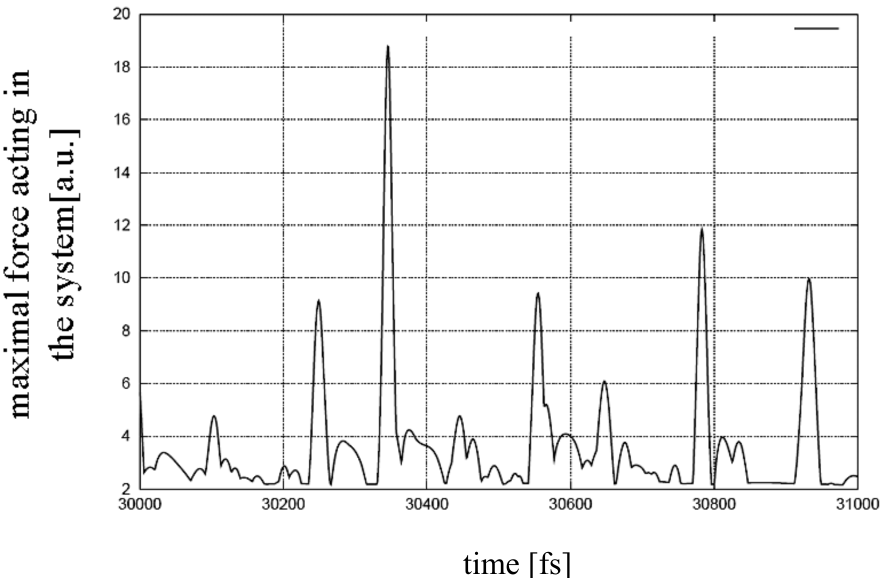

**Figure 3.8 Illustration of collisions due to atomic deposition. Large peaks correspond to primary collisions as bombarding atoms arrive at the surface. Satellite peaks are due to secondary collisions either made by the bombarding atom, or by the atom with which the bombarding atom collided during the primary collision. The time needed for the maximal force to settle down to equilibrium value is about 200 fs.**

### 3.3.3 Bombarding energy dependence of amorphous structures

#### 3.3.3.1 Difference in growth kinetics

In Figure 3.9 a drastic difference can be seen between the growth kinetics of two different simulations with different bombarding energies (0.1 eV and 1 eV). In case of lower energy the bombarding atoms have a higher tendency to be backscattered, therefore the effective growth rate is smaller in the case of smaller energy although in both cases in every 300 fs a new bombarding atom was introduced. The inclination of the curves are different. Smaller inclination can be seen in the smaller energy case. This reflects a smaller effective growth rate, but it also shows that the sample prepared with smaller bombarding energy is more porous during deposition, it tends to have more voids and these voids fill up slowly as time goes on. The kinetics of the growth is different because in the 0.1 eV case two or three slices grow at the same time and in the 1 eV case one slice fills up after another. To illustrate this, let us consider layers with 100 atoms and the layers above. In the case of 1 eV let us consider the black line corresponding to the layer between 20 Å and 25 Å at 200 ps, it contains about 100 atoms. The above layer between 25 Å and 30 Å contains about 30 atoms. This is the typical ratio for the 1 eV case. More drastic difference can be seen in the 0.1 eV case where we can find neighboring layers with nearly the same amount of atoms, as for example in the case of the yellow curve, between 15 Å and 20 Å and blue curve, between 10 Å and 15 Å in the top subfigure in Figure 3.9. Therefore, in the case of 0.1 eV growth the densities of the layers saturate slower, which reflects that the surface is more porous during growth.

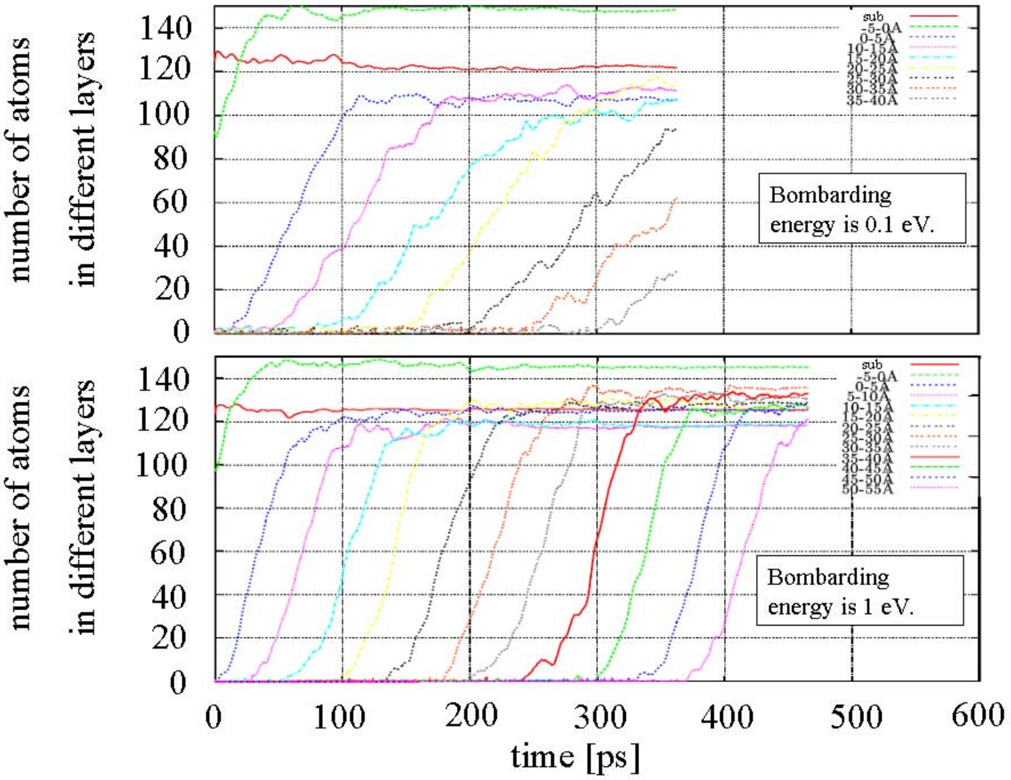

**Figure 3.9 Comparison of time development of two growth kinetics with different bombarding energies (0.1 eV – upper panel and 1 eV – lower panel). All other bombarding parameters are identical, substrate temperature is 100 K and incoming flux is 1/300 atom per femtosecond. Differences are twofold. Firstly, the backscattering in the 0.1 eV case is large, it is about 40%, while in the 1 eV case it is smaller than 5%. Secondly, the subsequent layers in the 0.1 eV case grow more simultaneously than in the 1 eV case. Note that in the upper panel, in the 0.1 eV case if a layer has 80 atoms then the layer below has always more than 20 atoms in it (i.e. blue and yellow line), however in the case of 1 eV bombarding if a layer has 80 atoms then the layer below it has always less than 20 atoms.**

### 3.3.3.2 Structural analysis

I have prepared three different structural models with different bombarding energies. I name them as SeStr0.1, SeStr1 and SeStr10, corresponding to bombarding energies of 0.1 eV, 1 eV and 10 eV respectively. All other preparation parameters were the same, the temperature of the substrate was 100 K , deposition flux corresponded to one deposited atom per 300 fs. In order to analyze only the amorphous part of the system I had to pay special attention to boundary conditions. Only atoms are considered in the structural analysis which are not effected by the substrate or the surface of the amorphous film, these atoms are called bulk atoms. In Table 3.1 I have summarized the number of total atoms and number of bulk atoms in the structures. After relaxation of the samples I have compared the pair correlation functions of the models because this quantity can be directly compared with experiments. There are no differences between the pair correlation functions of different models, however the experimental results [21] differ from results obtained from the modeling, the comparison between pair correlation function of model SeStr1 and experimentally determined pair correlation function of amorphous Selenium can be seen in Figure 3.10.

| model | total number of atoms | number of bulk atoms |
|---|---|---|
| SeStr0.1 | 954 | 509 |
| SeStr1 | 1016 | 584 |
| SeStr10 | 822 | 373 |

**Table 3.1. Total number of atoms and number of bulk atoms. Bulk atoms are the atoms which are between the following two Z coordinates: 5 Å above the uppermost substrate atom and 5 Å below the uppermost atom in the grown layer.**

The theoretical curve compared to the experimental one gives a too narrow first and second peak. The reason for this lies in potential, although if the number of coordination defects is high in the experimental model a wider first peak can be expected due to coordination defects which have longer and shorter bond lengths. The authors of experimental articles [13, 21] claim that very long chains are expected to exist in amorphous Selenium based on simulations. This estimate is also supported by the density functional calculations of liquid Selenium by G. Kresse [22]. They have reported a very low coordination defect density in liquid Selenium. Although liquid and solid phases are different it can be expected that a Selenium glass prepared by liquid quenching will have less defects than in liquid phase.

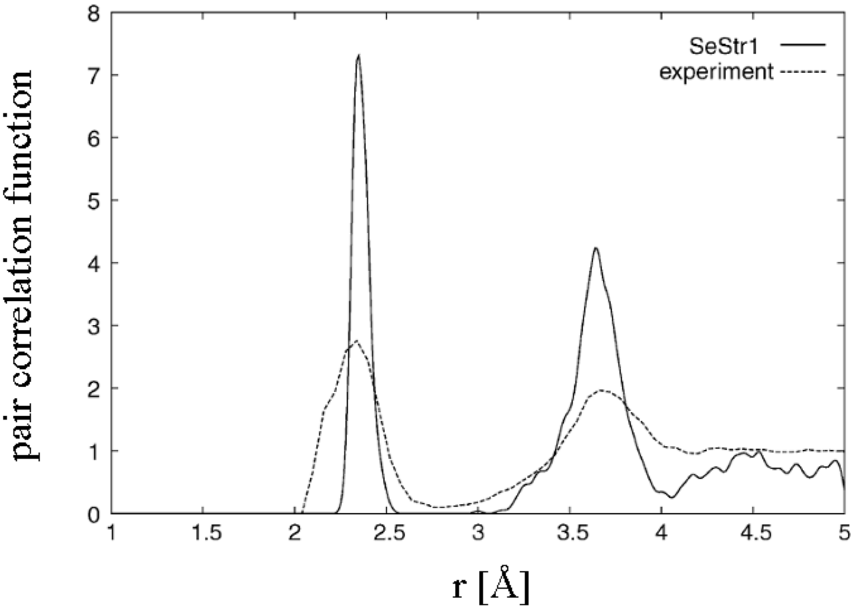

**Figure 3.10. Comparison of pair correlation functions of model SeStr1 and neutron diffraction experiment evaluated by reverse Monte Carlo modeling [21].**

To analyse the effects of coordination defects on bond lengths I have prepared Table 3.2 to compare bond lengths of different type of Selenium-Selenium bonds. For example $Se^2$-$Se^3$ bonds, i.e. bonds between atoms with two-fold and three-fold coordination are longer than $Se^2$-$Se^2$ bonds. Therefore, higher number of coordination defects could lead to increase the width of the first neighbor peek. It can be seen that bombarding energy does not influence the average bond length in either models. A very small increase can be seen in bond length of $Se^3$-$Se^3$ bonds as bombarding energy decreases as a consequence of density increase as later will be discussed, however the significance of this observation is poor because of the small number of three-fold coordinated effects (10-20% of the atoms).

| model | Se-Se [Å] | $Se^2$-$Se^3$ [Å] | $Se^3$-$Se^3$ [Å] | $Se^2$-$Se^2$ [Å] |
|---|---|---|---|---|
| SeStr0.1 | 2.37 | 2.41 | 2.48 | 2.35 |
| SeStr1 | 2.37 | 2.41 | 2.47 | 2.35 |
| SeStr10 | 2.37 | 2.41 | 2.46 | 2.35 |

**Table 3.2 Bond lengths and their dependence on coordination numbers.**

To discover how coordination defects are influenced by the change of bombarding energy in different models, I have made a detailed analysis on the relaxed structure and presented the results in Table 3.3. The average coordination number in a-Se is slightly higher than two. There is no fourfold coordinated Selenium atom but I found three-fold and one-fold coordinated atoms (defects) in every models. We can see a decrease in the relative number of three fold coordination defects as the bombarding energy increases. There are about five-ten times more three-fold coordinated defects than one-fold coordinated defects. Based on density functional and tight-binding results  the number of defects should be about one percent [12]. The increase of the three fold coordinated atoms with decreasing bombarding energy can be a consequence of decreasing density as it can be seen in Table 3.4. For crystalline α, β, and metallic Selenium the densities are equal to 4.4 g/cm$^3$, 4.35 g/cm$^3$ and 4.8 g/cm$^3$ which are larger than the values we obtained for a-Se, i.e. my molecular dynamics simulation provided lower dense structures.

| model | Z=1 | Z=2 | Z=3 | Z=4 |
|---|---|---|---|---|
| SeStr0.1 | 2 (1%) | 432 (85%) | 75 (14%) | 0 (0%) |
| SeStr1 | 1 (1%) | 516 (88%) | 67 (11%) | 0 (0%) |
| SeStr10 | 1 (1%) | 332 (89%) | 40 (10%) | 0 (0%) |

**Table 3.3 Number of coordination defects in different models. Increasing bombarding energy decreases the number of three-fold coordination defects. There are mainly three fold coordinated defects in all models, number of one-fold coordinated defects is very small in every case.**

| model | density [g/cm$^3$] |
|---|---|
| SeStr0.1 | 3.21 |
| SeStr1 | 3.73 |
| SeStr10 | 4.34 |

**Table 3.4 Comparison of densities of different models. Densities increase with increasing bombarding energy.**

### 3.3.3.3 Comparison of bond angles and bond lengths with diffraction measurements on Se molecules

To compare the local arrangements obtained by molecular dynamics simulations to experiments I have additionally analysed the structure of molecules containing -Se-Se- and -Se-Se-Se- fragments. This systematic analysis of structural data has been carried out using the Cambridge Structural Database (CSD) [23], which is the world's largest database of experimentally determined crystal structures containing the results of X-ray and neutron diffraction studies. CSD is designed as a critically evaluated numerical resource, containing three-dimensional atomic coordinates. In Figure 3.11 the bond length distributions in the simulated Str1eV model and the corresponding distribution of 551 molecules containing -Se-Se- bonds are compared. The shape of the two curves are surprisingly similar, however the experimentally determined bond lengths are shifted to lower values with 0.1 Å compared to values obtained from the Se1eV model.

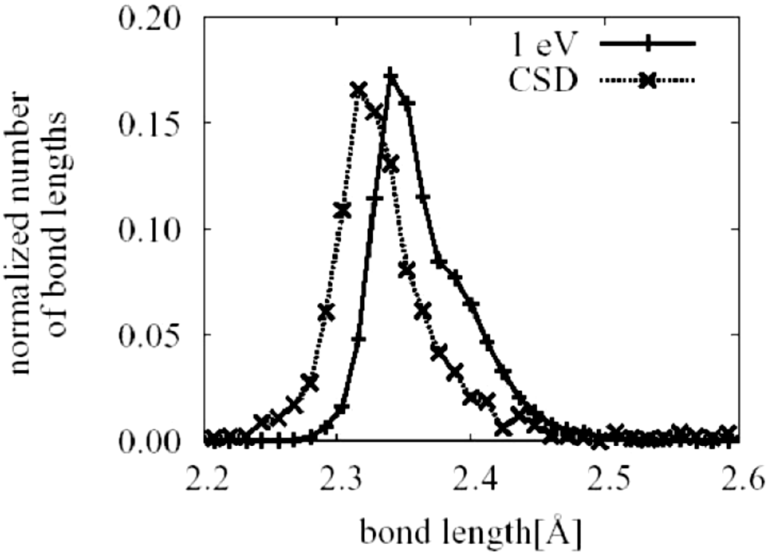

**Figure 3.11 Differences between the bond length distribution in the simulated Str1eV model and the corresponding distribution obtained using 551 different molecular structures which contained Se-Se bonds.**

To analyse bond angles I investigated molecules containing –Se-Se-Se– fragments, I have found an interesting correlation in the experimental data: larger bond angles correspond to smaller bond lengths on average. This can be seen in Figure 3.12. Each point represents a measured bond angle as a function of bond length. The majority of the points fall in the expected region, i.e. around 2.35 Å and 102°. The minimum bond length is 2.09 Å while the maximum is 2.58 Å. The bond angles lie inside the interval 79-114°. A histogram of calculated bond angles in one of my model along with the corresponding histogram obtained using the Cambridge Structural Database is displayed in the Figure 3.13. The main contribution to the bond angle distribution arises from angles between 95° and 110° in my model which is in a very good agreement with the experimental histogram. In α Selenium the bond angle is 103.1° [24] which is larger than the average value in my simulations (102.1°). Comparison of average bond angles depending on the coordination of central atom can be seen in Table 3.5. Bond angles at three-fold coordinated atoms decrease compared to two-fold coordinated counterparts in every model.

| model | Se-Se$^3$-Se | Se-Se$^2$-Se | Se-Se-Se |
|---|---|---|---|
| SeStr0.1 | 100.9° | 102.69° | 102.08° |
| SeStr1 | 100.97° | 102.68° | 102.2° |
| SeStr10 | 101.08° | 102.68° | 102.25° |

**Table 3.5 Bond angle dependence on coordination of the central atom. Bond angles at three-fold coordinated atoms decrease compared to two-fold coordinated counterparts in every model.**

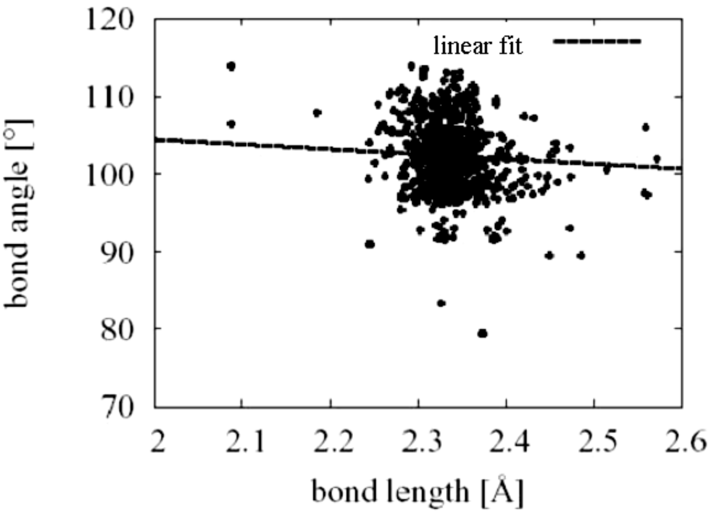

**Figure 3.12 Bond lengths and bond angles of –Se-Se-Se- fragments in molecules whose structure was determined by diffraction measurements (Cambridge Structural Database). Bond angles depend on bond lengths: larger bond lengths tend to reduce corresponding bond angles.**

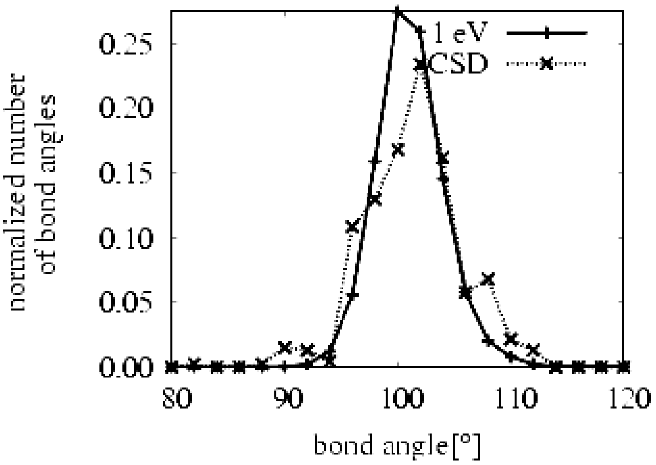

**Figure 3.13 Comparison of distribution of bond angles in a simulated model (Str1eV) and in molecules containing –Se-Se-Se- fragments found in the Cambridge Structural Database (CSD). Bond angle distributions of different models are very similar, therefore only that of model Str1eV is depicted as a representative curve.**

### 3.3.3.4 Density profiles, voids, lack of memory effect

Depending on the deposition flux and temperature it is possible to prepare both crystalline and amorphous materials. In accordance with this idea, in the work of K. Kohary it has been noted that near to the substrate the amorphous structure remembers the crystalline structure. A so called memory effect has been reported both in the case of amorphous carbon [1] and amorphous Silicon [18]. Therefore, it is expected that in the case of Selenium memory effect can be observed, however despite all the tedious search for this effect I have not found any evidence that it exists in the three investigated models.

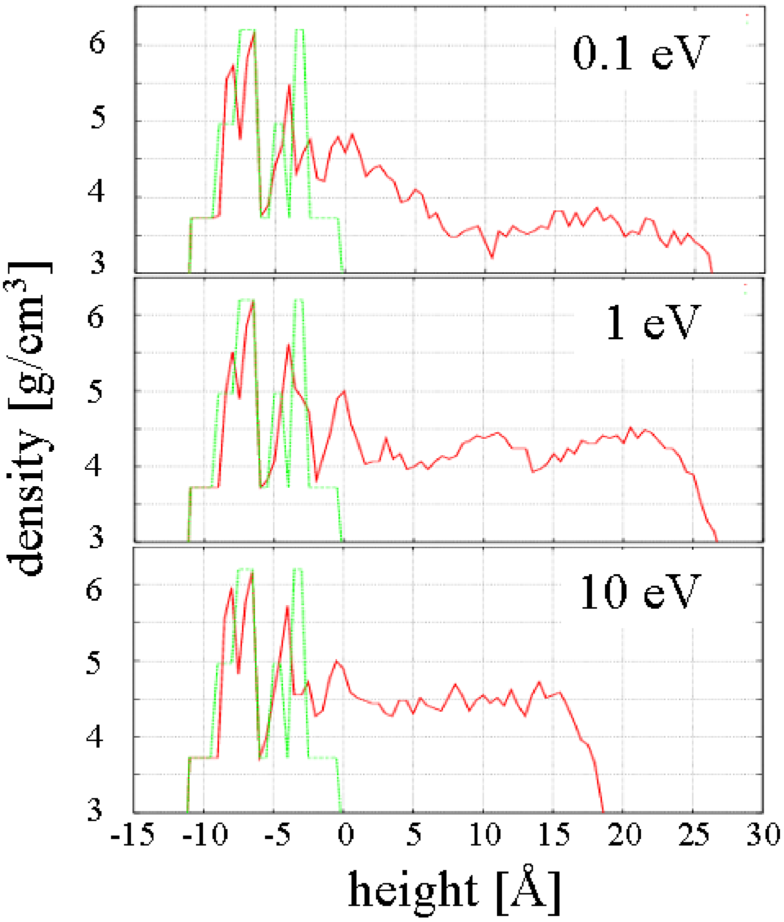

**Figure 3.14 Density profiles in different models with different bombarding energies (0.1 eV, 1 eV and 10 eV) Green curves represent substrates while red ones the amorphous structures. The curves are moving averages over 5 Å, this means that for example in the case of 1 eV bombarding energy (middle panel) at 10 Å the curve has the value 4.48 g/cm$^3$, which means that the average density of the layer between 5 Å and 10 Å is 4.48 g/cm$^3$.**

I have searched for a memory affect not only in the density distribution (Figure 3.5) but also in the orientation of the bonds and I concluded that no such effect is present in amorphous Selenium. The density profile delivers important information on the density and homogeneity of the system. In Figure 3.5 the green curve represents the substrate corresponding to the trigonal phase of crystalline Selenium. The extremely high local density which corresponds to 6 g/cm$^3$ at –7.5 Å is due to the artifact that I averaged over layers with a thickness of 5 Å and not thicker. If I would have averaged over thicker layers the density of the substrate at –7.5 Å would be the experimental value which is 4.8 g/cm$^3$. However, the 5 Å layer thickness is optimal for the amorphous case because it has no discrete transnational symmetry as a crystal. In the 1 eV and 0.1 eV case we can detect voids which are responsible for the low density. Note for example the density difference between 10 Å and 14 Å in the case of 1 eV bombarding energy. It is about 0.5 g/cm$^3$. The highest density sample made by 10 eV bombarding energy is the most homogeneous. The growth kinetics of the 0.1 eV and 1 eV cases differs in that the bombarding atoms with higher energy can penetrate more easily into the voids and fill them up. Therefore the density increases with bombarding energy, as this can be seen in Figure 3.14.

## 3.3.4 Growth versus rapid quenching

Chalcogenide glasses have been the subject of numerous experimental works in recent decades. Basically, there are two different ways to produce samples for experiments; liquid-quenching and evaporation. In the first case the initial phase of raw materials is liquid while in the latter case the starting compound is vaporized. Usually, the quenched materials are named glasses and the amorphous forms are prepared from gas phase onto substrates. The principal advantage of rapid quenching compared to evaporation is that the method can provide large volume of samples. There may be differences in the physical properties of samples produced by different ways because these states are non-equilibrium states [25]. My particular aim was to determine how the structural changes occur due to the different preparation methods. In order to obtain an answer for this question I performed molecular dynamics simulations. The atomic networks contain about 1000 Selenium atoms interacting via classical empirical three-body potential[6]. Non-crystalline Selenium receives particular attention because it is the model material of covalently bounded chalcogenide glasses.

### 3.3.4.1 Simulation details

The simulation of the vapor deposited sample has been described in detail in previous chapters. Here, I summarize only the most important points to compare the simulation details of the two different preparation techniques: growth and rapid quenching. Amorphous and glassy structures are usually grown by different vapor depositions on substrates. A crystalline lattice cell containing 324 Selenium atoms was employed to mimic the substrate. There were 108 fixed atoms at the bottom of the substrate. The remaining atoms could move with full dynamics. The simulation cell was open along the positive z-direction and periodic boundary conditions were applied in x and y-directions. Kinetic energy of the atoms in the substrate was rescaled at every MD step ($\Delta t = 1$ fs) in order to keep the substrate at a constant temperature. In this kind of simulation there is no ad hoc model for energy dissipation of incoming atoms, although the incoming atoms become part of the substrate after incorporation. In the deposition process the frequency of the atomic injection was 300 $fs^{-1}$. This flux is orders of magnitude larger than the deposition rate commonly applied in experiments but we compensate this disadvantage with a low substrate temperature and the substrate growth algorithm. After bombarding (no more incoming atoms) there were 30 ps periods for structure relaxations. Three different structures [SeStr] have been constructed at the temperature of 100 K. The average bombarding energies of SeStr0.1, SeStr1, and SeStr10 models were 0.1, 1 and 10 eV, respectively. However in the follow I were only consider the 1 eV case and only compare model SeStr1 with the rapid cooled model because the effect of the different bombarding energies on the structure has been already discussed in detail in previous chapter.

Rapid cooling of liquid phase is frequently applied to construct glassy structures. The system is usually cooled down to room temperature by a rate of $10^{11}$–$10^{16}$ K/s in computer simulations although this rate is some orders of magnitude smaller in the experimental techniques. In order to retrieve information on the rapid cooling (meltquench), I prepared a model (SeStrQ) in the following way. Temperature of a deposited film (SeStr1) was increased up to 900 K as an initial state (liquid phase), while the substrate temperature remained the same. After this melting, the trajectories of the Selenium atoms were followed by full dynamics for 100 ps. The substrate temperature kept at 100 K leads to the cooling of the film above the substrate. This technique can be considered as the computer simulation of real splat cooling, where small droplets of melt are brought into contact with the chill-block.

### 3.3.4.2 Temperature and densities during and after preparation

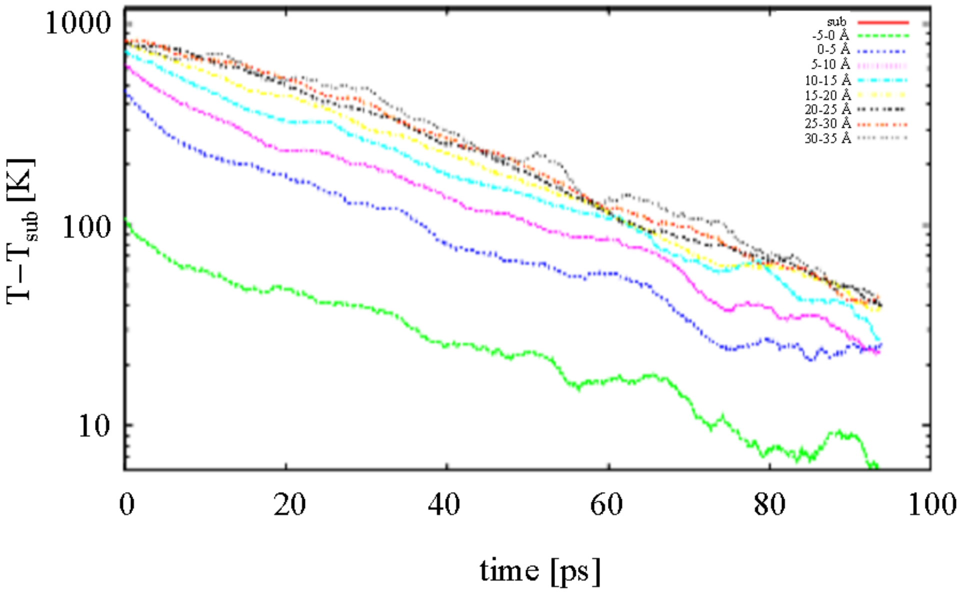

**Figure 3.15 Decrease of temperature in different layers during rapid cooling. The curves represent averages over 5 ps. This means for example that values at 0 represent an average over the raw values between 0 ps and 5 ps.**

Temperature relaxation of the amorphous system after heating the SeStr 1eV model. The heating procedure was the following. I have only heated up atoms which were not part of the 324 substrate atoms, in the following I will call these atoms bulk atoms. I increased the kinetic energy of bulk atoms to 2000 K in the first MD steps according to Maxwellian velocity distribution. After this I rescaled only the velocities of the 324 substrate atoms. The bulk atoms were able to move freely. Immediately, in the first couple of picoseconds the system thermalizes and the 2000 K kinetic energy decreases quickly to about 900 K. This is because the SeStr1 structure originally was relaxed at 100 K and its average potential energy was according to this. About half of the initially given kinetic energy is transferred into potential energy, this is the reason why the temperature drops so quickly in the first 5 ps. Note that in Figure 3.15. I have only plotted the temperature difference between the substrate and the layers after the initial 5 ps thermalization completed. The reason for this is that the exponential decrease of temperature in layers could be observed only after the initial thermalization phase.

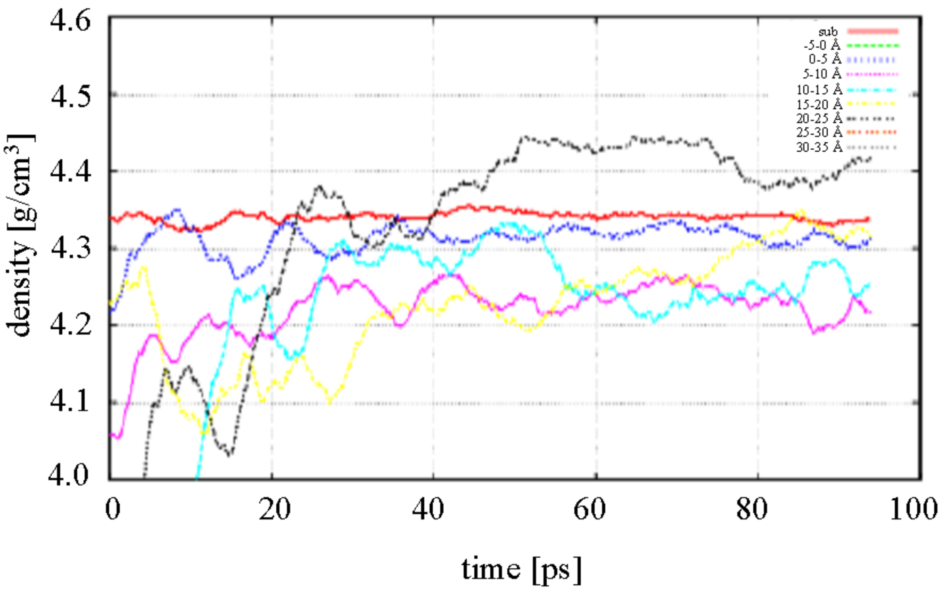

**Figure 3.16 Densities of different layers during rapid quenching. Moving average with 5 ps has been applied.**

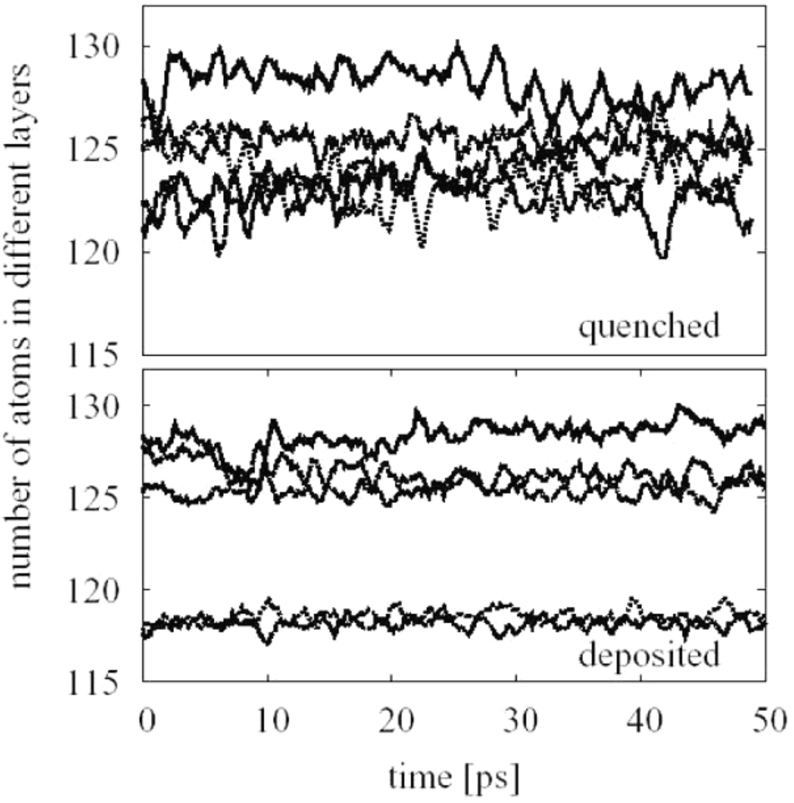

**Figure 3.17 Comparison of time developments of number of atoms in different layers after preparation for two different models. Low density layers disappeared from the SeStr1 model after the rapid cooling procedure.**

The exponential decay of the layers can be described as follows

$$T = T_0 \exp\left(-\frac{t}{\tau}\right).$$

where $T_0$ is the initial temperature of the layer after thermalization, $\tau$ is the characteristic time for temperature relaxation near the surface. Its value is 35 ps, as it can be estimated from Figure 3.15.

As the liquid droplet cools down after reaching the surface of a cold substrate its density begins to increase. This process can be seen in Figure 3.16. After the thermalization took place (5 ps) and the densities decreased from the amorphous value to the liquid value they begin to increase again as temperature drops. Large density fluctuations can be seen during the last phase of the cooling (at around 80 ps) where the layer 20-25 Å is only about 200 K hot, 100 K hotter than the substrate (100 K) as it can be seen in Figure 3.15. We can also note that the different layers have different densities, similarly to the case of deposited atoms. In Figure 3.17 the time developments of the number of atoms in different layers are depicted. Concerning the total density, the density of the rapid quenched model (SeStrQ) is 6% higher than that of the SeStr1 model.

In order to compare how much density fluctuation can be expected due to the system geometry and the relatively low number of atoms in the layers (about 100 atoms) I have performed a simulation with Selenium liquid at 3000 K. The density fluctuations of the different layers is depicted in Figure 3.18. It can be seen that after equilibration the fluctuation is between only 2-3%, therefore deviation more than 3% can be considered as significant inhomogeneity in the amorphous samples, as discussed above. It is interesting to note, how gradually the density fluctuations caused by non-equilibrium initial atomic positions decay at 3000 K in about 60 ps, and the system behaves stationary after this point. This reflects the fact that even at high temperatures a considerable amount of computing power is needed to reach equilibrium, this illustrates for example why it is nearly impossible to study crystallization by molecular dynamics simulations.

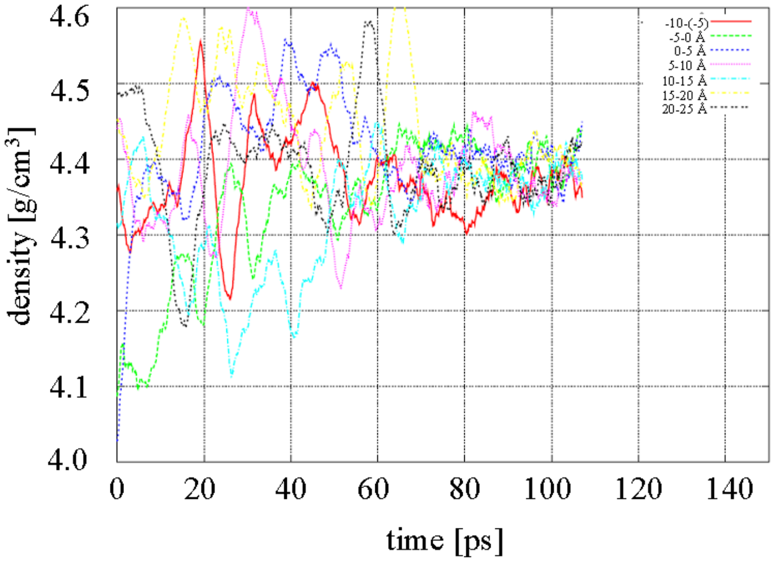

**Figure 3.18 Equalization of densities of different layers with random starting atomic positions at 3000 K temperature. Note that the maximal density fluctuation of the layers is only about 2-3%, therefore fluctuations in the amorphous samples larger than this are significant and they are not simply due to the fact that atoms are randomly distributed in the layers.**

### 3.3.5 Conclusion

I have developed a molecular dynamics computer code to simulate the preparation procedure of a-Se networks. I have grown three models by a vapor deposition technique and additionally prepared one model with simulated rapid cooling. This enabled me to make a direct comparison between the atom-by-atom deposition and melt-quenching preparation techniques. The most important difference I have found between the models prepared at various conditions, was in the local density. Rapid quenched models were more homogeneous than their deposited counterparts. Furthermore, I observed an increase in bulk density due to higher bombarding energies in the deposited models. Bond angles and bond lengths were compared with experimentally determined values obtained using the Cambridge Structural Database, the world's largest database of experimentally determined crystal structures. Bond lengths were larger in the simulated models compared to experimental values and bond angle distributions were in perfect agreement with diffraction data.

## *3.4 Growth of amorphous Selenium thin films: classical versus quantum mechanical molecular dynamics simulation*

### 3.4.1 Motivation

Recently, amorphous chalcogenide thin films have received particular attention due to their unique light-induced effects [26,27]. Samples for experiments can either be grown by vacuum deposition techniques or prepared with rapid quenching. I focus on vacuum deposition where the starting compound is evaporated and condensed to a substrate. This process can be followed by an atomic-scale molecular dynamics (MD) simulation where the forces acting on the particles are calculated from a model interatomic interaction which can be either a classical empirical or a quantum mechanical description. The quality of the model interaction profoundly determines the results obtained by molecular dynamics simulation.

In this chapter I compare three different types of interaction by growing amorphous Selenium (a-Se) thin films. Amorphous Selenium is considered as a model material for chalcogenide glasses. As far as I know no molecular dynamics investigation has been carried out on a-Se thin film growth yet. My particular questions are the following. What are the differences in physical properties of the films simulated using various interatomic potentials? When should we use the more CPU time-consuming quantum mechanical description instead of the classical empirical one?

### 3.4.2 Simulation details

The ATOMDEP simulation algorithm for atomic deposition has been already applied successfully for growing amorphous carbon [1], Silicon [2] and Selenium films [28], however the detailed simulation geometries and parameters are different from previous work, therefore I give a short overview on the most important aspects of the simulation technique applied.

An $\alpha$-crystalline Selenium lattice with chains directed perpendicular to the growth direction was chosen as the substrate model (Figure 3.19a). It contained 72 Selenium atoms of which 36 atoms were held fixed at the bottom part of the substrate. The dimensions of the substrate were 13.35 and 19.0 Å in the $x$ and $y$ directions where periodic boundary conditions were applied. The simulation cell was open along the $z$ axis, i.e., in the growth direction. For integrating the Newton equations in the MD simulation I used the velocity Verlet algorithm [15]. The time step was chosen to be 1 fs. The preparation conditions were identical in each case; only the interatomic interactions were different. The total kinetic energy of the atoms in the substrate was rescaled at every MD step in order to keep the substrate at a constant temperature ($T$ = 300 K). I used the growing substrate algorithm: as soon as atoms arrived at a substrate-atom closer than 3.5 Å they were treated also as a substrate-atom: their temperature was also controlled [18]. The incoming atoms were randomly positioned above the substrate and their initial velocity corresponded to an average kinetic energy of 1 eV with Maxwellian velocity distribution. Directions were determined by $\theta = 120° + p \times 60°$ and $\varphi = p \times 360°$, where $\theta$ and $\varphi$ are polar angles and

$p$ is a uniformly distributed random number between 0 and 1. In the deposition process the frequency of the atomic injection was 125 $\mathrm{fs}^{-1}$. The total bombardment period was 500 ps. The corresponding flux is orders of magnitude larger than the deposition rate commonly applied in experiments which usually corresponds to a couple of monolayers per second. I have compensated this deviation by the growing-substrate algorithm [18]. A 20 ps period followed the bombardment (no more incoming atoms) for structure relaxations.

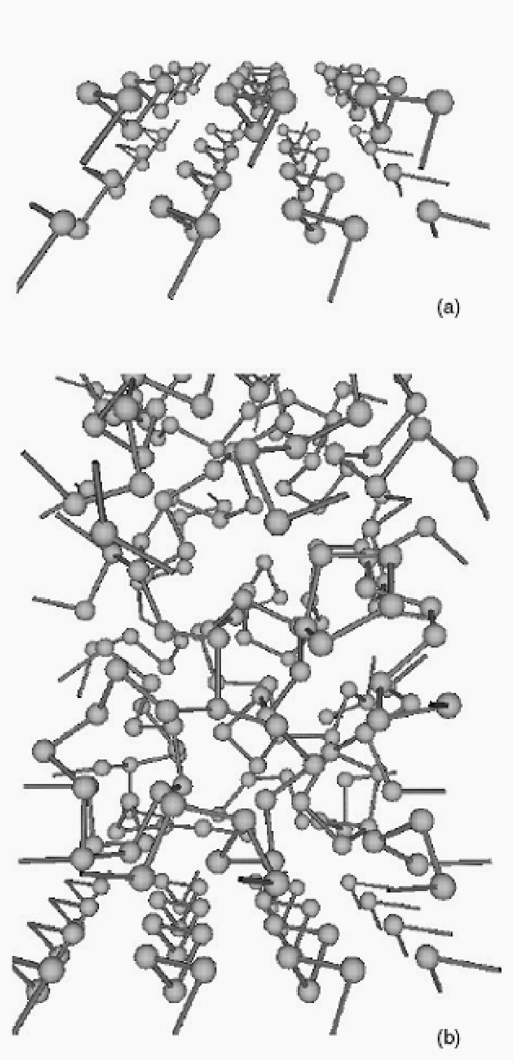

**Figure 3.19 Snapshots of the substrate (a) and of an amorphous Selenium film (b) after relaxation. The substrate consisted of six 12-member helical Selenium chains. The three bottom chains were fixed to mimic the underlying bulk material. Dangling bonds at the border are displayed for a better visualizations of the periodic boundary conditions.**

## 3.4.3 Applied potentials

*Classical empirical potential*

For classical empirical simulations I have chosen the three-body potential developed by Oligschleger *et al* [6]. It employs two-body and three-body terms to describe correctly the two-fold coordinated nature of Selenium structures. The potential was parameterized by fitting the binding energy of Se-clusters and crystalline phases to

DFT calculations and experimental values. It was used to investigate the structure, relaxation and thermal properties of amorphous Selenium [3, 4, 5].

*Tight-binding model*

Tight-binding models [10] for studying amorphous Selenium have been widely used in recent years [7, 8, 9]. The tight-binding (TB) method preserves the quantum mechanical description of bonding when compared to empirical methods but its drawback is the higher computational cost. However, when compairing it with the *ab-initio* techniques it is faster, but it has reduced transferability because of the approximations made. For my simulations I have chosen the model proposed by Molina *et al* [11] which has been tested in different phases and proved to give acceptable agreement with experiments. The total energy was computed by diagonalizing the hopping matrix [11].

*Tight-binding model with Hubbard correction*

In disordered phases of Selenium the TB model developed by Molina *et al* [11] produces large charge transfer and favors coordination defect formations. To correct this discrepancy the authors introduced a Hubbard term [12], which increases the potential energy of the system if positive or negative charge accumulates on atoms. The Hubbard term can be taken into account either by perturbation theory [12] or by self-consistent field method. I have chosen the latter, which requires iterative solving where one can use the solution obtained in the previous MD step as the starting point for the actual MD step. Usually, only a few iterative steps were needed to obtain the solution in our simulation.

### 3.4.4 Analysis of amorphous structures

#### 3.4.4.1 Densities, coordination defects

I denote the structural model prepared using classical empirical potential as CLASS. Structures obtained using tight-binding models are named as TB-NOHUB (without Hubbard term) and TB-HUB (with Hubbard term). To eliminate surface and substrate effects [1], I took into account only a 33.0 Å thick layer with 5 Å above the substrate and at least 5 Å below the atom which had the largest *z*-coordinate. A typical snapshot after relaxation can be seen in Figure 3.19b. The number of atoms, densities and percentages of coordination defects inside the subsystem are shown in Table 3.6. Densities are lower by 4%–5% than the experimental value [13], which can be attributed to the fact that preparational details affect the density: for example, my previous classical molecular-dynamics simulation study on a-Se thin film growth has shown that bombarding energy correlates with the final density of the amorphous films [28]. Two atoms are considered to be bonded if the distance between them is shorter than 2.8 Å. The most stable $\alpha$-crystalline phase of Selenium consists of helical chains parallel to each other, which means that every atom is two-fold coordinated. Other crystalline phases of Selenium are built up from eight-member rings [24]. In the amorphous phase Selenium chains can end or branch at coordination defects (one-fold or three-fold coordinated atoms). In liquid (close to the melting point) and glassy Selenium their concentrations are very low [12, 22], i.e., chains of a thousand atoms can exist [19]. I have found that model TB-HUB gives the lowest defect concentration: it provides the most realistic modeling in this respect. Simulation of the amorphization by rapid quenching using the TB-HUB interaction can produce samples having more than 99% two-fold coordinated atoms [29]. By compairing the TB-NOHUB and TB-HUB models it turns out that the Hubbard term is essential for achieving low coordination defect density: in the TB-NOHUB model nearly every second atom introduces a coordination defect. The dominant structural defect in model CLASS is the branching of Selenium chains. Accordingly, this model has the lowest one-fold coordination defect density: it is below 1%. Coordination defects change the corresponding average bond length, too. Higher coordination number causes longer bond length (Table 3.7). This correlation can be observed in all the models and its magnitude can even reach 10%.

| Model | $N_{bulk}$ | Z=1 | Z=2 | Z=3 | $\rho$ |
|---|---|---|---|---|---|
| CLASS | 272 | 0.8% | 88.3% | 10.9% | 4.21 |
| TB-NOHUB | 282 | 16.7% | 46.6% | 36.7% | 4.31 |
| TB-HUB | 274 | 1.9% | 92.0% | 6.1% | 4.27 |
| Experiment | | | 99.9% | | 4.47 |

**Table 3.6 Model, number of atoms in bulk ($N_{bulk}$), percentages of atoms with different coordination numbers ($Z$), and density $\rho$ (g/cm$^{-3}$). Experimental data were taken from Ref. 13, 21.**

| Model | Z | $d_{bond}$ (Å) | θ | γ | $N_{ICN}$ |
|---|---|---|---|---|---|
| CLASS | 1 | 2.33 | | | 9.9 |
| | 2 | 2.36 | 102.5° | 80.0° | 8.0 |
| | 3 | 2.43 | 101.0° | 83.8° | 5.8 |
| TB-NOHUB | 1 | 2.38 | | | 9.0 |
| | 2 | 2.41 | 99.5° | 95.4° | 7.0 |
| | 3 | 2.45 | 99.0° | 93.6° | 5.4 |
| TB-HUB | 1 | 2.36 | | | 10.1 |
| | 2 | 2.42 | 101.5° | 85.6° | 7.8 |
| | 3 | 2.48 | 100.9° | 95.6° | 5.4 |

**Table 3.7 Influence of coordination number ($Z$) on average bond length ($d_{bond}$), bond angle ($\theta_{bond}$), dihedral angle ($\gamma$) and number of interchain neighbours ($N_{ICN}$).**

### 3.4.4.2 Radial distribution functions

In Figure 3.20, the radial distribution functions (RDFs) are depicted. Curves are obtained as time averages during equilibrating the final structures at 300 K for 10 ps. The first peak describes the nearest-neighbor shell: model CLASS has the sharpest peak, whereas model TB-NOHUB has the broadest due to the overwhelming presence of coordination defects. In this model the peak position is also shifted to larger values compared to its counterparts because of the longer bond lengths associated with three-fold coordinated atoms. The second peaks correspond to second-neighbour distances. Model CLASS has a single peak at 3.6 Å; by contrast, in model

TB-NOHUB two shoulders can be seen at 3.25 and 3.9 Å, which become more pronounced in model TB-HUB.

For a better understanding of the curves I divided them into two components: corresponding either to interatomic distances between atoms in the same chain (intrachain– RDF) or in different chains (interchain–RDF). One can see that in model-CLASS the interchain and intrachain peaks almost coincide at 3.6 and 3.7 Å. The first peak is much broader and has also a greater total area under the curve than the second peak. The shoulders seen in the total RDF in model TB-NOHUB and model TB-HUB are the consequences of the different peak positions of the interchain and intrachain curves. Furthermore, in model TB-NOHUB and model TB-HUB the interchain RDF has a small shoulder, i.e., a pre-peak at 3.25 Å. The intrachain curve is broadened in model TB-NOHUB due to the broad first-neighbour peak. I characterized the structures also by measuring the number of interchain neighbors, which is the number of atoms being closer than 4.5 Å to a given atom but being in a different chain (see Figure 3.20, dotted line).

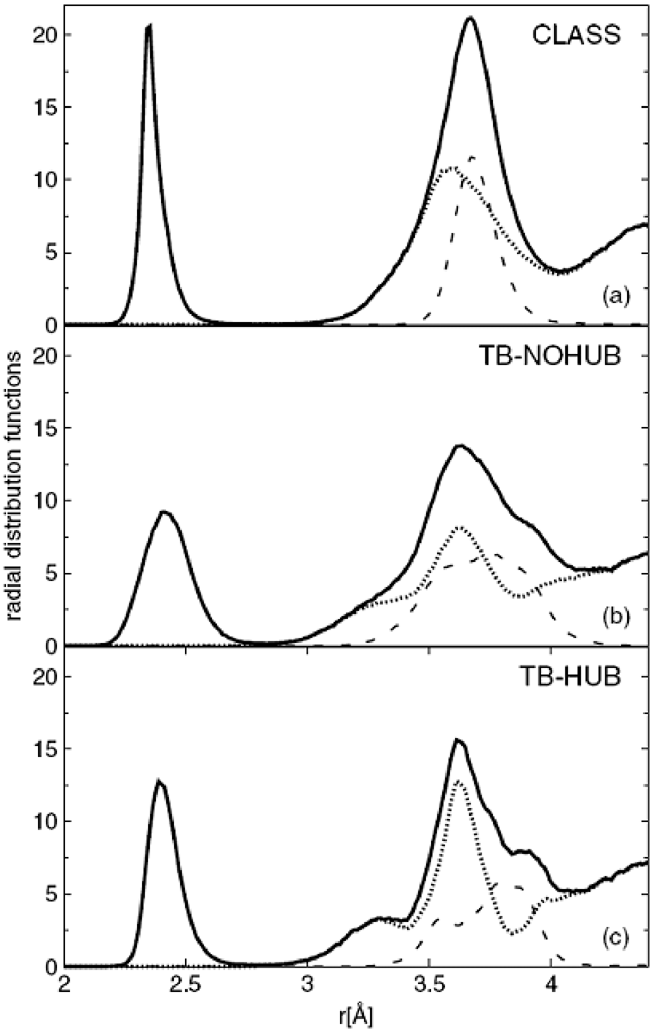

**Figure 3.20 Radial distribution functions of our amorphous Selenium models prepared by classicalempirical potential (a), tight-binding model without Hubbard term (b), and tight-binding model with Hubbard term (c). Solid lines represent the total radial distribution function, dotted and dashed lines correspond to the inter- and intrachain interatomic separations, respectively.**

I observed the decrease of the number of interchain neighbors with increasing coordination number (Figure 3.20). This is reasonable since the more neighbours an atom has the more intrachain second-nearest neighbors it has. That is why there will be less space left for interchain neighbors.

### 3.4.4.3 Bond angles

The bond angle distributions of the models differ significantly: the time-averaged distribution can be seen in Figure 3.21. Bond angles were not larger than 115° in either model; however, we have observed very rarely thermally fluctuating bond angles which had could temporarily have values from 80° up to 180° in every model. Model TB-NOHUB has the smallest bond angle values. Due to the high number of three-fold coordination defects, model TB-NOHUB also has the largest area under the curve, which gives the average number of bond angles per atom. Model CLASS provides the sharpest peak: here the full width at half maximum (FWHM) is only 8°; in comparison, in model TB-NOHUB it is 18°. Model TB-HUB has a bimodal intrachain radial distribution function (Figure 3.20) due to the corresponding bond angle distribution (Figure 3.21). A similar bimodal structure has also been reported by Shimizu *et al* [8]. Furthermore, bond angles depend on the coordination number of the central atom: in every model two-fold coordinated atoms have larger average bond angles than three-fold coordinated atoms but this difference is very small: it is about 1–2% (see table 2).

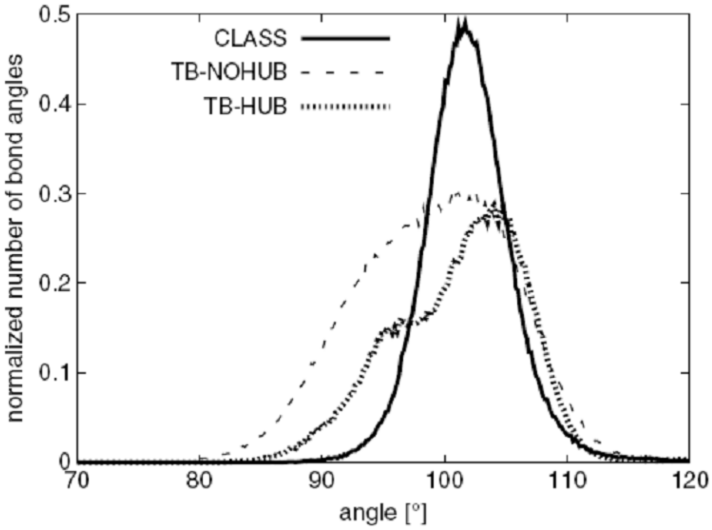

**Figure 3.21 Bond angle distributions of our amorphous models. Model TB-HUB provides a bimodal distribution (dotted line) whereas model CLASS has the sharpest peak (solid line) while model TB-NOHUB the broadest (dashed line).**

### 3.4.4.4 Correlation between bond angles and bond lengths

A correlation between bond angles and bond lengths of –Se–Se–Se– fragments can be observed in models CLASS and TB-NOHUB (Figure 3.22). However, a monotonic dependence cannot be seen in model TB-HUB. To compare these results to experiments I have additionally analysed the structure of 512 molecules containing –Se–Se–Se– fragments. This systematic analysis of structural data has been carried out using the Cambridge Structural Database (CSD) [23],which is the world's largest database of experimentally determined crystal structures containing the results of x-ray and neutron diffraction studies. The Cambridge Structural Database is designed as a critically evaluated numerical resource, containing three-dimensional atomic coordinates. The result of the search is shown in Figure 3.23. Each point represents a measured bond angle as a function of bond length. The majority of the points fall in the expected region, i.e., around 2.35 Å and 102°.

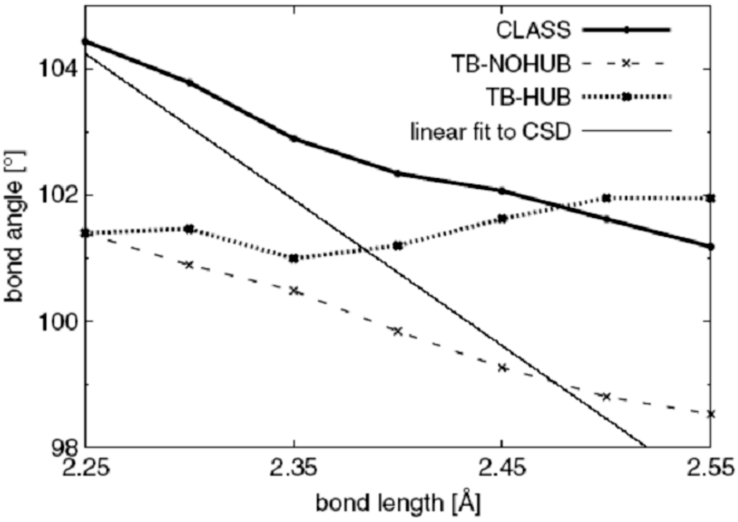

**Figure 3.22 Bond angles of –Se–Se–Se– fragments correlate with their bond lengths in models CLASS (solid line) and TB-NOHUB (dashed line). However, model TB-HUB (dotted line) shows a non-monotonic bond angle dependence on the bond length values. The thin solid line represents the best linear fit (with $\sigma = 4.2°$) to the corresponding bond angle and bond length values obtained from the Cambridge Structural Database (see Figure 3.23).**

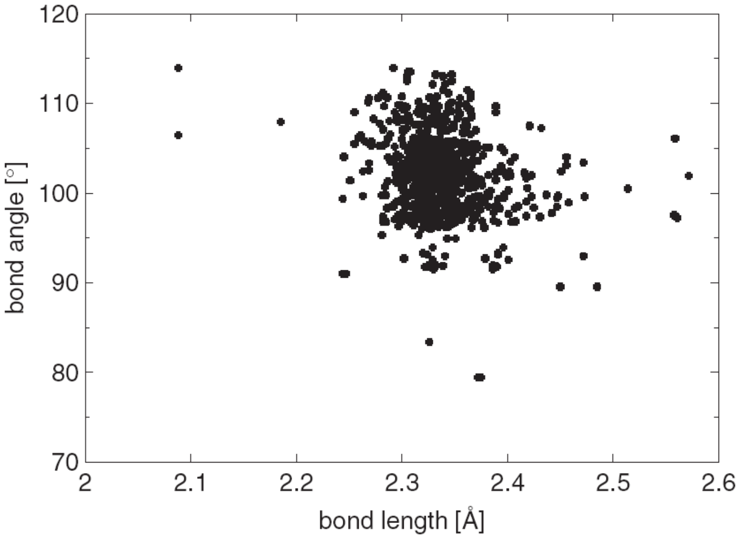

**Figure 3.23 Bond angles versus bond lengths function of 512 –Se–Se–Se– fragments in different molecules. Note that fragments having bond lengths larger than 2.38 Å have mainly bond angles smaller than 105° while larger bond angles correspond to smaller bond lengths.**

The minimum bond length is 2.09 Å, while the maximum is 2.58 Å. The bond angles lie inside the interval 79°–114°. Drawing a line of best fit (Figure 3.22, thin solid line), a correlation can be observed, i.e., an increase of bond angle corresponds to a decrease of bond length (Figure 3.22). A similar result has been obtained for the case of Silicon fragments [30]. This tendency can be also seen in models CLASS and TB-NOHUB, while a contrary behavior is present in model TB-HUB. This suggest that although model TB-HUB performs as the best in all other aspects, it fails to describe correctly the dependence of bond lengths on bond angles.

### 3.4.4.5 Dihedral angles

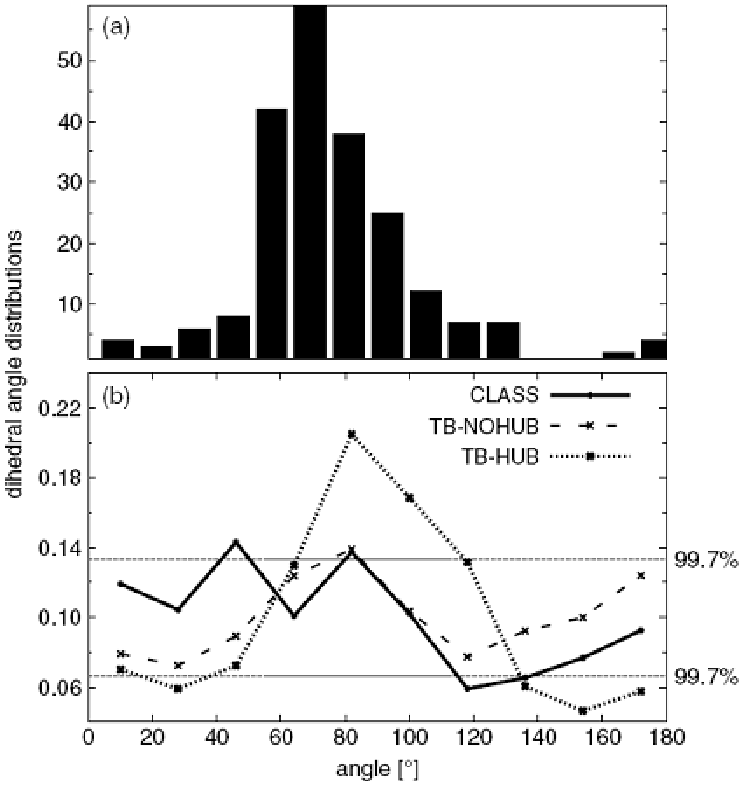

**Figure 3.24 Dihedral angle distributions of –Se–Se–Se–Se– fragments in the CSD (a) and of our models (b). Line types are defined as in Figure 3.22. Horizontal dashed lines represent the interval in which randomly distributed dihedral angles would lie with 99.7% probability. Only by points lying outside this interval can the corresponding dihedral angles be considered as significantly preferred or not preferred.**

In a comparison of dihedral angle distributions of –Se–Se–Se–Se– fragments (obtained from the Cambridge Structural Database, Figure 3.24a) and of my models is shown (Figure 3.24b). To improve the statistics I used 18° wide bins to create the dihedral angle distribution histogram of my models. Additionally, I modeled the random distribution of dihedral angles to measure the significance of the dihedral angle distributions obtained from the grown thin films. If the dihedral angles in my models were completely randomly distributed between 0° and 180° then the corresponding histogram values would lie between 0.133 and 0.066 (indicated by dashed horizontal lines in Figure 3.24b) with a probability higher than 99.7%. For modeling the completely randomly distributed dihedral angles, I assumed that the number of dihedral angles lying inside one bin has a binomial distribution. In this model calculation I set the total number of dihedral angles to 300. This number is close to the number of dihedral angles in all models. The lower this number is the wider the stripe in Figure 3.24 gets. I conclude that model CLASS prefers the absence of dihedral angles around 120° and prefers their presence at around 40° and 80°. Model TB-HUB does not prefer to have dihedral angles at around 30° and 150°. All models significantly prefer to have dihedral angles at around 80°. *Ab-initio* calculations for amorphous [31] and liquid Selenium near to melting point [32] have yielded dihedral angles similar to those in model TB-HUB. For comparison, the dihedral angles in $\alpha$-Selenium and $\alpha$-monoclinic Selenium crystalline phases are 100.7° and 103.1°, respectively [24]. Furthermore, the dihedral angle distribution of –Se–Se–Se–Se– fragments in the Cambridge Structural Database is very similar to the dihedral angle distribution of model TB-HUB, only the peak position is shifted with 15° towards smaller values. Therefore, I consider model TB-HUB as the most realistic description in this respect. I also analysed how coordination defects influence dihedral angles. Let us assume a chain segment of four Selenium atoms: A–B–C–D. The corresponding average dihedral angle is influenced by the coordination number of atom B (see Table 3.7). The most significant effect can be seen in model TB-HUB: the average dihedral angle increases by 10% with increasing coordination number.

### 3.4.5 Conclusion

I have grown amorphous Selenium thin films using three different types of Selenium interatomic interactions in my molecular dynamics simulations: one of them is based on a classical empirical three-body potential and the other two are of quantum mechanical origin. I analyzed the structural properties of the obtained amorphous networks: significant differences were found in the radial distribution functions, bond angles, dihedral angles and coordination defects. Furthermore, I have presented statistics based on a large number of diffraction measurements on molecules containing Selenium fragments. I observed an increase in bond length with decreasing bond angle. Only model TB-HUB did not reproduce this experimental result. Overall, model TB-HUB is the most realistic amorphous Selenium network. Model TB-NOHUB is unacceptable due to it is high number of coordination defects.

## 3.5 Two different tight-binding models. Description of structures obtained by them

### 3.5.1 Motivation

It has been concluded by K. Kohary in his doctoral dissertation [18] that the tight-binding model developed by Kwon *et al.* to describe Silicon performs poorly if applied to disordered phases. It predicts liquid like coordination defects, i.e. Silicon atoms with six neighbors in the condensed phase, which is not acceptable. Recently, a new version of the potential has been developed, where more parameters and larger cut-off for hopping integrals have been introduced by Lenosky *et al.* [19]. For the modeling of functional dependence of hopping integrals on interatomic distance a pioneering method has been used: instead of fitting exponential functions, cubic spline interpolation has been applied. The new model preserved the effectiveness of the old one and it performs much better in describing crystalline phases and small Silicon clusters [19, 33]. Although the Lenosky model has been used in many calculations so far, to my knowledge no work has been devoted to investigate how well the model performs when disordered phases have to be described. The aim of this section is to compare previous structural models of amorphous Silicon made by K. Kohary and S. Kugler [2] who used the tight-binding model developed by Kwon *et al.* [17] to structural models prepared by myself using the Lenosky tight-binding model [19]. For testing the two potentials I employed two approaches: static testing and dynamical testing. Static testing takes places at T=0 K using molecular mechanics, where the position of atoms are relaxed to find local potential minima, given the same initial atomic configurations, namely the famous Wooten [34] model with 216 atoms. Dynamical testing on the other hand compares the structures prepared by the exact same deposition process, however using different tight-binding models for the interatomic potentials. Comparisons of the two potentials on small atomic clusters has been recently published by Panda *et al.*, in this section I bring this comparison further, similarly as it has been done ten years ago by Hensel *et al.* [35]. He compared the classical Stillinger-Weber potential and a density functional based non-orthogonal tight-binding molecular simulation approach to investigate the growth of Silicon on a crystalline substrate. Their tight-binding approach has although a high accuracy, however it is more complicated to implement and slower than the Lenosky model. The simplicity of the Lenosky model gives scientist the possibility to describe Silicon easily with an excellent accuracy, therefore its test on amorphous structures is valuable information to researchers.

### 3.5.2 Simulation details

In Figure 3.25 I have depicted the dependence of the four hopping integrals on the interatomic distance. These curves define uniquely the electronic part of tight binding models. The repulsive part of the models agree qualitatively [33], however the terms which account for the covalent bonds differ significantly between the two models as it can be seen in Figure 3.25. Note how the cubic spline interpolation introduces greater flexibility in the Lenosky model, also the hopping to larger distances especially the positive $ss\sigma$ hopping which differs drastically in the Kwon model. This sign change of the $ss\sigma$ hopping is not plausible because one expects the overlap integrals to decay with the interatomic distance because they are matrix elements expanded in atomic basic set. This behavior may be a consequence of a compensation for the simplifications in the orthogonal tight binding-model. The cubic spline interpolation consist of cubic polynomials attached to each other [36], for the description of one curve in Figure 3.25 nine parameters are needed. The key innovation in the Lenosky model is in the fitting procedure, that makes it possible to fit such a complicated model in reliable way, the model was fitted to large number of density functional data, especially paying attention to atomic forces. In the Kwon potential every curve is described by three parameters and the fitting took place to energies instead of atomic forces. It is remarkable how the number of parameters were increased from twelve to thirty six and the model still could be fitted properly without running into non-physical local minima.

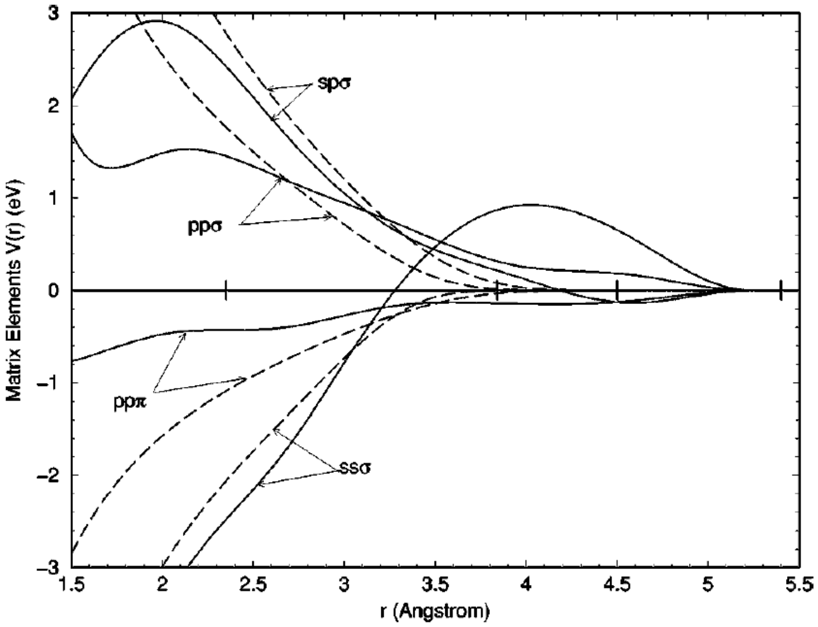

**Figure 3.25. Hopping integrals for the four different types of bonds for both tight-binding models (Lenosky – solid line, Kwon – dashed line), the figure is taken from Ref. 33. Note how the cubic spline interpolation enables much greater flexibility and non-monotonic behavior in the Lenosky model.**

I have implemented and tested the molecular dynamics computer code for the Lenosky tight-binding model and used it to grow 177 Silicon atoms on diamond substrate consisting of 120 atoms, with 24 atoms fixed at the bottom. In Figure 3.26 I have depicted the structure of both models, one made with the Lenosky tight-binding model (upper picture) and the other one made with the Kwon tight-binding model (lower picture). The results for the structure made using the Kwon tight-binding model has been taken from the doctoral dissertation of K. Kohary [18]. Different colors mean different coordination numbers in the amorphous layer, while red atoms denote fixed atoms at the bottom of the substrate and yellow atoms mean substrate atoms. Note how some of the substrate atoms and atoms from the amorphous structure changed roles after deposition: some substrate atoms incorporated into the amorphous layer while some deposited atoms incorporated into the crystalline substrate. All simulation parameters in the two runs were identical: bombarding energy of atoms were 1 eV. The bombarding atoms arrived with random directions, beside that impinging angles smaller than 60° were not allowed similarly to the case of Selenium (Section 3.3). The temperature of the substrate was set to 100 K, only the temperature of substrate atoms were rescaled. There was no need to apply the growing substrate algorithm applied during Selenium growth, because the grown Silicon layer is much thinner than the Selenium layer was and the surface of the amorphous film is not too far away from the crystalline substrate to conduct and dissipate heat. Also, the melting and boiling temperature of crystalline Silicon (1410 ºC , 2355 ºC) is much higher then that of Selenium (217 ºC , 684.9 ºC). The movies of the deposition process showed also a stable growth, without of the explosion of the amorphous structure as it was the case in Selenium when I not used the substrate growing algorithm. K. Kohary has found that using the substrate growing algorithm for larger systems [18] keeps the film solid during deposition and no relaxation needed. However, in the case of the Lenosky model, 5 ps relaxation was applied after the arrival of the last bombarding atom. This allowed the cooling down of the amorphous film, so that atomic vibrations become less important and the structure can be analyzed as a static structure. After the preparation of the Kwon model, K. Kohary applied a somewhat longer relaxation time, it was 20 ps.

### 3.5.3 Amorphous structures grown by different tight-binding models

#### 3.5.3.1 Three-dimensional snapshots

In Figure 3.26. the final three dimensional structures of the relaxed amorphous networks after growth is depicted. Top panel belongs to Lenosky-model and bottom panel to Kwon-model. All preparation parameters were identical, only the applied tight-binding models were different. Different colors mean different coordination numbers: orange is six, gray is five, blue is four, green is three, brown is two and red is one. Note, how much more five fold coordinated defects exist in the Kwon-model compared in the Lenosky-model, those kind of defects are called floating bonds. In the Kwon model even defects with six neighbors can be observed (orange colored atoms), such defects can only be found in liquid Silicon and therefore the Kwon-model provides a poor description in this respect. Note that the five fold coordination defects (gray atoms) always tend to be located next to either a three-fold coordinated defect ( green atoms) or a five fold coordinated defect. In this particular picture bonding was defined by the distance: if the distance between two atoms is smaller than 2.59 Å, then they were considered as bonded atoms.

#### 3.5.3.2 Densities and of coordination defects

| name of structural model | number of bulk atoms | density [g/cm$^3$] |
|---|---|---|
| Kwon | 134 | 2.4 |
| Lenosky | 113 | 2.3 |

**Table 3.8. Comparison of densities of different amorphous structures. In the second column the number of atoms is shown which were considered as free of surface and substrate effects, i.e. the total number of atoms in the system is more.**

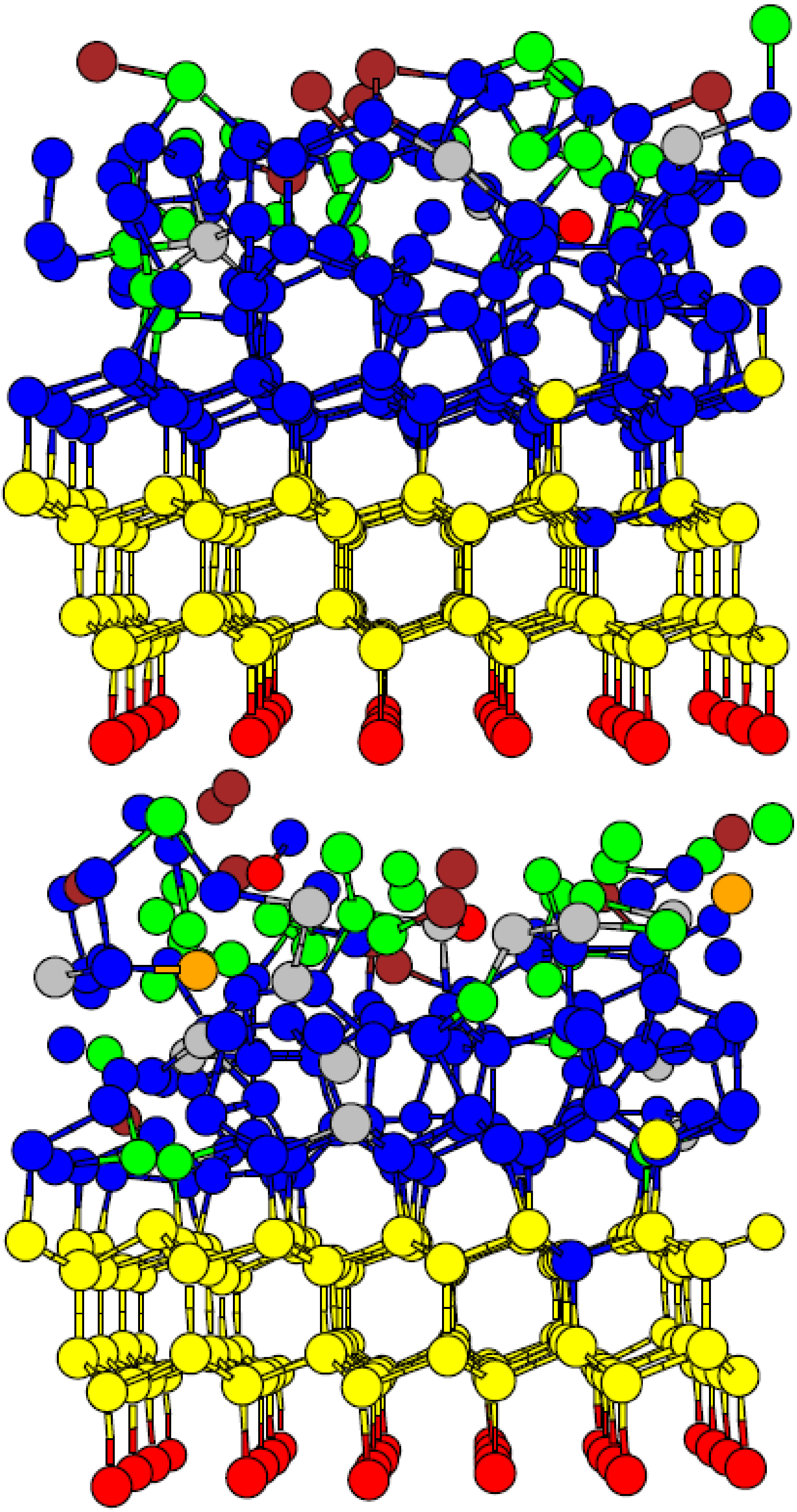

**Figure 3.26. Comparison of the amorphous structures grown by using different tight-binding models (top panel – Lenosky model, bottom panel – Kwon model). Preparation parameters are the same: bombarding energy is 1 eV, substrate temperature is 100 K**

In Table 3.8 densities of the two different amorphous structures are compared. To calculate densities and other structural properties of the amorphous samples I only considered atoms in Table 3.8. the amorphous film which were free of surface effects. Number of such atoms can be seen in This means the atoms above the substrate and 3 Å below the atom having the highest Z coordinate, Z axis points against growth direction.

The Lenosky model has smaller density than the Kwon model, however the bond lengths in different Silicon clusters would predict an opposite trend [33]. B. K. Panda *et al.* has calculated the ground state geometries of different Silicon clusters using both the Kwon as well as the Lenosky tight-binding method [33]. Most of the bond lengths in the Kwon geometries are larger than in the Lenosky geometries. This would predict that amorphous models made with the Kwon potential have smaller density than samples made using the Lenosky tight-binding model. The experimental crystalline density is 2.33 g/cm$^3$ which is close to the density of both structures. Due to small system size it is important to compare the densities predicted by the two models. By compairing the average bond lengths in the different models, we can conclude that the Lenosky potential predicts higher density, i.e. if we calculate the third power of the relative change in bond lengths, we obtain the percentual change in the volumes, which is 9%.

The density should be about 0.2 g/cm$^3$ larger in a model made by the Lenosky potential as compared to a model made by the Kwon potential, if only the average bond length changes (Table 3.9). However, as it can be seen in Table 3.8, the density in the Lenosky model is 0.1 g/cm$^3$ smaller than the density of the Kwon model, which means that the topology (number of coordination defects) of the amorphous network influences significantly the density of the structures.

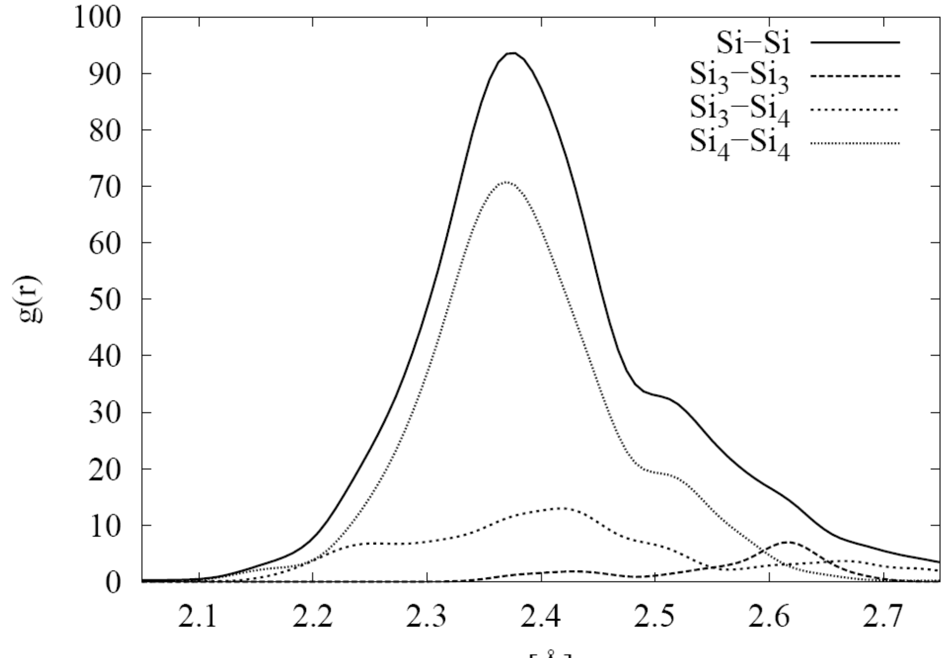

**Figure 3.27. Partial and total radial distribution functions of interatomic distances in the first neighbor shell in the Lenosky model.**

In Table 3.10 the relative number of coordination defects are compared in both models and in Table 3.9 their effect to change bond lengths is shown. The Lenosky mode performs better in describing coordination defects because it does not produce two-fold and six-fold coordinated atoms. Six fold-coordinated atoms only exist in liquid Silicon. Note how the coordination number changes the bond lengths (Table 3.9), bond lengths are in every case smaller in the Lenosky model. Coordination defects tend to increase bond lengths in both models compared to the bond between two four-fold coordinated atom ($Si_4$–$Si_4$).

By compairing average bond lengths (Kwon - 2.45 Å, Lenosky - 2.38 Å) with neutron diffraction measurements (2.34 Å, from Ref. 37) I conclude that the Lenosky potential performs better in reproducing the experimentally determined average bond length in amorphous Silicon.

| model | bond lengths [Å] | | | | | | |
|---|---|---|---|---|---|---|---|
| | Si–Si | $Si_3$–$Si_3$ | $Si_3$–$Si_4$ | $Si_3$–$Si_5$ | $Si_4$–$Si_4$ | $Si_4$–$Si_5$ | $Si_5$–$Si_5$ |
| Kwon | 2.45 | 2.53 | 2.47 | 2.51 | 2.42 | 2.49 | 2.49 |
| Lenosky | 2.38 | 2.47 | 2.37 | 2.42 | 2.38 | 2.40 | N/A |

**Table 3.9 Bond length changes due to different coordination numbers. Note that all values in the Lenosky model are smaller.**

| model | Z=2 | Z=3 | Z=4 | Z=5 | Z=6 | average Z |
|---|---|---|---|---|---|---|
| Kwon | 3.0 % | 12.7 % | 71.6 % | 10.4 % | 1.5 % | 3.9 |
| Lenosky | 0.0 % | 7.1 % | 89.4 % | 2.7 % | 0.0 % | 3.9 |

**Table 3.10. Comparison of relative number of coordination defects in both models. The Lenosky model has significantly less defects. Six-fold coordination defects can be found only in liquid Silicon, therefore the Kwon model performs poorly in this respect.**

### 3.5.3.3 Memory effect

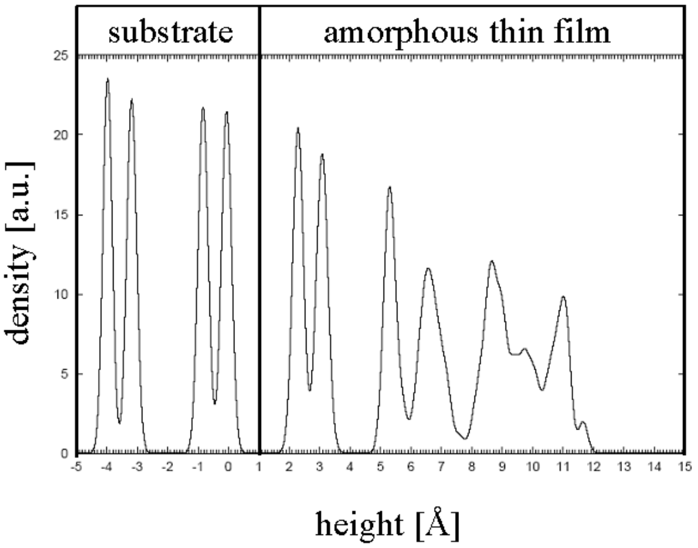

**Figure 3.28. Density profile for the Lenosky model. Note that a memory effect can be observed up to 7 Å. Real amorphous structure is above 7 Å. The first layer is perfectly crystalline as it can be seen also in Figure 3.26.**

In Figure 3.28 the density profile for the Lenosky model is depicted. Similarly to the case of carbon, in both models, a memory effect can be observed [1]. To illustrate this let us consider the density profile in the case of the Lenosky model (Figure 3.28). From –5 Å to 1 Å the substrate can be seen, and the four peaks between –5 Å and 1 Å correspond to the yellow atoms in Figure 3.26. The first layer of the grown film is perfectly crystalline which can be also seen in Figure 3.28 between 1 Å and 4 Å. Even the second layer has some crystalline characteristics from 4 Å and 7 Å, however the amorphous phase begins to emerge. Above 7 Å the memory effect can only vaguely observed.

### 3.5.3.4 Rings and average bond angles

Structure can be characterized through counting the number of rings in the samples, such information is also relevant to electronic structure as different ring sizes contribute at different energies to the electronic density of states. Detailed structural analysis shows that triangles tend to be in the vicinity of five-fold coordinated atoms. More detailed discussion on the presence of triangles and squares in amorphous Silicon is given by S. Kugler *et al.* in Ref. 38.

| ring size | 3 | 4 | 5 |
|---|---|---|---|
| number of rings in the Kwon model | 9 | 14 | 68 |
| number of rings in the Lenosky model | 3 | 7 | 50 |

**Table 3.11. Ring statistics. Note that the Kwon model provides higher number of triangles and squares than the Lenosky model. Note also that in the Kwon model there are three times more triangles than in the Lenosky model and also there are three times more five-fold coordinated defects in the Kwon model than in the Lenosky model (Table 3.10), this suggest a correlation between the number of five-fold coordination defects and the number of triangles.**

| model | Si-Si-Si | Si-Si$_3$-Si | Si-Si$_4$-Si | Si-Si$_5$-Si |
|---|---|---|---|---|
| Kwon | 105.6° | 98.6° | 107.0° | 102.9° |
| Lenosky | 109.0° | 113.7° | 109.0° | 104.0° |

**Table 3.12 Bond angle dependence on the coordination of the central atom. In crystalline Silicon all the bond angles are 109°. That is the consequence of tetrahedral bonding. The Lenosky model reproduces this value if the central atom is four-fold coordinated. There are opposite trends in bond angle change in the two models: in the Kwon model bond angles increase with increasing central atom coordination number, whereas in the Lenosky model just the opposite can be observed.**

Structures can be also characterized by average bond angles and their dependence on coordination numbers. In Table 3.12 I have summarized the dependence of bond angles on the coordination number on the central atom. We can see a drastic difference in the three fold coordinated atoms. In that case bond angles near to 120° correspond to a planar arrangement similar to that of graphite, on the other hand bond angles smaller than this predict structures which are not in-plane. We can conclude that the main difference between the two models in this respect is that the Kwon model favors three dimensional arrangements around a three fold coordinated atom, while the Lenosky model produces more likely planar arrangements.

### 3.5.4 Compatibility with the Wooten-Winer-Weaire model

The Wooten-Winer-Weaire model is one of the most accepted amorphous Silicon models even today, although the model is more than twenty years old [34]. In order to determine the quality of both tight binding models it is important to check if the models are compatible with the Wooten-Winer-Weaire model, which provides 100% four-fold coordinated structure. I have performed structural relaxation of the original Wooten-Winer-Weaire model at T=0 K temperature. The model containing 216 atoms were relaxed with both tight-binding models and the comparison of coordination defects after the relaxation can be seen in Table 3.13. The behavior of the two tight-binding models are completely different: the Lenosky tight-binding model causes the formation of three-fold coordinated defects and the Kwon model five and six-fold coordinated defects. This could be explained by the fact that the Kwon tight-binding model prefers longer bond lengths than the Lenosky model and therefore smaller densities. This in agreement with the plausible reasoning that by compressing amorphous Silicon in the computer, we can expect the appearance of five-fold coordinated atoms.

I conclude that none of the two tight-binding models are consistent with the original Wooten-Winer-Weaire model.

| coordination number | original Wooten-Winer-Weaire (WWW) model | WWW model after relaxing it with the Lenosky tight-binding model at T=0 K | WWW model after relaxing it with the Kwon tight-binding model at T=0 K |
|---|---|---|---|
| 1 | 0 | 0 | 0 |
| 2 | 0 | 0 | 0 |
| 3 | 0 | 4 | 0 |
| 4 | 216 | 212 | 213 |
| 5 | 0 | 0 | 2 |
| 6 | 0 | 0 | 1 |
| 7 | 0 | 0 | 0 |

**Table 3.13. Number of atoms having different coordination numbers in three structural models of amorphous Silicon. The behavior of the two tight-binding models are completely different: the Lenosky tight-binding model causes the formation of three-fold coordinated defects and the Kwon model five and six-fold coordinated defects.**

### 3.5.5 Conclusion

I have implemented in the ATOMDEP program package a recently proposed tight-binding model for Silicon, which is expected to perform much better than previous versions. My motivation was to produce good quality structural models of amorphous Silicon and also that – to my knowledge – the potential has not been tested so far for disordered structures. I have prepared an amorphous Silicon sample using the same procedure and physical parameters that have been used by K. Kohary who has applied a different tight-binding description. My aim was to compare the two structural models and decide which tight-binding model is more appropriate to provide good amorphous Silicon structures. I have compared densities, bond lengths, bond angles, number of coordination defects, number of triangles and squares. The most decisive difference can be seen in the description of coordination defects. The Kwon model produces six-fold and two-fold coordinated defects while the Lenosky model not.

I have also examined the compatibility of both tight-binding models with the Wooten-Winer-Weaire amorphous Silicon structural model which has 100 % four-fold coordinated atoms. I have relaxed the Wooten-Winer-Weaire model containing 216 atoms at T=0 K with both tight-binding models and calculated the number of coordination defects in the model. The two tight-binding models produced opposite results: the Lenosky model introduced three-fold coordinated defects, while the Kwon model five and six-fold coordinated defects.

Overall, I conclude that the Lenosky model provides better description for amorphous Silicon, the most important reason for this is that the Lenosky model does not produce six-fold coordinated defects in the amorphous structure. Such defects should be present only in liquid phase.

## 3.6 Bibliography

[1] K. Kohary and S. Kugler, Phys. Rev. B **63** 193404 (2001)
[2] K. Kohary and S. Kugler, Mol. Simul. **30** 17 (2004)
[3] C. Oligschleger and J. C. Schon, Phys. Rev. B **59** 4125 (1999)
[4] D. Caprion and H. R. Schober, Phys. Rev. B **62** 3709 (2000)
[5] D. Caprion, J. Matsui and H. R. Schober, Phys. Rev. Lett. **85** 4293 (2000)
[6] C. Oligschleger, R. O. Jones, S. M. Reimann and H. R. Schober, Phys. Rev. B **32** 1340 (1996)
[7] C. Bichara, A. Pellegatti and J. P. Gaspard, Phys. Rev. B **49** 6581 (1994)
[8] F. Shimizu, H. Kaburaki, T. Oda and Y. Hiwatari, J. Non-Cryst. Solids **250** 433 (1999)
[9] T. Koslowski, M. Koblischke and A. Blumen, Phys. Rev. B **66** 064205 (2002)
[10] C. M. Goringe, D. R. Bowler and E. Hernandez Rep. Prog. Phys. **60** 1447 (1997)
[11] D. Molina, E. Lomba and G. Kahl, Phys. Rev. B **60** 6372 (1999)
[12] E. Lomba, D. Molina and M. Alvarez, Phys. Rev. B **61** 9314 (2000)
[13] P. Jovari and L. Pusztai, Phys. Rev. B **64** 014205 (2001)
[14] S. Kugler, L. Pusztai, L. Rosta, P. Chieux, R. Bellissent, Phys. Rev. B **48** (1993) 7685
[15] M. P. Allen and D. J. Tildesley *Computer Simulation of Liquids* Oxford (1990)
[16] J. C. Slater and G. F. Koster, Phys. Rev. **94** 1498 (1954)
[17] I. Kwon, R. Biswas, C Z Wang, K M Ho, and C M Soukoulis Phys. Rev. B **49**, 7242 (1994)
[18] K. Kohary, Doctoral dissertation, Marburg-Budapest (2001)
[19] T. J. Lenosky, J. D. Kress, I. Kwon, and A. F. Voter, B. Edwards, D. F. Richards, S. Yang, and J. B. Adams, Phys. Rev. B **55**, 1528 (1997)
[20] S. R. Elliott, *Physics of Amorphous Materials* (Longman Scientific & Technical, John Wiley & Sons, Second Edition, 1990)
[21] P. Jovari, R. G. Delaplane and L. Pusztai Phys. Rev. B **61** 172201 (2003)
[22] G. Kresse, F. Kirchhoff, and M. J. Gillan, Phys. Rev. B **59**, 3501 (1999)
[23] F. H. Allen, O. Kennard, R. Taylor, Accts chem. Res. **16** 146 (1983)
[24] J. Donohue, *The Structures of The Elements* (John Wiley & Sons, 1974)
[25] K. Morigaki, *Physics of Amorphous Semiconductors* (World Scientific Publishing Co., 1999)
[26] T. Keiji Phys. Rev. B **57** 5163 (1998)
[27] J. Singh and K. Shimakawa *Advances in Amorphous Semiconductors* (London: Taylor and Francis, 2003)
[28] J. Hegedus, K. Kohary and S. Kugler, J. Non-Cryst. Solids **338** 283 (2004)
[29] J. Hegedus, K. Kohary and S. Kugler, J. Optoelectron. Adv. Mater. **7** 59 (2005)
[30] S. Kugler and Z. Varallyay, Phil. Mag. Lett. **81** 569 (2001)
[31] D. Hohl and R. O. Jones, Phys. Rev. B **43** 3856 (1991)
[32] F. Kirchhoff, G. Kresse and M. J. Gillan Phys. Rev. B **57** 10482 (1998)
[33] B. K. Panda S. Mukherjee and S. N. Behera, Phys. Rev. B **63**, 045404 (2001)
[34] F. Wooten, K. Winer and D. Weaire, Phys Rev. Lett. **54**, 1392 (1984)
[35] H. Hensel, P. Klein, H. M. Urbassek, and T. Frauenheim Phys. Rev. B **53**, 16497 (1996)

[36] W. H. Press, S. A. Teukolsky, W. T. Vetterling, and B. P. Flannery, *Numerical Recipes in C: The Art of Scientific Computing*, (2nd ed. Cambridge University Press, Cambridge, 1992)
[37] S. Kugler, G. Molnar, G. Peto, E. Zsoldos, L. Rosta, A. Menelle and R. Bellissent, Phys. Rev. B **40**, 8030 (1989)
[38] S. Kugler, K. Kohary, K. Kadas, L. Pusztai, Solid State Communications **127** 305 (2003)

# 4 Light-induced volume changes in chalcogenide glasses

## 4.1 Introduction

Chalcogenide glasses exhibit various changes in structural and electronic properties during bandgap illumination, like photo-induced volume change, photodarkening, and photo-induced change in the phase state (photo-crystallization and photo-amorphization). A size effect can be observed: photodarkening cannot be induced in $As_2S_3$ films which are thinner than 50 nm [1]. These phenomena do not occur in the crystalline chalcogenides nor in any other amorphous semiconductors. The microscopic structural changes are facilitated by two factors common to chalcogenide glasses: the low average coordination number and the structural freedom of the non-crystalline state. During the illumination some of the films can expand (a-$As_2S_3$, a-$As_2Se_3$, etc.), and some shrink (a-$GeS_2$, a-$GeSe_2$, etc.) [2]. Several investigations have been carried out in order to provide an explanation of these phenomena [3, 4, 5, 6, 7, 8]. It has been established that there is a configurational rearrangement with changes in atomic coordination in the vicinity of the excitation [5, 6, 7]. In a simplistic model such changes in the local bonding environment were explained by the formation of VAP's [5]. In amorphous Selenium, the model material of chalcogenide glasses, the formation of new inter-chain bonds has also been suggested [6]. However, an atomistic study of amorphous Selenium has revealed that the structural rearrangements are less local than used in such simple models and has given evidence that further possible bond formations and bond breakings are responsible for photo-induced effects [7]. Computer simulations of photo-induced phenomena become more and more important beside theoretical investigations, in the last couple of years excellent studies have been published on this topic [9, 10, 11, 12]. I proposed a simple, unified description of the photo-induced volume changes in chalcogenides based on tight-binding (TB) molecular dynamics (MD) simulations of amorphous Selenium [8]. I have found that the microscopic rearrangements in the structure (like bond breaking and bond formation) are responsible for the macroscopic volume change under illumination. The first *in situ* surface height measurement [13] on amorphous Selenium was carried out recently and supports my proposed mechanism. Recently, two excellent books appeared on these topic [14, 15]

The layout of this chapter is as follows: Section 4.2 gives an overview on our MD computer code we developed. The details of high quality, void free sample preparation using my code can be found in the Section 4.3. The two subsequent sections contain my microscopic and macroscopic descriptions of photoinduced volume changes.

## 4.2 Simulation method

In my previous work, I have further developed the molecular dynamics (MD) computer code called ATOMDEP to simulate the preparation procedures of real amorphous Selenium and Silicon structures (growth by atom-by-atom deposition on a substrate and rapid quenching) [16, 17]. Standard velocity Verlet algorithm was applied in my MD simulations in order to follow the atomic scale motions. To control the temperature I applied the velocity-rescaling method. I chose $\Delta t = 1$ fs or 2 fs for the time step, depending on the temperature. In my works the growth of amorphous Selenium and Silicon (see Chapter 3) films were simulated by this MD method. This computer code is convenient to investigate photo-induced volume changes as well if the built-in atomic interaction can handle the photo-excitation.

For calculating the inter-atomic forces in a-Se I used tight-binding (TB) [18, 19] and self-consistent tight-binding (SCF-TB) [18, 20] models. The TB parameterization [19] has been introduced for disordered Selenium following the techniques developed by Goodwin et al [21]. It was thoroughly tested by MD calculations in liquid and amorphous phases and the results were compared to experiments and to *ab initio* calculations. The agreement with experiments and *ab-initio* calculations are rather good apart from the fact that the number of coordination defects in the solid and liquid phases are higher than the experimentally measured values. The authors have improved their TB Hamiltonian by including the Hubbard correction [22]. This implies that either the algorithm has to be made self-consistent or perturbation theory must be applied. My choice is the first alternative. For a good accuracy only a few SCF and MD steps were needed because of the knowledge of wave functions from previous molecular dynamic steps. Convergence criteria were considered to be satisfied if the deviation of atomic charges between the actual and the previous iterations was less than 0.01 electron/atom. First, I constructed the tight-binding Hamiltonian, and then diagonalized it. After obtaining the solution, I added the new Hubbard term which is calculated using the eigenvectors. So I obtained the new Hamiltonian matrix. The procedure was repeated until the necessary convergence has been reached. The Hamiltonian matrix changed only slightly in one molecular dynamics step, due to the small atomic movements. Therefore, I used the eigenvectors from the previous molecular dynamics step as the starting point in the self-consistency cycle, this speeds up the convergence. However, convergence problems can occur if occupied and not occupied atomic orbitals are near to each other in energy. Near means that the correction due to Hubbard term can swap two orbitals in energy. The solution oscillates in such a case and does not converge. To handle this issue I introduced a damping in the SCF cycles by linearly combining the new solution with the previous one. This method slows down the convergence speed, but eliminates the oscillations as well. Such scenario typically happens if the LUMO and HOMO approaches each other nearer then 0.1 eV.

Crystalline forms of Selenium consist of chains and eight-membered rings. It is very likely that these local arrangements can be found in non-crystalline forms of Selenium as well. Therefore, first I have performed two simulations to see how the building units of amorphous Selenium react to photo-excitation [23]. Such runs are excellent to test the code before using it to simulate the photo-excitation in larger systems. Corresponding to the two simulations, there were two different initial configurations: an eight-member ring and an eighteen-member helical Selenium chain. In the initial configuration of the eight-member ring in my simulation had bond lengths of 2.38 Å and bond angles of $102^o$. Dihedral angles were equal to $100^o$.For the eighteen-member Selenium chain (with one-dimensional periodic boundary conditions) these values were: 2.36 Å, $100^o$, and $98^o$, respectively. In this structures every Selenium atom has two first-neighbors, i.e. there are no coordination defects.

Before illumination (photo excitation) the individual ring and the chain were relaxed for 4 ps at T=500 K. During this period the structures are stable.

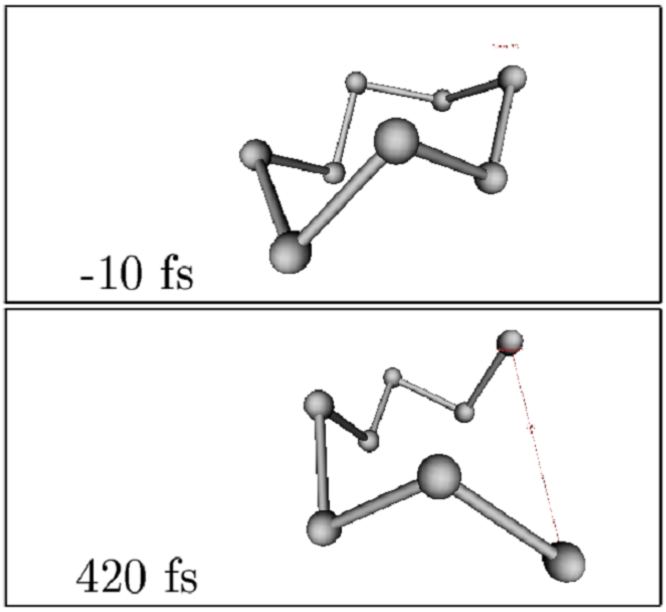

**Figure 4.1. Two snapshots of bond-breaking process caused by photo-excitation in the $Se_8$ ring. Top panel displays the ring structure before excitation. An electron from the HOMO is excited to the LUMO at $t = 0$ fs. Bottom panel shows the configuration after 420 fs.**

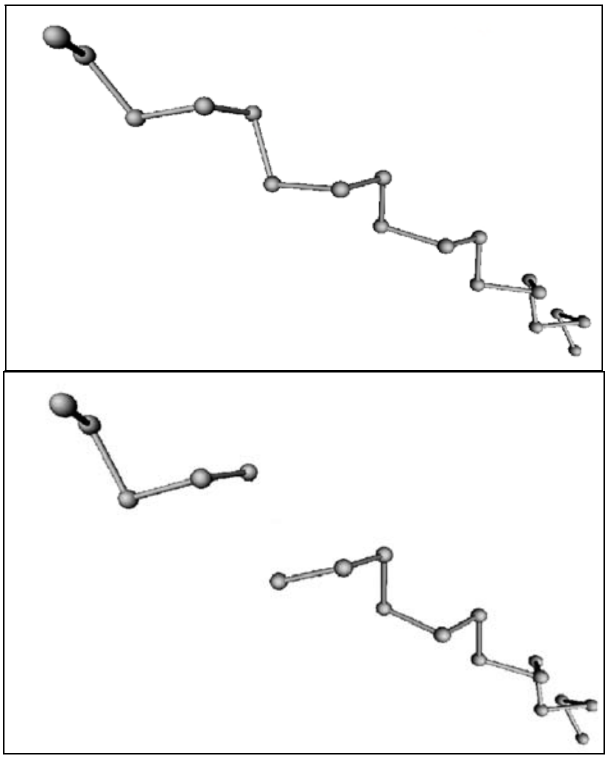

**Figure 4.2. Top panel: a snapshot of an 18 atom linear chain at room temperature. Bottom panel: the same linear chain after excitation.**

When a photon was absorbed an electron from the highest occupied molecular orbital (HOMO) to the lowest unoccupied molecular orbital (LUMO) was transferred. This is a simple model of photo-excitation when an electron is shifted from the valence band to the conduction band (electron-hole pair creation). After excitation one bond length in the ring started to increase and bond-breaking occurred (see Figure 4.1). A similar result was published [24] by a Japanese group for $S_8$. They performed MD simulation within the framework of density functional theory in the local density approximation. In our second MD simulation we investigated the linear chain structure. The same procedure was performed to model the excitation. Very similar result was obtained; a bond inside the chain was broken immediately after a HOMO electron was excited. Two snapshots of this process can be seen in Figure 4.2.

## 4.3 Sample preparation

To mimic the thin film structures, I fabricated glassy networks, for which I applied periodic boundary conditions (PBC) in two dimensions [*x*, *y*]. The samples were open in the *z* direction. When we illuminated the cell, it could expand or shrink into the open direction. The volume changes in the sample can be derived by measuring the distance between atoms at the two open ends. The initial simulation cell geometry was a rectangular box of size 12.78x12.96x29.69 (*xyz* in Å). The 162-atom sample had an initial density of 4.33 g/cm$^3$.

I prepared our samples from liquid phase by rapid quenching. My 'cook and quench' sample preparation procedure was as follows: first I set the temperature of the system to 5000 K for the first 300 MD steps. During the following 2200 MD steps, I decreased linearly the temperature from 700 K to 250 K, driving the sample through the glass transition and reaching the condensed phase. Then I set the final temperature to 20 K and relaxed the sample for 500 (1 ps) MD steps. The closed box was opened in the z-direction at the 3000th MD step. I thus obtained two surfaces with increased number of one-fold coordinated atoms. This final topology corresponded to a thin-film structure. One problem remained: the localized vibration modes at the surface were excited by the opening procedure. This caused an inhomogeneity in the temperature distribution: the sample had higher temperatures at the ends. Therefore, I homogenously redistributed the atomic kinetic energies according to the Maxwell-Boltzmann distribution, to speed up the thermalization process. I did this three times at the 4000th, 6000th, and 7000th MD steps. The Hubbard parameter, U was also changed during quenching. By increasing U, one can expect a greater tendency to form a nearly fully two-fold coordinated structure, which is claimed to be the situation for Selenium. Therefore, I set the Hubbard parameter at 5 eV during the quenching in the first 4000 MD steps. After the opening procedure was completed, during the relaxation phase at the 4000th MD step I restored U from 5 eV to 0.875 eV, which is the optimized value according to Lomba *et al.* [18]. The system was relaxed for at total of 40000 MD steps (80 ps) at 20 K.

The most important steps of the preparation procedure can be seen in Figure 4.3, Figure 4.4, Figure 4.5 and Figure 4.6. The initial structure was a bulk glassy Selenium network. As in the first phase (0-0.6 ps) the temperature was set at 5000 K in the first MD step, the potential energy abruptly increased from -540 eV to -480 eV (Fig. 3). This means that the initial bonding topology was completely destroyed since at high temperatures all the bonds break immediately. Here, two atoms were considered bonded when the bond length between them was less than 2.7 Å. The relative number of one fold coordinated atoms was about 40% and that of the three fold coordinated atoms was 10% during the first 0.6 picoseconds. At 0.6 picoseconds, when the temperature was set to be about 700 K, this situation changed drastically, the percentage of one-fold and threefold coordinated atoms decreased to 20-25% and 1-2%, respectively. At this point the potential energy decreased by 60 eV within less than 0.1 ps. In the second phase (0.6-5 ps), as I reduced the temperature further down from 700 K to 250 K the number of one-fold coordinated atoms decreased from 20% to 5% but the number of threefold coordinated atoms did not change (See Figure 4.4).

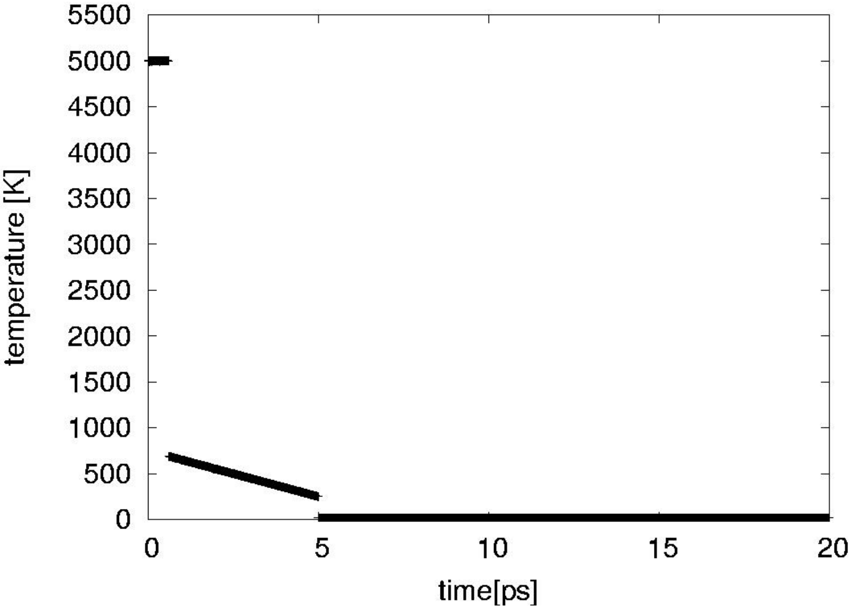

**Figure 4.3. Temperature as a function of time during the sample preparation.**

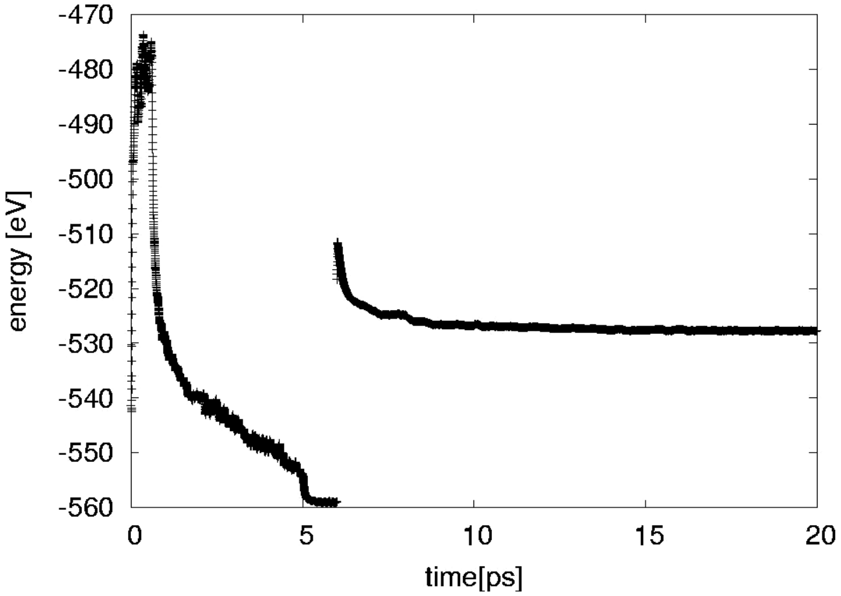

**Figure 4.4 A typical curve of the potential energy of the sample versus time during preparation**

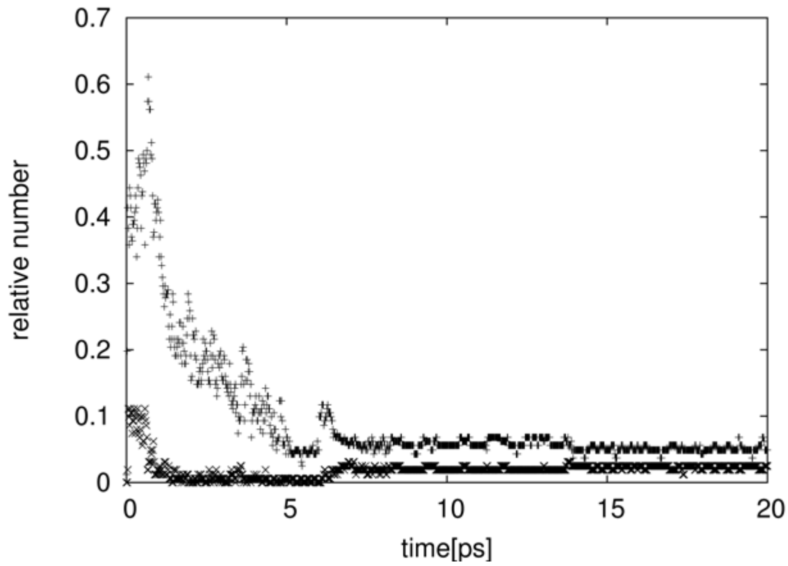

**Figure 4.5. Time development of the relative numbers of 3-fold (x) and 1-fold (+) coordinated atoms.**

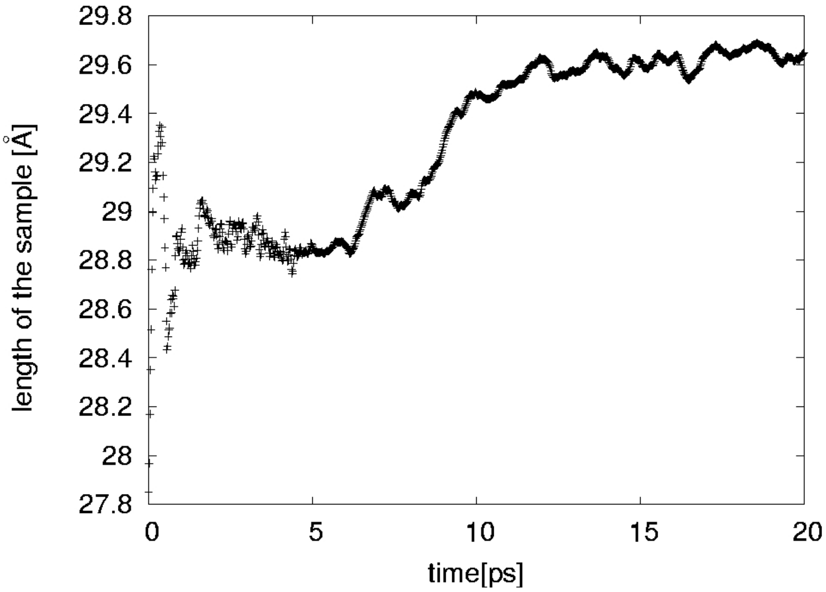

**Figure 4.6. Length of the sample during preparation.**

The cooling rate during this phase was about $10^{14}$ K/s. At 5 ps, another sudden decrease by 5 eV in the potential energy (Figure 4.4) was observed when the temperature was reduced from 250 K to 20 K. After this the system was equilibrated for another 1 ps and then the network was opened by releasing the PBC in the z-direction. Examining the potential energy (Fig. 3), an immediate increase from -560 eV to -510 eV can be seen. This corresponds to breaking approximately 10-20 bonds at the surface. Subsequently, a quick recovery occurred, involving about a 5-10 eV decrease in the potential energy in 0.5 picoseconds and then another 5-10 eV decrease on a longer time scale (10-100 picoseconds). The first corresponds to forming new bonds, as one sees in the change of coordination numbers (Figure 4.5), while the second corresponds to a large scale structural change, i.e. volume expansion (Figure 4.6.).

During the last five picoseconds the sample became stable and the volume no longer changed significantly. If I changed the initial velocities of the atoms only during the first MD step I fabricated topologically different glassy networks under similar physical conditions. For a 162 atom system, one SCF step on a 1200 MHz computer took about 2-3 seconds. The visualization of the structures and of the time development of the system was carried out by self-written Java software, JGLMOL [25].

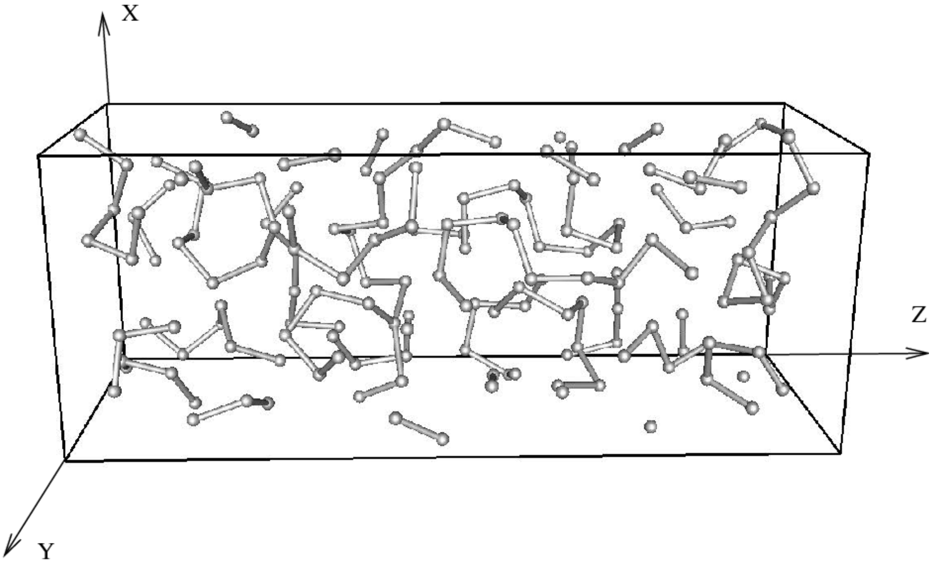

**Figure 4.7. Snapshot of a final glassy Selenium network. The sample can expand in z direction, since at the ends I do not apply periodic boundary conditions.**

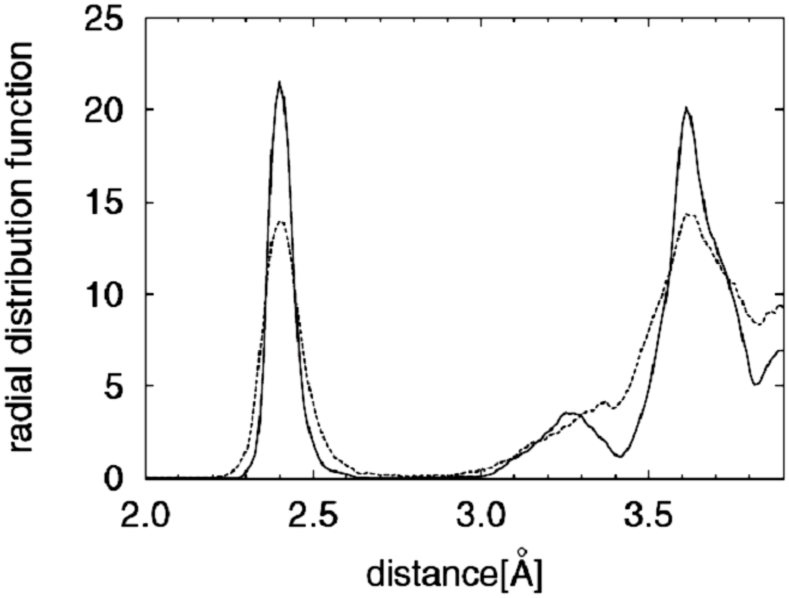

**Figure 4.8. Radial distribution function of amorphous Selenium network in function of atomic distances. The model was prepared by MD simulation at 20 K. Dashed line stands for radial distribution function at 300 K. Peaks at 3.3 Å and at 3.6 Å which are separate at 20 K merge at 300 K.**

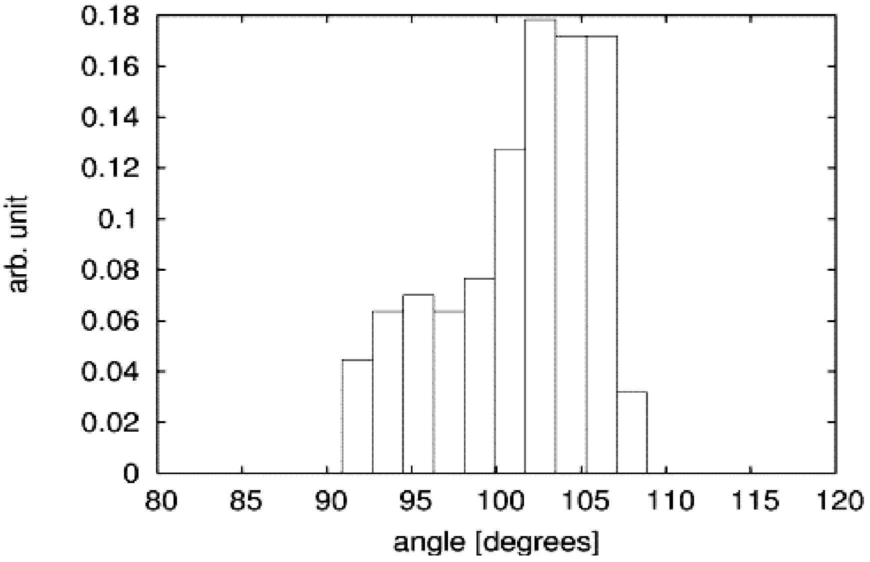

**Figure 4.9. Bond angle distribution function at 20 K.**

Samples prepared at 20 K had densities from 3.95 to 4.19 g/cm$^3$. The number of coordination defects ranged from 3 to 12%. Most of these defects were located on the surfaces. The structure mainly consisted of branching chains, but some rings could also be found. The samples were accepted if the volume fluctuation was less than 0.5 % in 60 picoseconds. I prepared altogether 30 samples, and 17 were considered to be stable and useful for further studies. One of them is displayed in Figure 4.7. A radial distribution function and bond angle distribution of a representative sample can be seen in Figure 4.8 and in Figure 4.9.

## *4.4 Light induced phenomena*

In the amorphous Selenium immediately after the absorption of a photon, a pair of electron and hole became separated in space [8]. Therefore, they can be treated independently i.e. we can investigate the roles of excited electrons and holes separately. I ran two sets of computer simulations: first, to model the excited electron creation I put an extra electron into the LUMO (Lowest Unoccupied Molecular Orbital), and second, I annihilated an electron in Highest Occupied Molecular Orbital, HOMO (hole creation).

### 4.4.1 Electron excitation

A covalent bond between two-fold and three-fold coordinated atoms was broken (C2+C3 => C1+C2) in the majority of cases when an additional electron was put in the LUMO as seen in Figure 4.10 and in Figure 4.11. The bond breaking significantly affects the bond lengths, which alternates between shrinkage and elongation in the vicinity of the broken bond as being displayed in Figure 4.11. My localization analysis revealed that the LUMO was localized at this site before the bond breaking as it can be seen in Figure 4.12. A release of excitation restores all bond lengths to their original value.

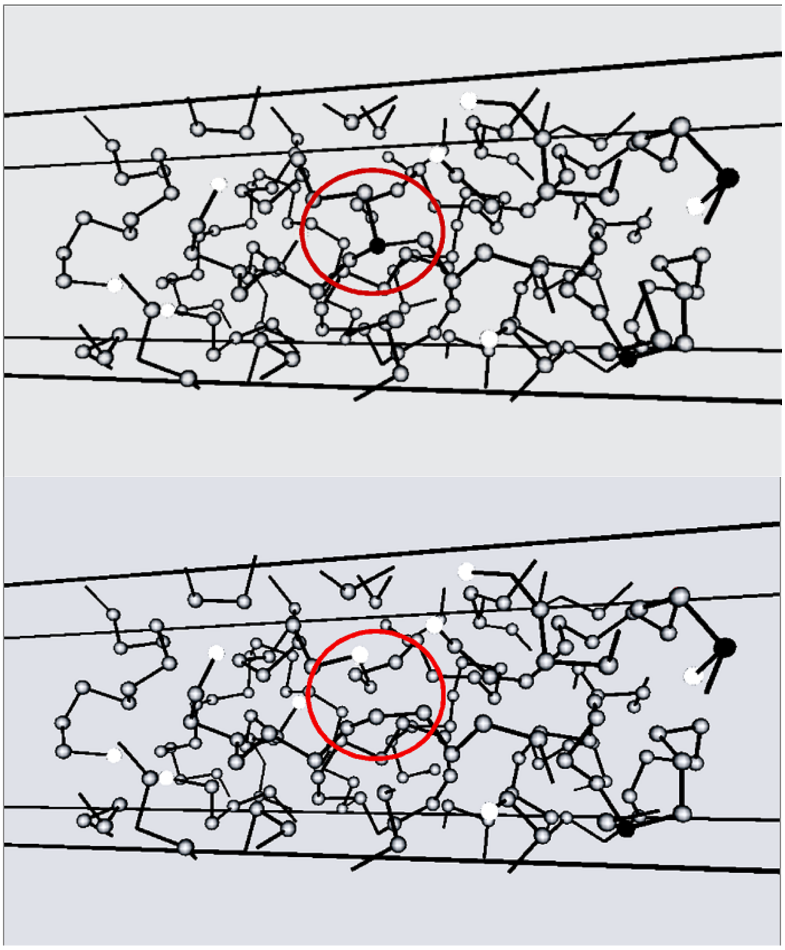

**Figure 4.10 Bond breaking due to electron excitation in an amorphous Selenium structure consisting of 162 atoms. Top figure show the structure before excitation and bottom snapshot was taken during photo excitation. Black colored atoms are three-fold coordinated and white colored atoms are one-fold coordinated.**

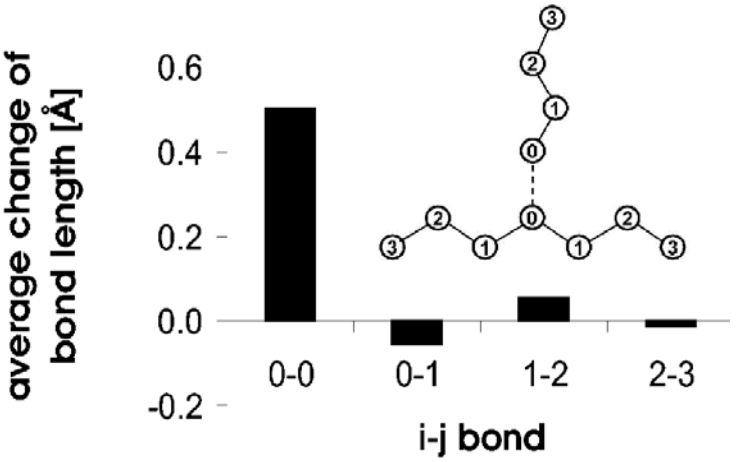

**Figure 4.11. Bond breaking and bond length changes due to electron addition in the LUMO of amorphous Selenium network. Here i and j refer to the numbered atoms in the figure. The dark rectangles represent the average changes in bond lengths between i-j atoms.**

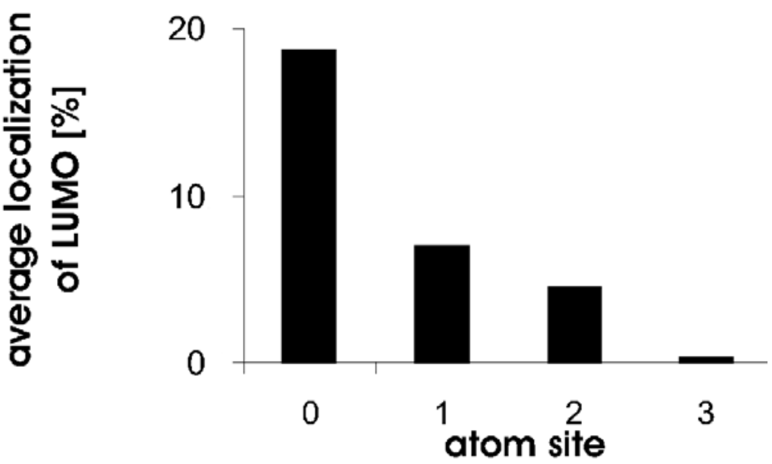

**Figure 4.12. Average localizations of LUMO at the atoms 0, 1, 2, 3. See Fig. 8. for notations.**

In Figure 4.13 the time development of the photo-induced bond breaking in a representative sample is shown. Furthermore, the corresponding *in-situ* volume expansion is also depicted. Bond breaking is due to the added electron to the LUMO. Similar changes were observed in each amorphous Selenium network. Before the excitation at 5 ps the bond length is about 2.55 Å. In this particular case, the bond breaking occurred at a weaker bond due to the C3 site, which had a larger interatomic separation than the majority of the nearest-neighbor bonds (2.4 Å). During the illumination, this weaker bond (2.55 Å) increases by 15 % (in this example to 3 Å) and it decreases to its original value after the de-excitation. (Arrows show the excitation and de-excitations in Figure 4.13) The volume change follows the bond breaking and it shows damped oscillations on the picoseconds time scale.

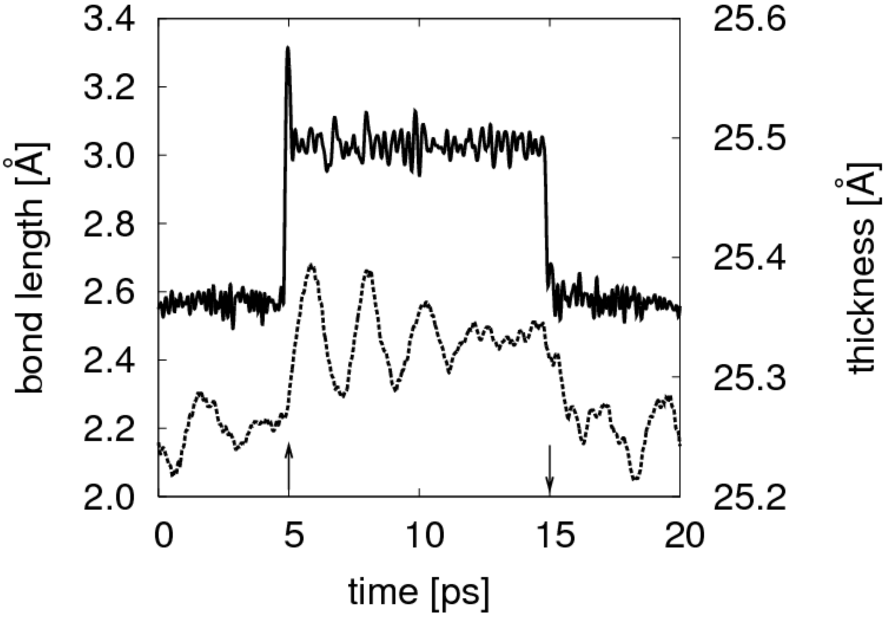

**Figure 4.13. Bond length of breaking bond (solid line) and thickness of sample (dotted line) during photo-excitation. Excitation starts at 5 ps and ends at 15 ps (arrows).**

### 4.4.2 Hole creation

I observed that inter-chain bonds were formed after creating a hole and they cause contraction of the sample (Figure 4.15 and Figure 4.14). This contraction always appears near to atoms where HOMO is localized. Since HOMO is usually localized in the vicinity of a one-fold coordinated atom, the inter-chain bond formation often takes place between a one-fold coordinated atom and a two fold-coordinated atom (C{1,0}+C{2,0} => C{1,1}+C{2,1}, where the second number means the number of inter-chain bonds). However, sometimes I also observed the formation of inter-chain bonds between two two-fold C2 coordinated atoms (C{2,0}+C{2,0} => C{2,1}+C{2,1}).

In order to model the collective effect of photo-induced changes in amorphous Selenium, I also performed simulations with five excited electron creations and five hole creations. I put five excited electrons from the five highest occupied energy levels (one electron from one level) to the five lowest unoccupied energy levels (again, one electron to each level). I found similar effects as described above for single electron/hole creation: bond breakings and inter-chain bond formations have similar characteristics. Nevertheless, in the five excited electron creation case, further bond breaking occurred not only at the C3 sites, but as well at some C2 sites. In the case of the five hole creation, I observed that inter-chain bonds were formed between C1 and C2 sites and also between C2 and C2 sites. The bond breaking and inter-chain bond formation can be understood in terms of a change in the bond strength before and during the excitations. I calculated the bond energies [8] within the TB representation. I obtained decrease in the bonding energy of 0.24 eV after a bond breaking for a typical case. In contrast, a hole addition leads to an increase in the inter-chain bond energy of 0.042 eV.

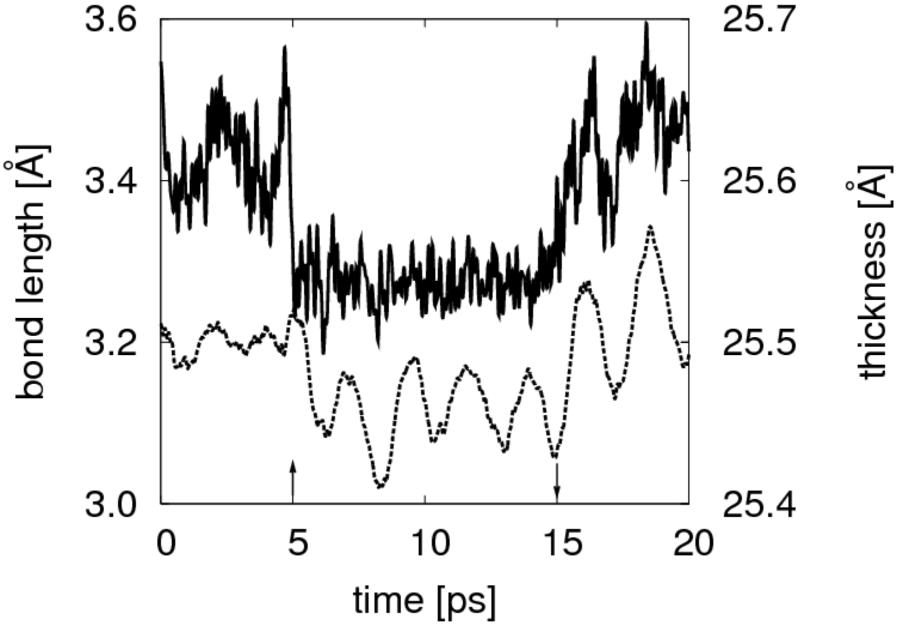

**Figure 4.14. Photo-induced local contraction due to the addition of a hole in a-Se as a function of time. Distance between two atoms in different Se chains at sites where HOMO is localised (solid line). Thickness of sample is denoted with dashed line. Hole is created at 5 ps and annihilated at 15 ps.**

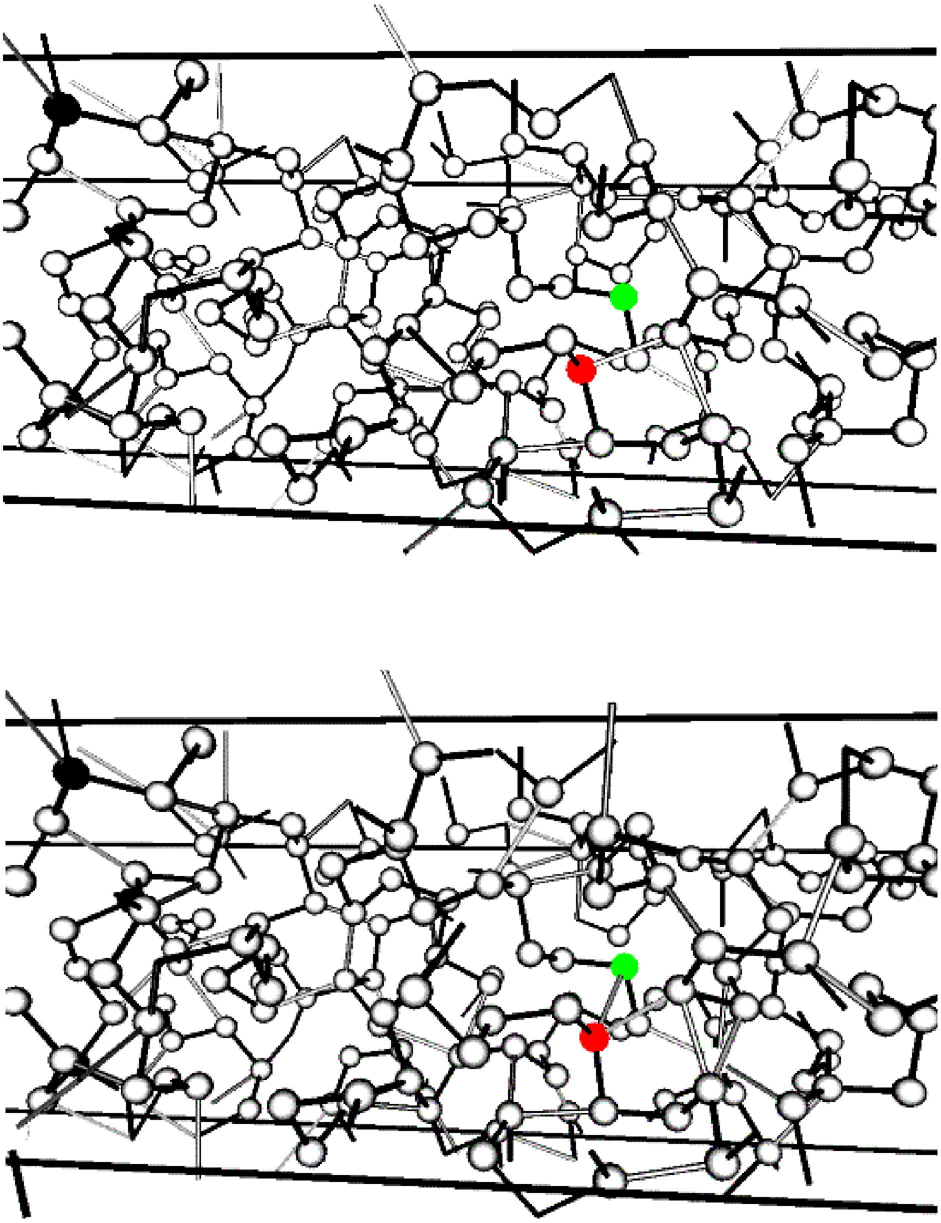

**Figure 4.15. Formation of weak interchain covalent bonds in an amorphous Selenium sample due to photo-excitation. Red and green atoms denote atoms where photo induced interchain formation takes place. Upper panel show the structure before excitation and in the lower panel the snapshot has been taken during excitation. Black bonds denote covalent bonds having bond lengths between 2 Å and 2.8 Å. Grey lines stand for weak interatomic covalent bonds corresponding to interatomic distances between 2.8 Å and 3.4 Å. Note that grey lines never connect second neares-neighbors in the same chain.**

## 4.5 Macroscopic models

### 4.5.1 Ideal, reversible case (a-Se)

The light induced volume expansion and volume shrinkage in amorphous Selenium occur simultaneously and these are additive quantities as my molecular dynamics simulations have confirmed it. The expansion of the thickness $d_e$ is proportional to the number of excited electrons $n_e$ ($d_e = \beta_e n_e$), while the shrinkage $d_h$ is proportional to the number of created holes $n_h$ ($d_h = \beta_h n_h$), where the parameters $\beta_e$ and $\beta_h$ are the average thickness changes caused by an excited electron and a hole, respectively. The time dependent equation of thickness change can then be written as:

$$\Delta(t) = d_e(t) - d_h(t) = \beta_e n_e(t) - \beta_h n_h(t)\,. \tag{1}$$

Assuming $n_e(t) = n_h(t) = n(t)$ I get

$$\Delta(t) = (\beta_e - \beta_h) n(t) = \beta n(t)\,, \tag{2}$$

where $\beta$ is a characteristic constant of different chalcogenide glasses related to photo-induced volume (thickness) change. The sign of this parameter governs whether the material shrinks or expands. The number of electrons excited and holes created is proportional to the duration time of illumination. Their generation rate G depends on the number of incoming photons and on the photon absorption coefficient. After the photon absorption, the separated excited electrons and holes migrate within the amorphous sample and then eventually recombine. A phenomenological equation for this dominant process can be written as:

$$\frac{dn_e(t)}{dt} = G - C n_e(t) n_h(t)\,, \tag{3}$$

where C is a constant. Using $n_e(t) = n_h(t) = n(t)$ and $\Delta(t) = \beta\, n(t)$, I obtain a fundamental equation for the time dependent volume change, namely,

$$\frac{d\Delta(t)}{dt} = G\beta - \frac{C}{\beta}\Delta^2(t)\,. \tag{4}$$

Solution of this nonlinear differential equation is obtained as:

$$\Delta(t) = \beta\left(\frac{G}{C}\right)^{1/2} \tanh\left((GC)^{1/2} t\right). \tag{5}$$

Recently, the photo-induced expansion of amorphous Selenium films was measured *in situ* for the first time using the optoelectronic interference and enhanced by image processing [9]. Figure 4.16 shows the measured time evolution of the surface height in the interval of 0-300 s together with its best fit.

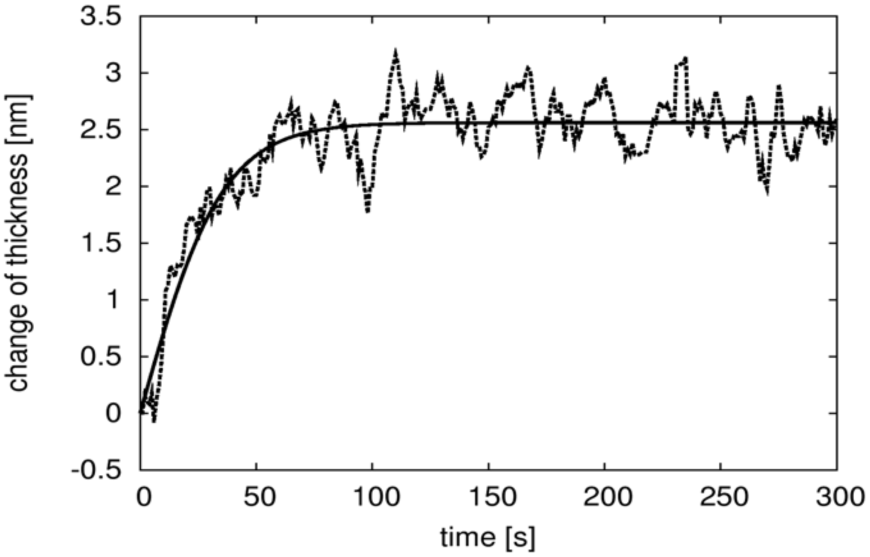

**Figure 4.16. Time development of volume expansion in amorphous Selenium (dashed line) and its theoretical fit (solid line).**

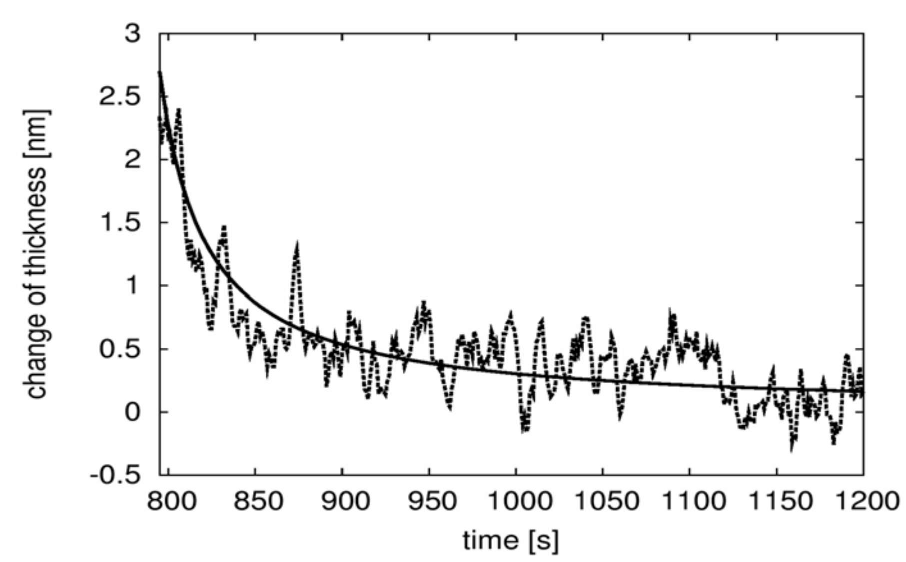

**Figure 4.17. The measured shrinkage of a-Se (dashed line) and the fitted curve (solid line) after stopping the illumination.**

After the light is turned off (G = 0), Eq. (4) can be written as

$$\frac{d\Delta(t)}{dt} = -\frac{C}{\beta}\Delta^2(t), \tag{6}$$

with the solution

$$\Delta(t) = \frac{a}{\left(a\frac{C}{\beta}t + 1\right)}. \tag{7}$$

Figure 4.17 displays the measured volume change and the fitted theoretical curve to the measured data. Light was switched off at t = 800 s.

### 4.5.2 Non-ideal, irreversible case (a-$As_2Se_3$)

In the ideal case I assumed that each local structure variations were reversible and the original local structure were reconstructed after the electron-hole recombination. However, the result of a measured volume change on flatly deposited a-$As_2Se_3$ film is quite different from the ideal Selenium case (See: Figure. 2b in Ref. 13). To explain the difference I must take into account a large number of irreversible changes in the local atomic arrangement i.e. after turning off the light the local configuration remains the same and there is no electron-hole recombination. The total volume change includes both the reversible and irreversible changes and it can be written as:

$$\Delta_{total}(t) = \Delta_{rev}(t) + \Delta_{irrev}(t) \tag{8}$$

The reversible part follows Eqs. (4) and (6) during and after the illumination, respectively, with the corresponding solutions given in Eqs. (5) and (7).

I now consider the irreversible component. During the illumination, the generation rate of irreversible microscopic change is time dependent. Let us consider that an upper limit exists for the maximum number of electrons and holes causing irreversible changes and denoted by $n_{e,irr,max}$ and $n_{h,irr,max}$, respectively. To simplify the derivation let us assume that $n_{e,irr,max} = n_{h,irr,max}$. In this case, one can write the electron generation rate as:

$$G_e(t) = C_e\left(n_{e,irr,\max} - n_e(t)\right). \tag{9}$$

Note that there is no recombination term in Eq. (9). Following Eq. (4), I obtain that the irreversible expansion is governed by :

$$\frac{d\Delta(t)}{dt} = G_{irr} - C_{irr}\Delta(t) \tag{10}$$

Equation (10) then leads to the solution:

$$\Delta_{irr}(t) = \frac{G_{irr}}{C_{irr}}\left(1 - \exp(-C_{irr}t)\right). \tag{11}$$

Using Eqs. (11) in Eq. (8), the best fit of the volume expansion ($\Delta_{total}(t)$), and that of the reversible and irreversible parts ($\Delta_{rev}$ (t), and $\Delta_{irr}$ (t)) are displayed in Figure 4.18.

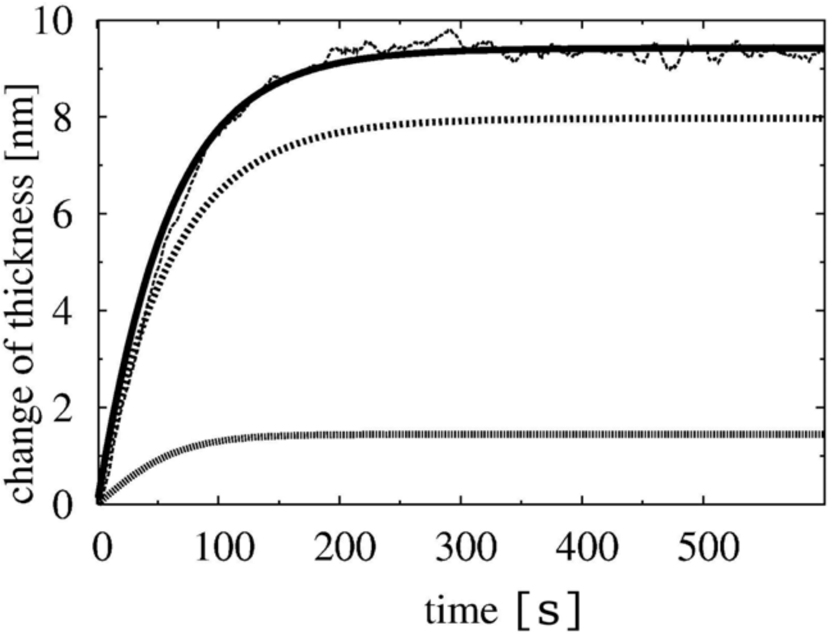

**Figure 4.18. Time development of volume expansion of a-$As_2Se_3$. Thin solid line is the measured curve, thick solid line is the fitted line ($\Delta_{total}(t)=\Delta_{rev}(t)+\Delta_{irr}(t)$). Lower dashed curve is the best fit of $\Delta_{rev}(t)$ while upper one is that of the irreversible part $\Delta_{irr}(t)$.**

After illumination there is no volume change caused by the irreversible microscopic effects. Figure 4.19 shows the shrinkage after switching off the illumination, which is the fit as obtained in the reversible case.

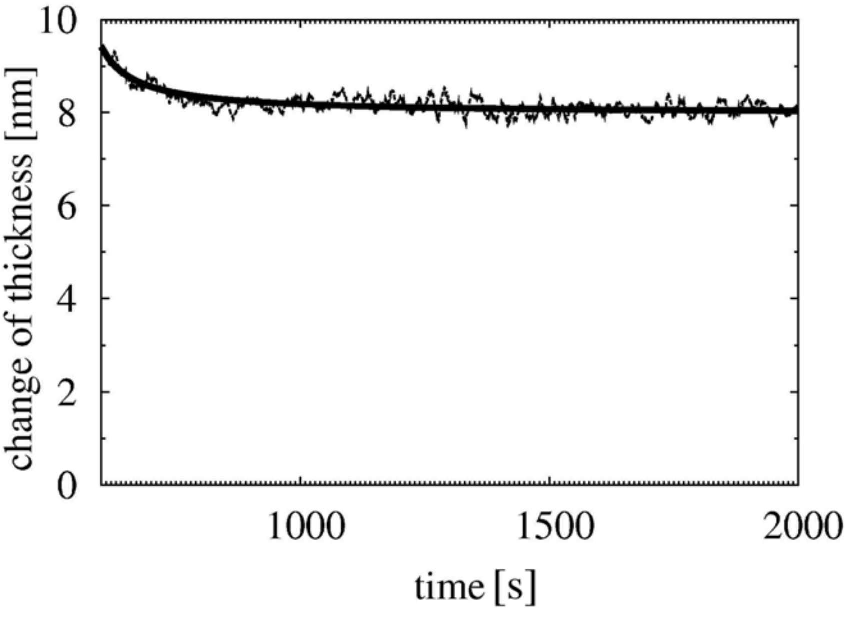

**Figure 4.19. The measured decay (thin solid line) and the fitted theoretical curves (thick solid line) for the shrinkage as a function of time after stopping the illumination.**

## 4.6 Summary

I have proposed a new explanation for the photo-induced volume changes in chalcogenide glasses. I have found that the covalent bond breaking occurs in these glasses with excited electrons, whereas holes contribute to the formation of inter-chain bonds. In the ideal situation both processes are reversible. The interplay between photo-induced bond breaking and inter-chain bond formation leads to either volume expansion or shrinkage. In the non-ideal case, only a part of the processes is irreversible and the total expansion includes the reversible and irreversible changes. My microscopic explanation of the macroscopic photo-induced volume change is consistent with the first *in-situ* surface height measurements.

## 4.7 Bibliography

[1] Ke. Tanaka, N. Kyoya and A. Odajima, Thin Solid Films **111**, 195 (1984)
[2] Y. Kuzukawa, A. Ganjoo, and K. Shimakawa, J. Non-Cryst. Solids **227-230**, 715 (1998) and Philos. Mag. B **79** 249 (1999)
[3] K. Shimakawa, A. Kolobov, and S. R. Elliott, Adv. in Phys. **44**, 475 (1995).
[4] K. Shimakawa, N. Yoshida. A. Gahjoo, A. Kuzukawa, J. Singh, Philos. Mag. Lett. **77**, 153 (1998).
[5] H. Fritzsche, Solid State Commun. **99**, 153 (1996).
[6] A. V. Kolobov, H. Oyanagi, K. Tanaka, and Ke. Tanaka, Phys. Rev. B **55**, 726 (1997).
[7] X. Zhang, and D. A. Drabold, Phys. Rev. Lett. **83**, 5042 (1999).
[8] J. Hegedüs, K. Kohary, D. G. Pettifor, K. Shimakawa, and S. Kugler, Phys. Rev. Lett. **95**, 206803 (2005).
[9] T. Uchino and S.R. Elliott, Phys. Rev. B **67**, 174201 (2003).
[10] T. Uchino, D.C. Clary and S.R. Elliott, Phys. Rev. Lett. **85**, 3305 (2000).
[11] S.I. Simdyankin, M. Elstner, T.A. Niehaus, Th. Frauenheim and S.R. Elliott., Phys. Rev. B **72**, 020202(R), (2005).
[12] S.I. Simdyankin, T.A. Niehaus, G. Natarajan, Th. Frauenheim and S.R. Elliott, Phys. Rev. Lett. **94**, 086401 (2005)
[13] Y. Ikeda, K. Shimakawa, J. Non-Cryst. Solids **338**, 539 (2004).
[14] Jai Singh and Koichi Shimakawa *Advances in Amorhous Semiconductors* (Taylor and Francis, London and New York, 2003)
[15] *Photo-Induced Metastability* (Amorphous Semiconductors, Ed. Alexander V. Kolobov, Wiley-VCH, 2003)
[16] J. Hegedus, K. Kohary, S. Kugler, Journal of Optoelectronics and Advanced Materials **7**, 1923 (2005)
[17] J. Hegedüs, K. Kohary, S. Kugler, J. Non-Cryst. Solids **338**, 283 (2004).
[18] J. Hegedüs and S. Kugler, J. Phys.: Condens. Matter **17**, 6459 (2005)
[19] D. Molina, E. Lomba Phys. Rev. B **60**, 6372 (1999).
[20] E. Lomba, D. Molina, M. Alvarez, Phys. Rev. B **61**, 9314 (2000).
[21] L. Goodwin, A.J. Skinner, and D. G. Pettifor, Europhys. Lett. **9**, 701 (1989)
[22] E. Lomba, D. Molina, M. Alvarez, Phys. Rev. B **61**, 9314 (2000).
[23] J. Hegedüs, K. Kohary, S. Kugler, K. Shimakawa, J. Non-Cryst. Solids **338**, 557 (2004)
[24] F. Shimojo, K. Hoshino, and Y. Zempo, J. Phys.: Condens. Matter **10**, L177 (1998)
[25] http://www.physik.uni-marburg.de/~joco/JGLMOL.html

# Summary

The thesis consists of three main parts: i) kinetic Monte Carlo simulation of step-bunching on crystalline surface during growth, ii) molecular dynamics simulation of growth of amorphous semiconductors, iii) tight-binding molecular dynamics investigation of photo-induced phenomena in amorphous Selenium.

In Chapter 2 I have investigated the influence of immobile impurities on epitaxial growth for the first time using two dimensional kinetic Monte Carlo simulations, more specifically how immobile impurities cause step-bunching. I have implemented a kinetic Monte Carlo code which is capable to simulate the deposition of about one million atoms in the relevant parameter regime. I have instigated systems with two, three and eight steps. Systems with two steps showed three different type of behavior corresponding to the type of impurities. Systems show step-pairing if I co-deposit impurities which cause extra potential barriers on the surface, i.e. impurities which hinder diffusion locally. If impurities do not effect the potential barrier for hopping of adatoms on the flat surface then the time development of the terrace sizes follow random walk behavior and do not show either any sign of step-pairing nor any tendency to equalize distances between steps. By co-depositing impurities which enhance local diffusion I observed terrace size-equalization after the deposition of ten monolayers. More complicated situation arises in the case of three steps. The time development of the terrace sizes even in the absence of impurities shows a more complex behavior due to the coupling between velocities of neighboring steps through shared terrace. That is the reason why oscillations of terrace sizes can be observed even in the case of no impurities. Impurities can either enhance or suppress the oscillations but they do not cause stable step-pairing any more, as this was the case when considering only two steps. Step-pairing can be observed in the case of three-steps, but step-pairs remain only bound for the time needed to depozit about one monolayer. In the case of eight-steps I investigated the interaction between steps. By applying impurities which enhance local diffusion it is possible to equalize the terrace sizes in the case of systems with eight steps. No step-bunching has been observed when I co-deposited impurities which suppress local diffusion, only step-pairs have been clearly observed which were stable only for the deposition time of about two monolayers. Step pair formation and dissolution shows wave like behavior. Simulation results suggests that although impurities effect the growth dynamics substantially, but no step-bunching takes place as the direct consequence of the presence of impurities in the system. It may happen however that larger step-bunches form under certain conditions due to complex behavior of the system if the system size and number of deposited impurities becomes macroscopically large. The situation is expected in that case to be similar to traffic jams on highways.

In Chapter 3 I investigated the growth of amorphous semiconductors using molecular dynamics simulation. Chapter 3 has three main sections where I discuss results (Section 3.3, Section 3.4 and Section 3.5).

In Section 3.3 I present results on molecular dynamics simulation of preparation methods of amorphous Selenium using classical empirical potential to describe interatomic interactions. Classical empirical potentials enable the simulations of large systems (1000-2000 atoms) and long time scales (1-2 ns) on a single processor. I have compared structures grown at different bombarding energies (0.1 eV, 1 eV and 10 eV) keeping all other parameters unchanged: substrate temperature is 100 K,

injection rate is one atom in every 300 fs. I have observed strong dependence of the densities on the bombarding energies. The density increases with bombarding energy: 3.21 g/cm$^3$ (0.1 eV), 3.73 g/cm$^3$ (1 eV) and 4.34 (10 eV) g/cm$^3$. I have noticed that number of backscattered atoms increases with decreasing bombarding energy. Kinetics of the growth is different depending on bombarding energy. In the case of 0.1 eV bombarding energy a porous structure is built up with voids. These voids become filled up by atoms in a later stage of the bombardment. On the other hand, in the case of 1 eV bombarding energy there is no difference between early and late stages of growth. I also compared different preparation techniques: growth versus rapid quenching. The rapid quenched sample was more homogeneous than its grown counterpart, this can be explained by the smaller number of voids present in the rapid quenched sample. I compared physical properties of the prepared amorphous samples with diffraction measurements both on amorphous samples and on large number of Selenium containing molecules. The simulation produced a too narrow first neighbor peak when compared to diffraction measurements on amorphous samples. Agreement with structure of molecules was on the other hand remarkable, both with respect to bond length and to bond angle distributions.

In Section 3.4 I have compared amorphous Selenium structures grown using three different type of interatomic potentials with various accuracy to determine when it is necessary to use the more accurate but more CPU intensive method. The three applied potentials were: a classical empirical potential (CLASS), a tight-binding model without Hubbard-term (TB-NOHUB) and a self-consistent tight-binding model with Hubbard-term (TB-HUB). The Hubbard term helps to avoid any large charge transfer. I analysed the structural properties of the obtained amorphous networks: significant differences were found in the radial distribution functions, bond angles, dihedral angles and coordination defects. Furthermore, I have presented statistics based on a large number of diffraction measurements on molecules containing Selenium fragments. I observed an increase in bond length with decreasing bond angle. Only model TB-HUB did not reproduce this experimental result. Overall, model TB-HUB is the most realistic amorphous Selenium network. Model TB-NOHUB is unacceptable due to it is high number of coordination defects.

In Section 3.5 I describe the results after I have implemented a recently proposed tight-binding model for Silicon (Lenosky model) in the ATOMDEP program package. This new model should perform much better than previous versions. My motivation was to produce good quality structural models of amorphous Silicon and I was also motivated by the fact that – to my knowledge – the potential has not been tested so far for disordered structures. I have prepared an amorphous Silicon sample using the same procedure and physical parameters that have been used by K. Kohary who has applied a different tight-binding description developed by Kwon *et al*. My aim was to compare the two structural models and decide which tight-binding model is more appropriate to provide good amorphous Silicon structures. I have compared densities, bond lengths, bond angles, number of coordination defects, number of triangles and squares. The most decisive difference can be seen in the description of coordination defects. The Kwon model produces six-fold and two-fold coordinated defects while the Lenosky model not. I have also examined the compatibility of both tight-binding models with the Wooten-Winer-Weaire amorphous Silicon structural model which has 100 % four-fold coordinated atoms. I have relaxed the Wooten-Winer-Weaire model containing 216 atoms at T=0 K with both tight-binding models and calculated the number of coordination defects in the models. The two tight-binding models produced opposite results: the Lenosky model introduced three-fold coordinated defects, while the Kwon model five and six-fold coordinated defects. Overall, I conclude that the Lenosky model provides better description for amorphous Silicon, the most important reason for this is that the Lenosky model does not produce six-fold coordinated defects in the amorphous structure. Such defects should be present only in liquid phase.

In Chapter 4 I present results on tight-binding molecular dynamics simulation of photo-induced phenomena in amorphous Selenium. In isolated eight-member Selenium ring and in isolated Selenium chain I have observed bond-breaking after transferring one electron from the highest occupied molecular orbital to the lowest unoccupied molecular orbital. Following this finding I simulated the behavior of a 162 atom amorphous Selenium network under photo-excitation. In that calculations I assumed that electron-hole interaction can be neglected because the energy scale of the potential fluctuations due to disorder is larger than the typical energy of electron-hole coupling. Therefore I handled electrons and holes separately and I simulated electron creation and hole creation in separate runs. Based on the simulation results I have proposed a new explanation for the photo-induced volume changes in chalcogenide glasses. I have found that covalent bond breaking occurs in the networks with excited electrons, whereas holes contribute to the formation of inter-chain bonds. In the ideal situation both processes are reversible. The interplay between photo-induced bond breaking and inter-chain bond formation leads to either volume expansion or shrinkage. Therefore, both the expansion and the contraction of chalcogenide glasses can be described in this frame, supported by molecular dynamics simulations. I also considered the non-ideal case, where only a part of the processes is irreversible and the total expansion includes reversible and irreversible changes. The microscopic explanation of the macroscopic photo-induced volume change is consistent with the first *in-situ* surface height measurements. By showing that tight-binding molecular dynamics simulations are capable to predict and explain physical processes on the atomic level I have pioneered one way for future simulations on photo-induced phenomena.

# Zusammenfassung (In German)

Die Doktorarbeit besteht aus drei Teilen: i) kinetische Monte Carlo Simulationen von Stufenbündeln während epiktaktischen Wachstums in kristallinen Materiallen, ii) molekulardynamische Simulation von Wachstum von amorphen Halbleitern, iii) Tight-binding molekulardynamische Simulationen von lichtinduzierten Phänomenen in amorphem Selen.

Im Kapitel 2 ich habe den Effekt von nichtbeweglichen Störstellen auf Stufenbündel während epiktaktischen Wachstums untersucht. Dabei habe ich kinetischen Monte Carlo Simulationen verwendet. Ich habe den Computercode selbst implementiert. Das Programm ist in der Lage, die Ablagerung von einer Millionen Atomen in dem relevanten Parameterregime zu verfolgen. Ich habe Systeme mit zwei, drei und acht Stufen untersucht. Systeme mit zwei Stufen zeigen drei verschiedene Verhalten entsprechend den Typen der Störstellen. Wenn die abgelagerten Störstellen die lokale Diffusion unterdrücken, dann zeigt das System das Paaren von Stufen. Wenn die Störstellen die lokale Diffusion nicht beeinflussen, dann entspricht die Zeitentwicklung der Fläche der Terrassen einem Zufallsweg und es deutet nichts darauf hin, dass das System entweder das Paaren von Stufen oder das Angleichen der Terrassengrößen bevorzugen würde. Wenn die Störstellen die lokale Diffusion fördern, hat das System die Präferenz, Terrassen von gleicher Größe zu bilden. Die Situation wird komplizierter wenn drei Stufen in dem System sind. Die Zeitentwicklung der Terrassengrossen zeigt ein komplizierteres oszillierendes Verhalten auch in der Abwesendheit der Störstellen wegen der Kopplung der Geschwindigkeiten von nebenaneinanderliegenden Stufen durch Teilung der selben Terrassen, von denen die Adatome von den beiden Stufen eingesammelt werden. Störstellen können die Oszillationen entweder verstärken oder dämpfen, je nachdem, ob die Störstellen die lokale Diffusion hindern oder fördern. Das Paaren von Stufen kann auch in dem System mit drei Stufen beobachtet werden, aber es bilden sich keine Tripel von Stufen. Die Paaren sind nur für kurze Zeit stabil, weil Sie nach dem Entstehen sich bald wieder auflösen. In dem Fall von acht Stufen kann die Wechselwirkung der Stufen untersucht werden. Störstellen, die die lokale Diffusion fördern, führen zu ausgeglichenen Terrassengrößen. Gegen die Erwartung passiert kein Stufenbündeln, wenn die Störstellen die lokale Diffusion hindern. Außerdem kann ein Wellenverhalten von Entstehen und Auflösen der Stufenpaare beobachtet werden.

In Kapitel 3 untersuche ich das Wachstum von amorphen Halbleitern. Das Kapitel hat drei Hauptteile, in denen ich die Resultate diskutiere: Sektion 3.3, Sektion 3.4 and Sektion 3.5.

In Sektion 3.3 stelle ich meine Ergebnisse über die molekulardynamische Untersuchung von verschiedenen Herstellungsmethoden des amorphen Selens vor. Dabei verwende ich ein klassisches empirisches Potenzial, um die interatomare Wechselwirkung zu beschreiben. Dies ermöglicht die Simulation von großen Systemen (1000-2000 Atomen) und von langen Zeitskalen (1-2 ns) auf einem einzigen Prozessor. Zuerst habe ich amorphe Strukturen verglichen, die mit verschiedener Bombardierungsenergie gewachsen waren (0.1 eV, 1 eV and 10 eV). Ich habe dabei alle anderen Parameter unverändert gelassen, die Temperatur des Substrates ist 100 K, Ablagerungsgeschwindigkeit ist ein Atom je 300 fs. Ich habe festgestellt, dass es eine starke Abhängigkeit der Dichten von der Bombardierungsenergie gibt. Die Dichte steigt mit der Bombardierungsenergie an: 3.21 g/cm$^3$ (0.1 eV), 3.73 g/cm$^3$ (1 eV) and 4.34 (10 eV) g/cm$^3$. Außerdem, habe ich festgestellt, dass die Anzahl von rückgestreuten Atomen anwächst, wenn die Bombardierungsenergie niedriger wird. Die Kinetik des Wachstums ist unterschiedlich, je nach dem, ob man große (1 eV) oder kleine Bombardierungsenergie nimmt. Bei niedrigerer Bombardierungsenergie (0.1 eV) entsteht zuerst eine poröse atomare Struktur auf der Oberfläche und die Lücken in dieser Struktur werden später langsam mit Atomen aufgefüllt. Bei höheren Bombardierungsenergien gibt keinen Unterschied zwischen frühen und späten Stadium des Wachstums, weil es keine poröse Struktur entstehen kann. Ich habe auch verschiede Präparationstechniken verglichen: Wachstum und rapides Kühlen. Die atomare Struktur der amorphen Dünnschicht, die durch rapides Kühlen hergestellt wurde, ist homogener als die Dünnschicht, die durch Wachsen hergestellt wurde. Ich habe meine Ergebnissen mit Streuungsmessungen von amorphem Selen und von Molekülen, die Selen enthalten, verglichen. Die simulierte Struktur hat ein zu schmalen erste Nachbar Peak in der radialen Verteilungsfunktion verglichen mit den Streuungsergebnissen von amorphem Selen. Die Übereinstimmung mit Streuergebnissen von Molekülen, die Selenatome enthalten, ist gut.

In Sektion 3.4 habe ich verschiedene amorphe Strukturen verglichen, die mit unterschiedlichen atomare Wechselwirkungen hergestellt worden sind, um zu bestimmen, wann man quantensmechanische Beschreibung statt klassische Beschreibung verwenden muss. Die drei verwendeten Potentiale waren: klassisches empirischen Potential (CLASS), tight-binding Model ohne Hubbard-Größe (TB-NOHUB) und ein selbstkonsistentes tight-binding Model mit Hubbard-Größe (TB-HUB). Die Hubbard Größe hilft Ladungstransfer zu vermeiden und die Atome zu neutralisieren. Ich habe die strukturellen Eigenschaften der entstandenen amorphen Netze analisiert: signifikante Abweichungen können in der radialen Verteilungsfunktion, Bindungswinkelverteilungsfunktion, dihedrische Winkelverteilungsfunktion und Koordinationsdefekten auftreten. Außerdem, habe ich Statistiken über Streuungsversuche von Molekülen, die Selen enthalten, präsentiert. Ich habe einen Zusammenhang zwischen Bindungslänge und Bindungswinkeln festgestellt: mit wachsende Bindungslänge nimmt der Bindungswinkel ab. Nur Model TB-HUB hat dieses Ergebnis nicht reproduziert. Model TB-HUB ist das realistischste amorphe Selennetz unter den drei Modellen. Model TB-NOHUB ist nicht akzeptabel, weil es zu viele Koordinationsdefekten enthält.

In Sektion 3.5 beschreibe ich die Ergebnissen der Computersimulation von amorphem Silizium, nachdem ein neues tight-binding Model für Silizium (Lenosky Model) ich implementiert habe. Das neue Model soll viel bessere Ergebnisse liefern als die vorherige Version, entwickelt von Kwon *et al.* Meine Motivation war, gute strukturelle Modelle von amorphem Silizium herzustellen und ich war auch durch das Fakt motiviert, dass das neue tight-binding Model (Lenosky Model) noch nicht an amorphen Strukturen getestet wurde. Ich hab eine amorphes Siliziumnetz präpariert, so dass ich die selben Parameterwerte benutzt habe, die auch K. Kohary in seiner Doktorarbeit benutzt hat, in der er das Silizium tight-binding Model von Kwon angewendet hatte, um ein amorphes Siliziumnetz zu modellieren. Mein Ziel ist es, die beiden tight-binding Modelle (Lenosky vs. Kwon) zu vergleichen und festzustellen, welches Model, in welcher Hinsicht, sich als besser erweist. Ich habe Dichten, Bindungslängen, Bindungswinkel, Koordinationsdefekte, Anzahl von Drei- und Vierecken verglichen. Der größte Unterschied war in der Beschreibung von Koordinationsdefekten zu finden. Das Kwon Model erzeugt sechs- und zweifache Koordinationsdefekte und das Lenosky Model nicht. Ich habe auch die Kompatibilität mit dem Wooten-Winer-Weaire Model untersucht. Das Wooten-Winer-Weaire Model ist ein Modelnetzwerk des amorphen Siliziums, das hundertprozentige vierfache atomare Koordination zeigt. Ich habe das Wooten-Winer-Weaire Model mit beiden tight-binding Modellen bei T=0 K relaxieren lassen. Dann habe ich die Anzahl von Koordinationsdefekten in den Modelle bestimmt. Die zwei verschieden tight-binding Modele haben entgegengesetzte Ergebnisse produziert: das Kwon Model fünf- und sechsfache Koordinationsdefekte, dagegen das Lenosky Model dreifach koordinierte Defekte produzierte. Im Allgemeinen beschreibt das Lenosky Model amorphes Silizium besser als das Kwon Model, weil das Lenosky Model nicht sechsfache Koordinationsdefekten produziert, die nur im flüssigen Silizium vorkommen sollten.

Im Kapitel 4 präsentiere ich Ergebnisse über tight-binding Computersimulation von photo-induzierte, Phänomene, in amorphem Selen. In einem isolierten Selenring bestehend aus acht Atomen und in einer isolierten Selenkette bestehend aus achtzehn Atomen habe ich Bindungsbrechen nach dem Transferieren eines Elektrons aus den höchsten nichtbesetzten molekularen Orbital in das niedrigste besetze molekulare Orbital beobachtet. Nach diesem Ergebnis habe ich das Verhalten eines amorphen Selennetzwerkes während Photoanregung simuliert. In diesen Rechungen habe ich die Elektron-Loch Wechselwirkung vernachlässigt, weil die Energieskala der Potentialfluktuationen infolge der Unordnung größer als die typische Energieskala der Elektron-Loch Wechselwirkung ist. Deswegen habe ich Elektronen und Löcher voneinander getrennt behandelt, indem ich zwei verschiedene Simulationen für die Simulation einer Photoerregung durchgeführt habe: eine, in der ein extra Elektron erzeugt wird, und eine, in der ein extra Loch erzeugt anders gesagt, ein Elektron entfernt wird. Auf dieser Ergebnissen basierend habe ich eine neue Erklärung für die lichtinduzierte Volumenänderung in kalkogenen Gläsern vorgeschlagen. Ich habe gefunden, dass kovalentes Bindungsbrechen infolge einer Elektronerzeugung und das Entstehen schwacher kovalente Interkettigen-Bindungen infolge einer Elektronvernichtung stattfindet. Das Zusammenspiel des Entstehendes einer Interkettigen Bindung und des Bindungsbrechens kann entweder eine makroskopische Ausdehnung oder Zusesamenziehung verursachen. Beide Phänomene können in diesem Bild beschrieben werden. Ich habe auch den nichtidealen Fall untersucht, in dem nur ein Teil der Prozesse reversibel ist und die totale Volumenänderung aus zwei Teilen besteht: reversible und irreversible Teile. Die mikroskopische Beschreibung der Volumenänderungen ist mit den *in-situ* Messungen konsistent. Damit habe ich gezeigt, dass molekulardynamische Simulationen lichtinduzierte Volumenänderungen erklären können und habe den Weg für zukünftige molekulardynamische Simulationen photo-induzierter Phänomene gebahnt.

# Összefoglalás (In Hungarian)

A doktori dolgozatom három részből áll: i) lépcsőtorlódás kinetikus Monte Carlo szimulációja, ii) amorf félvezetők növesztésének molekuláris dinamikai modellezése, iii) fény által okozott térfogváltozás tight-binding molekuláris dinamikai vizsgálata amorf szelénben.

A második fejezetben a nem-mozgékony szennyezők által okozott lépcsőtorlódást vizsgálom kinetikus Monte Carlo szimulációval. Kifejlesztettem egy programot amivel akár egy millió atom növesztését is szimulálni lehet. Különböző méreteket vizsgáltam: két, három ill. nyolc lépcsőt tartalmazó rendszereket. A két lépcsőt tartalmazó rendszerek három fajta eltérő viselkedést mutattak, attol függően, hogy milyen típusúak voltak a szennyező atomok. Lépcsőpárok képződése figyelhető meg, ha a szennyeződések a lokális diffúziót akadályozzák. Ha a szennyeződések nem befolyásolják a diffúziót, akkor a teraszméretek időfejlődése véletlen bolyongással írható le és a rendszer nem mutatja semmi jelét lépcsőpárok képződésének vagy a teraszméretek kiegyenlítődésének. Ha olyan szennyeződéseket juttatok a felületre, amelyek a lokális diffúziót elősegítik, akkor a teraszméretek kiegyenlítődését figyelhetem meg körülbelül tíz atomi réteg lerakódása alatt. A rendszer viselkedése bonyolultabb volt három lépcső esetében. Még a szennyeződések távollétében is komplex viselkedés figyelhető meg, a lépcsők sebességének a megosztott teraszokon keresztül való csatolása miatt. Ez a csatolás az oka, amiért oszcilláció jelenik meg a teraszméretek időfejlődésében még akkor is, ha nincsen a rendszerben szennyeződés. Szennyeződések vagy felerősítik vagy elnyomják az oszcillációkat, de nem vezetnek stabil lépcsőpárok képződéséhez, ellentétben azzal, ahogy a két lépcsős rendszerek esetében történt. Lépcsőpárok képződése ugyan rövid időre megfigyelhető, ezek hamar felbomlanak a képződés után. Nyolc lépcsőt tartalmazó rendszer esetében a lépcsők kölcsönhatását vizsgáltam. Azok a szennyeződések, amelyek elősegítik a diffúziót, a teraszméretek kiegyenlítődését okozzák. Lépcsőpárok képződése igen, azonban lépcsőtorlódás nem volt kimutatható a lokális diffúziót akadályozó szennyeződések esetében. A lépcsőpárok képződése és újra szétválása hullámszerű viselkedést mutatott. A szimulációs eredmények kis rendszerekre azt jósolják, hogy nem jelenik meg lépcsőtorlódás a szennyeződések hatására a várakozással ellentétben. Azonban nagy rendszerekre megtörténhet az, hogy a bonyolult lépcsőkölcsönhatás egy lépcsőtorlódáshoz vezet, hasonlóan mint ahogy forgalmi dugók megjellenek az autópályákon, még akkor is ha nem volt baleset.

A harmadik fejezet három alrészre bomlik. A 3.3-as részben az amorf szelén előállításának molekuláris dinamikai szimulációját disszkutálom. Ebben a fejezetben egy klasszikus empirikus potenciál felhasználásával elértem, hogy nagy rendszerek váljanak szimulálhatóvá. Három különböző bombázási energiával készült amorf struktúrát hasonlítottam össze (0.1 eV, 1 eV, 10 eV), miközben minden más paramétert változatlanul hagytam: a szubsztrátum hőmérséklete 100 K volt, az injektálási frekvencia pedig 1/300 fs volt. Erős összefüggést találtam a bombázási energia és a sűrűség között: növekedő energiával nőtt a sűrűség: 3.21 g/cm$^3$ (0.1 eV), 3.73 g/cm$^3$ (1 eV) and 4.34 (10 eV) g/cm$^3$. A visszaszórt atomok száma is jelentősen nőtt a bombázási energia csökkentésével. A növekedés kinetikája különböző a bombázási energiától függően. Ha 0.1 eV-al bombázunk akkor először egy lyukacsos struktúra alakul ki, majd ez töltődik fel a későbbiekben. Nagyobb energiáknál ilyen lyukacsos elő-struktrúra nem alakul ki. Összehasonítottam különböző készítési eljárással gyártott amorf szelen mintákat is: a növesztést a gyorshűtéssel. A gyorshűtéssel készült minta homogénebb volt és kevesebb lyukat tartalmazott. Összehasonlítottam a kapott struktúrákat diffrakcióból származó kisérleti eredményekkel is, amelyeket vagy amorf mintából nyertek vagy szelén atomokat tartalmazó molekulákból. Az egyezés figyelemreméltó.

A 3.4-as részben különböző atomi potenciálok felhasználásával készített amorf szelén szerkezeteket hasonlítottam össze, hogy megállapítsam mikor érdemes használni a pontosabb, de lassabb kvantum mechankiai leírást. Három eltérő potenciált használtam: klasszikus empirikus (CLASS), szoros kötésű modelt Hubbard tag nélkül (TB-NOHUB) és egy önkonzisztens szoros kötésű modellt Hubbard taggal (TB-HUB). A Hubbard tag kiegyenlíti az atomi töltéseket. Elemeztem a kapott amorf struktúrákat és szignifikáns eltérést találtam a radiális eloszlásfüggvényekben, a kötés és dihedrális-szög statisztikákban és a koordinációs hibahelyek relatív számában. Összehasonlítottam az eredményeket diffrakciós mérésből kapott értékekkel. A kisérleti eredmények negatív korrelációt mutattak a kötésszögek és kötéshosszak között. Csak a TB-HUB model nem reprodukálta ezt a függést. Mindent összevetve a TB-HUB potenciál teljesített a legjobban és a TB-NOHUB model elfogadhatatlan eredményt produkált a sok koordinációs hibahely miatt.

A 3.5-ös részben diszkutálom az amorf szilíciumra kapott eredményeimet. Készítettem egy programot, ami a Lenosky féle szoros kötésű modelt használja a molekuláris dinamikai szimuláció során az atomi kölcsönhatás modellezésére. Ez a model sokkal jobb mint az elődjei és tudomásom szerint én vagyok az első aki amorf szilíciumon tesztelte. A célom az, hogy jó minőségű amorf szilícium struktúrát állítsak elő. Növesztéssel készítettem egy amorf szilícium szerkezetet és ezt hasonlítottam össze a Koháry Krisztián által készített szerkezettel, amely a Lenosky potenciál elődjének felhasználásával készült (Kwon potenciál). A célom az volt, hogy eldöntsem melyik potenciál ad jobb struktúrákat. Összehasonítottam a sűrűségeket, a kötéshosszakat, a kötésszögeket és a koordinációs helyek relatív számát. A legdöntőbb különbséget a koordinációs hibahelyek leírásában találtam: a Kwon model kettes és hatos defekteket hoz létre, míg a Lenosky modell nem. Összehasonlítottam ezentúl a Wooten-Winer-Weaire modellel való kompatibilitásukat is a szoros kötésű potenciáloknak. A Wooten-Winer-Weaire model 100%-os négyes koordináltságú atomokból áll. A modell relaxáltatása után megvizsgáltam a koordinációs számokat. A Lenosky potenciál csak hármas defekteket hozott létre, míg a Kwon csak ötös és hatos defekteket. Összefoglalva az eredményeket a Lenosky modelt találtam realisztikusabbnak, mert az nem hoz létre hatos koordináltságú defekteket, amelyek csak a folyékony halmazállapotban kellenének, hogy megtalhatóak legyenek.

A negyedik fejezetben a foto-indukált térfogváltozás molekuláris dinamikai szimulációját mutatom be. Először izolált szelénium gyűrűben és láncban vizsgálom a fotogerjesztésre adott reakciót és mindkét esetben kötésfelszakadást találok. Ezután több 162 atomot tartalmazó amorf szelenium szerkezetekben vizsgálom a photogerjesztést úgy, hogy a lyuk elektron kölcsönhatást elhanyagolom a rendezetlenség által okozott energiafluktuáció miatt. Két sorozat szimulációt futtatok: elektrongerjesztés és lyukgerjesztés. Az elektrongerjesztés kötéstfelszakadást és a minta kitágulását okozza, míg a lyukgerjesztés gyenge láncközötti kötések kialakulását és a minta összehúzódását okozza. Ezek alapján egy új, univerziális modellt javasoltam a kalkogén üvegekben létrejövő fotoindukált térfogatváltozás leírására. Mivel a teljes térfogatváltozás a modell szerint a tágulás és összehúzódás összejátéka, ez megmagyarázza, hogy egyes kalkogén anyagok miért mutatnak tágulást mások pedig összehúzódást. Az ideális reverzibilis eseten túl az irreverzibilis esetet is tárgyaltam, ahol reverzibilis és irreverzibilis változások összegével irható le a jelenség. A modellből adódó eredményeket összehasonlítottam valós idejű mérésekkel és kiváló egyezés adódott. Az általam végzett molekuláris dinamikai szimuláció úttörő példát mutat hasonló kutatásoknak, ahol számítógépes szimulációval tanulmányozzák majd a fotoindukált változásokat kalkogén üvegekben.

# Acknowledgements

I thank to Prof. Sándor Kugler for much more than supervision of my work. I met him for the first time six years ago when I was a student at Budapest University of Technology. With him my research carrier begun. He helped me all the way from being his diploma student to finishing my PhD thesis. I have learnt from him about the physics of amorphous materials and their computer simulations. He taught me how to write a scientific paper and how to organize my work efficiently. I have learnt how to choose excellent scientific research topics i.e. to study the photo-induced changes in amorphous chalcogenides. These materials might become as important as Silicon in the 20th century because of their potential application in non-volatile memories. Prof. Sándor Kugler taught me much more than physics. I have learned how to give excellent talks and write convincing research proposals. He taught me about people, music, history and humor. Without his help and caring I would be not as successful now as I became under his wings. I am grateful to fate that I met him because he made a tremendously positive influence on my life what I will always carry with myself.

I thank to Prof. Peter Thomas who made it possible for me that I become a fellow of the European Graduate College “Electron-Electron Interactions in Solids”. In Marburg he supervised my PhD work and helped me to fit into the new environment. I have learned from Prof. Peter Thomas about the physics of semiconductors and disordered systems. He managed my research and always helped me wholeheartedly when I had any problem. I thank to him for more than being an excellent supervisor. I will never forget the excursions made together, the deep philosophical discussions in the coffee houses of Budapest and the happy hours in the Weinlädele in Marburg. I thank to Prof. Peter Thomas. It is beyond expression how much his goodwill and help contributed to my success in life.

I am indebted to Dr. Jürgen Vollmer, who helped me in the kinetic Monte Carlo simulations of crystal growth. His passion and enthusiasm about physics enchanted me always when we were discussing our results.

I am indebted to Prof. Stephen R. Elliott and to Prof. Sergei Baranovski for refereeing my PhD thesis. I thank to Dr. Krisztián Koháry. Who helped me in developing the tight-binding molecular dynamics code and in simulation of amorphous materials. I am grateful for the valuable discussions with him. I thank to Koichi Shimakawa for his experimental support. I am indebted to PD Dr. Wolfgang Stolz and Dr. Kerstin Volz who led me into the science of epitaxial growth, to Dr. Frank Grosse who helped me in developing the kinetic Monte Carlo simulation code, to Dr. Laszló István who answered my questions in quantum chemistry, to PD Dr. Torsten Maier who helped me to use parallel computers at the Jülich supercomputer center. I thank to Prof. Joachim Krug for his help in the theory of impurity induced step-bunching.

I am glad that my mother, Teréz Illés will see her son to became a doctor and my sister, Anita Hegedüs can be proud of her brother. It has been a long way. So many things happened in the past, good and bad. My mother and my sister stood beside me on my long journey. I thank to my mother that she has realized my talent and brought me to the best school in Hungary. Anita helped me with love in all my life. I thank so many things to them. I want to see them always as happy as I am now.

# List of publications

**Publications in peer reviewed international scientific journals:**

1. J. Hegedus, K. Kohary, S. Kugler, "Universal feature of photo-induced volume changes in chalcogenide glasses", Journal of Non-Crystalline Solids **352** 1587 (2006)

2. J. Hegedus, K. Kohary, D. G. Pettifor, K. Shimakawa, and S. Kugler, "*Photo-induced volume changes in amorphous selenium*", Physical Review Letters **95**, 206803 (2005)

3. J. Hegedus, K. Kohary, S. Kugler, "*Light-induced volume changes in glassy selenium II. Kinetics of volume expansion*", Journal of Optoelectronics and Advanced Materials **7**, 2231 (2005)

4. J. Hegedus, S. Kugler, "*Growth of amorphous selenium thin-films: classical versus quantum mechanical molecular dynamics simulation*", Journal of Physics: Condensed Matter **17**, 6459 (2005)

5. J. Hegedus, K. Kohary, S. Kugler, "*Light-induced volume changes in amorphous selenium. Molecular dynamics simulation: Sample preparation and excitation*", Journal of Optoelectronics and Advanced Materials **7**, 59 (2005)

6. J. Hegedus, S. Kugler, "*Molecular dynamics simulation of amorphous selenium prepared by different methods*", Journal of Optoelectronics and Advanced Materials **7**, 1923 (2005)

7. J. Hegedus, K. Kohary, S. Kugler, K. Shimakawa, "*Photo-induced volume changes in selenium. Tight-binding molecular dynamics study.*", Journal of Non-Crystalline Solids **338**, 557 (2004)

8. J. Hegedus, K. Kohary, S. Kugler, "*Comparative analysis of different preparation methods of chalcogenide glasses: Molecular dynamics structure simulations*", Journal of Non-Crystalline Solids **338**, 283 (2004)

**Book chapters, proceedings and online publications:**

9. S. Kugler, J. Hegedus, K. Kohary, Book chapter in "Optical properties of condensed matter and applications", to be published by Wiley & Sons. in 2006 (in print)

10. J. Hegedus, P. Thomas, S. Kugler, Proceedings of Frühlingsakademie, 2005, Balatonfüred, Hungary, "Molekulardynamische Untersuchungen von lichtinduzierten Volumenenderungen im amorphen Selen"

11. J. Hegedus, Master Thesis "Molecular dynamics simulation of preparation and light induced processes in amorphous semiconductors" (written in Hungarian, published online), Budapest, 2003

# Curriculum vitae

## Personal information:

Name: József Hegedüs
Born: Hungary, Budapest, 1979.10.13.
Nationality: Hungarian

## Education:

| | |
|---|---|
| 2003-2006 | PhD scholarship. Fellow of the Marburg-Budapest European Graduate College. |
| 2003 | M.Sc. in physics. Master thesis: ”Molecular dynamics study of preparation and photo-induced phenomena in amorphous semiconductors” |
| 2001-2003 | Condensed matter specialization. |
| 1998-2003 | Engineering-physicist faculty, Technical University of Budapest and Economics |
| 1994-1998 | Grammar school, Fazekas Mihály[1] |

## Awards, prizes:

| | |
|---|---|
| 2005 | The “Ferenczi György” prize for semiconductor research[2] |
| 2003 | First place in nationwide physics competition among all universities |
| 2003 | Prize for outstanding scientific work by The Hungarian Foundation of High Education and Research |
| 2002 | First place in university-wide physics competition |
| 1998 | Fourth place in nationwide physics competition[3] |

## Teaching activities and supervisions of PhD students:

One semester of quantum chemistry for physics students at Budapest University of Technology and Economics, Hungary (2005)
Four semesters of physics laboratory practice (held in German) at Phillipps University Marburg, Germany (2003-2004)
Supervision of one PhD student (R. Lukacs) at Budapest University of Technology and Economics, Hungary, project: “Molecular dynamics simulation study of obliquely deposited amorphous chalcogenides”, (2005)

**Spoken languages**: English (fluent, state exam), German (fluent, state exam), French (basic)

---

[1] “Fazekas Mihaly” secondary grammar school is considered to be the best grammar school in Hungary.
[2] This award is given every year to a scientist younger than 35-years-age for his/her successful research.
[3] Jozsef Hegedus has been immediately accepted to all of the most prominent Universities in Hungary.